TKK Dissertations 233
Espoo 2010

THERMAL AND MECHANICAL ANALYSES OF HIGH-SPEED PERMANENT-MAGNET ELECTRICAL MACHINES

Doctoral Dissertation

Zlatko Kolondzovski

Aalto University
School of Science and Technology
Faculty of Electronics, Communications and Automation
Department of Electrical Engineering

TKK Dissertations 233
Espoo 2010

THERMAL AND MECHANICAL ANALYSES OF HIGH-SPEED PERMANENT-MAGNET ELECTRICAL MACHINES

Doctoral Dissertation

Zlatko Kolondzovski

Doctoral dissertation for the degree of Doctor of Science in Technology to be presented with due permission of the Faculty of Electronics, Communications and Automation for public examination and debate in Auditorium S4 at the Aalto University School of Science and Technology (Espoo, Finland) on the 6th of August 2010 at 12 noon.

Aalto University
School of Science and Technology
Faculty of Electronics, Communications and Automation
Department of Electrical Engineering

Aalto-yliopisto
Teknillinen korkeakoulu
Elektroniikan, tietoliikenteen ja automaation tiedekunta
Sähkötekniikan laitos

Distribution:
Aalto University
School of Science and Technology
Faculty of Electronics, Communications and Automation
Department of Electrical Engineering
P.O. Box 13000
FI - 00076 Aalto
FINLAND
URL: http://sahkotekniikka.tkk.fi/
Tel. +358-9-470 22387
Fax +358-9-470 22991
E-mail: zlatko.kolondzovski@tkk.fi

ISBN 978-952-60-3279-5
ISBN 978-952-60-3280-1 (PDF)
ISSN 1795-2239
ISSN 1795-4584 (PDF)
URL: http://lib.tkk.fi/Diss/2010/isbn9789526032801/

TKK-DISS-2789

Monikko Oy
Espoo 2010

Aalto University

ABSTRACT OF DOCTORAL DISSERTATION	AALTO UNIVERSITY SCHOOL OF SCIENCE AND TECHNOLOGY P.O. BOX 11000, FI-00076 AALTO http://www.aalto.fi

Author Zlatko Kolondzovski

Name of the dissertation
Thermal and mechanical analyses of high-speed permanent-magnet electrical machines

Manuscript submitted 19.11.2009	Manuscript revised 11.02.2010
Date of the defence 06.08.2010	
☐ Monograph	☒ Article dissertation (summary + original articles)

Faculty	Faculty of Electronics, Communications and Automation
Department	Department of Electrical Engineering
Field of research	Modelling of electrical machines
Opponent(s)	Prof. Aldo Boglietti
Supervisor	Prof. Antero Arkkio
Instructor	Doc. Anouar Belahcen

Abstract

In the thesis, methods for the thermal and mechanical analyses of high-speed PM electrical machines are presented and implemented. The first method implemented for the thermal analysis is a combined 2D-3D numerical method. The thermal and turbulent properties of the flow, such as the temperature rise in the flow and the coefficients of thermal convection, are estimated using a 2D multiphysics method that couples CFD with heat-transfer equations. The detailed distribution of the temperature rise in the whole solid domain of the machine is determined using a 3D numerical heat-transfer method. The temperature rises in the machine are also estimated with the traditional thermal-network method, which uses a totally different approach to the heat-transfer analysis. The methods used for the mechanical analysis of the machine include finite-element rotordynamics modelling of the rotor for estimation of the critical speeds and the shapes of the bending modes and also analytical estimation of the stress in the retaining sleeve. The implemented methods are used for the comparative thermal and mechanical analyses of three different high-speed PM rotor constructions. The first type of rotor construction is retained with a carbon-fibre sleeve and uses a shield for eddy currents made of aluminium. The second rotor construction is retained with a retaining sleeve made from the alloy Ti-6%Al-6%V-2%Sn and the sleeve of the third rotor construction is made from the alloy Ti-2.5%Cu. The last two rotor constructions do not have separate eddy-current shields. The comparative analysis shows that the rotor with a carbon-fibre sleeve and an aluminium eddy-current shield shows the best thermal properties. The rotor with a retaining sleeve made of the titanium alloy Ti-6%Al-6%V-2%Sn offers promising thermal properties because the critical temperatures in the rotor are not exceeded. Additionally, the same rotor construction provides the best rotordynamics properties when compared to the other rotor constructions. The rotor construction retained with a sleeve made of the alloy Ti-2.5%Cu is inferior from the thermal and mechanical points of view when compared with the previous rotor constructions. The methods used for the thermal and mechanical analyses are also used for the determination of the maximum power limits for high-speed PM electrical machines for air-compressor applications. For that purpose, five high-speed PM electrical machines for the speeds of 20,000 rpm, 40,000 rpm, 60,000 rpm, 80,000 rpm, and 100,000 rpm are designed in order to determine their maximum mechanical powers. The electromagnetic, thermal, and mechanical designs of each machine are performed simultaneously and all the critical values of the thermal and mechanical design constraints are considered. The obtained maximum power limit defines the speed-power region of safe operation of the high-speed PM electrical machines intended for compressor applications.

Keywords high-speed electrical machines, permanent magnets, thermal modelling, rotordynamics.

ISBN (printed) 978-952-60-3279-5	ISSN (printed) 1795-2239
ISBN (pdf) 978-952-60-3280-1	ISSN (pdf) 1795-4584
Language English	Number of pages 190
Publisher Department of Electrical Engineering, Aalto University School of Science and Technology	
Print distribution Department of Electrical Engineering, Aalto University School of Science and Technology	

☒ The dissertation can be read at http://lib.tkk.fi/Diss/2010/isbn9789526032801

Preface

This research work was carried out during the period between October 2005 and November 2009 at the Department of Electrical Engineering, Helsinki University of Technology (today a part of Aalto University).

First of all, I would like to express my sincere gratitude to Professor Antero Arkkio for his guidance, invaluable help, and support during the whole work. I wish to thank the Head of the Department of Electrical Engineering, Professor Asko Niemenmaa, for offering me the opportunity to work in this environment and also for his cordiality, support, and encouragement.

I am thankful to Docent Anouar Belahcen and Professor Emeritus Tapani Jokinen for the fruitful discussions, constant help, and valuable comments during the research. I would also like to express my special appreciation to Mr. Ari Haavisto for his help concerning the practical issues. I owe thanks to all of my colleagues for creating a pleasant, warm, and very positive working atmosphere.

I also thank Professor Jaakko Larjola and Petri Sallinen from Lappeenranta University of Technology for the generous help they have given me about some scientific and practical issues related to the aspects of mechanical engineering this work deals with and the provision of measured data.

The additional financial support given by the Centre for International Mobility (CIMO), the Graduate School of Electrical Engineering, and Tekniikan Edistämissäätiö are gratefully acknowledged.

I would like to express my special gratitude to Professor Lidija Petkovska from Ss. Cyril and Methodius University in Macedonia for discovering and enhancing of my passion and interest in the field of electrical machines and for her recommendation to continue my education in the same field at Helsinki University of Technology in Finland.

Special thanks to all of my friends in Finland and Macedonia for sharing life experiences and for the unforgettable cheerful moments.

The completion of this thesis would not have been possible without the support of the members of my family. I am deeply grateful to my sister Aneta, my mother Zora and my father Bojo for their endless encouragement and care. Special thanks go to my wife Marija. Her deep love and continuous support were the main sources of confidence and motivation for me to carry out and finalise this work.

Espoo, November 2009

Zlatko Kolondzovski

Contents

List of publications

This thesis consists of an overview and the following publications:

P1. Kolondzovski Z. Determination of a critical thermal operation for high-speed permanent magnet electrical machines. *COMPEL-The International Journal for Computation and Mathematics in Electrical and Electronic Engineering*, Vol. 27, No. 4, 2008, pp. 720-727.

P2. Kolondzovski Z., Belahcen A., Arkkio A. Multiphysics thermal design of a high-speed permanent-magnet machine. *Applied Thermal Engineering*, Vol. 29, January 2009, pp. 2693-2700.

P3. Kolondzovski Z, Belahcen A., Arkkio A. Comparative thermal analysis of different rotor types for a high-speed permanent-magnet electrical machine. *IET Electric Power Applications*, Vol. 3, No. 4, July 2009, pp. 279-288.

P4. Kolondzovski Z. Multiphysics method for determination of the stator winding temperature in an electrical machine. *Proceedings of the XIV International Symposium on Electromagnetic Fields in Mechatronics, Electrical and Electronic Engineering - ISEF 2009*, Arras, France, 10-12 September, 2009, 8 p.

P5. Kolondzovski Z. Numerical modelling of the coolant flow in a high-speed electrical machine, *Proceedings of the XVIII International Conference on Electrical Machines - ICEM 2008*, Vilamoura, Portugal, 6-9 September 2008, 5 p.

P6. Kolondzovski Z., Sallinen P., Belahcen A., Arkkio A. Rotordynamics analysis of different rotor structures for high-speed permanent-magnet electrical machines. *IET Electric Power Applications*, 19 p., in press.

P7. Kolondzovski Z., Arkkio A., Larjola J., Sallinen P. Power limits of high-speed permanent-magnet electrical machines for compressor applications. *Report Series on Electromechanics*, Report 76, Aalto University School of Science and Technology, Espoo 2010, 21 p., ISSN 1456-6001, ISBN 978-952-60-3274-0.

List of symbols and abbreviations

List of symbols:

B_r	remanent flux density, [T]
C_f	friction coefficient dependent on the length of the air gap and the Couette Reynolds number, [/]
C_M	friction coefficient that depends on the clearance and the tip Reynolds number, [/]
$\mathbf{C}_n$	matrix of non-rotating damping, [N·s/m]
C_p	heat capacity, [J/kg·K]
$\mathbf{C}_r$	matrix of rotating damping, [N·s/m]
$C_{\varepsilon 1}$	model constant in the κ-ε turbulence model, [/]
$C_{\varepsilon 2}$	model constant in the κ-ε turbulence model, [/]
C_μ	model constant in the κ-ε turbulence model, [/]
$cos\ \varphi$	displacement factor, [/]
$\mathbf{F}$	volumetric force vector, [N]
F_g	geometrical factor of the air gap, [/]
$\mathbf{f}$	force matrix, [N]
$\mathbf{f}_n$	matrix of non-rotational forces, [N]
$\mathbf{f}_r$	matrix of rotational forces, [N]
$\mathbf{G}$	gyroscopic matrix, [N·s/m]
$\mathbf{G}_T$	thermal conduction matrix, [W/K]
H_c	coercive force, [A/m]
h	heat transfer coefficient of convection, [W/(m^2·K)]
h_{ag}	coefficient of convection in the air gap, [W/(m^2·K)]
h_{avg}	average coefficient of thermal convection, [W/(m^2·K)]
h_{local}	local coefficient of thermal convection, [W/(m^2·K)]
I_r	rated electrical current, [A]
i	imaginary unit, [/]
$\mathbf{K}$	stiffness matrix, [N/m]
$\mathbf{K}''_r$	hysteretic damping matrix, [N/m]
k	coefficient of stiffness, [N/m]
k_1	roughness coefficient of the rotor surface, [/]
k_2	velocity factor of the fluid, [/]
k_a	Kármán's constant, [/]
k_{eff}	effective thermal conductivity, [W/(m·K)]
k_f	physical thermal conductivity of the fluid, [W/(m·K)]
k_t	turbulent thermal conductivity, [W/(m·K)]
l_r	length of the rotor, [m]
$\mathbf{M}$	mass matrix, [kg]
$\mathbf{N}$	matrix of shape functions, [/]
Nu	Nusselt number, [/]
n	rotational speed, [rpm]
n_r	rated rotational speed, [rpm]

n_c	critical speed, [rpm]
$\boldsymbol{n}_s$	surface unit vector, [/]
P	power, [W]
P_r	rated power, [W]
$\mathbf{P}$	loss matrix, [W]
P_{acc}	losses caused by the acceleration of the fluid in a tangential direction,[W]
$P_{af\,ag}$	air-friction losses in the air gap, [W]
$P_{af\,re}$	air-friction losses on the surfaces of the rotor end-disks, [W]
P_{fp}	air-friction losses caused by a pressure drop in the fluid passages, [W]
Pr_t	turbulent Prandtl number, [/]
p	pressure, [Pa]
p_p	number of pole pairs, [/]
Δp	pressure drop of the fluid in the fluid passages, [Pa]
$\mathbf{q}$	vector of coordinates of the element, [/]
q_1	coolant flow in the channel between the stator yoke and the frame, [m^3/s]
q_2	coolant flow in the air gap, [m^3/s]
q_f	flow rate in the fluid passage, [m^3/s]
$\boldsymbol{q}_h$	heat flux, [W/m^2]
q_{h0}	general heat flux entering the domain, [W/m^2]
$\boldsymbol{q}_{h\,down}$	heat flux on the down side of the boundary, [W/m^2]
$q_{h\,local}$	local heat flux, [W/m^2]
$\boldsymbol{q}_{h\,up}$	heat flux on the upper side of the boundary, [W/m^2]
r_r	outer radius of the rotor, [m]
r_m	average value of the stator and rotor radii, [m]
r_{r1}	inner radius of the rotor end, [m]
r_{r2}	outer radius of the rotor end, [m]
r_{s1}	inner stator radius, [m]
T	temperature, [K, ^{0}C]
$\mathbf{T}$	temperature matrix, [K]
T_0	prescribed temperature, [K, ^{0}C]
T_a	Taylor number, [/]
T_{ag}	Air gap torque, [N·m]
T_{am}	modified Taylor number, [/]
T_{amb}	ambient temperature, [^{0}C]
T_f	temperature of the fluid, [K, ^{0}C]
$T_{f\,local}$	local temperature of the fluid, [K, ^{0}C]
$T_{max\,cfs}$	maximum temperature of the carbon-fibre sleeve, [^{0}C]
$T_{max\,pm}$	maximum temperature of the permanent magnets, [^{0}C]
$T_{max\,sw}$	maximum temperature of the stator winding, [^{0}C]
T_w	temperature of the solid wall, [K, ^{0}C]
$T_{w\,local}$	local temperature of the solid wall, [K, ^{0}C]
ΔT	temperature rise, [K]
ΔT_{max}	maximum temperature rise, [K]
$\Delta T_{max\,rot}$	maximum temperature rise of the rotor, [K]
$\Delta T_{max\,sw}$	maximum temperature rise of the stator winding, [K]
t	time, [s]

U	voltage, [V]
$\mathbf{u}$	vector of displacements, [m]
$\mathbf{V}$	averaged velocity field, [m/s]
v	velocity, [m/s]
$\mathbf{v}$	velocity vector, [m/s]
v_s	surface speed, [m/s]
v_a	mean axial fluid velocity, [m/s]
v_{f1}	initial speed of the flow when entering the air gap, [m/s]
v_{f2}	final total speed of the flow in the air gap, [m/s]
v_t	mean tangential fluid velocity, [m/s]
v_τ	friction velocity, [m/s]
W	energy, [J]
y	coordinate perpendicular to the solid wall, [m]
y^+	dimensionless wall distance, [/]
δ	radial length of the air-gap, [m]
ε	dissipation rate of the turbulent kinetic energy, [m^2/s^3]
η	coefficient of efficiency, [/]
η_t	turbulent cinematic viscosity, [m^2/s]
κ	turbulent kinetic energy, [m^2/s^2]
κ_w	turbulent kinetic energy at the wall, [m^2/s^2]
μ	dynamic viscosity of the air, [Pa·s]
ρ	mass density, [kg/m^3]
ρ_{air}	mass density of the air, [kg/m^3]
σ_{max}	maximum stress, [N/m^2]
σ_ε	model constant in the κ-ε turbulence model, [/]
σ_κ	model constant in the κ-ε turbulence model, [/]
Ω	angular speed of the rotor, [rad/s]

List of abbreviations:

2D	two-dimensional
3D	three-dimensional
Bwd	backward
CFD	computational fluid dynamics
EMF	electromotive force
FE	finite element
FEA	finite-element analysis
FEM	finite-element method
Fwd	forward
Nd-Fe-B	neodymium-iron-boron
PM	permanent magnet
RANS	Reynolds averaged Navier-Stokes equations
SiFe	silicon-iron
Sm-Co	samarium-cobalt
Ti-6%Al-6%V-2%Sn	titanium alloy with 6% aluminium, 6% vanadium, 2% tin
Ti-2.5%Cu	titanium alloy with 2.5% copper

1 Introduction

1.1 Background

In recent years, high-speed electrical drives have been widely studied because of their advantages, which include their higher power density, smaller size, and increased reliability in comparison with conventional drives. They are often used in many applications in industry, such as compressors, vacuum pumps, turbine generators, flywheel energy-storage systems, drilling tools, friction welding units, etc. The speed and the power of a high-speed application are controlled by a frequency converter. It means that the application is directly attached to the same shaft of the electrical machine and the gearbox which serves for changing the speed in conventional applications is not needed. The absence of the gearbox increases the reliability, reduces the costs of maintenance, and enables an oil-free performance of the drive. Three main types of high-speed electrical machines are used in the industry: permanent-magnet (PM) machines, induction machines and switched-reluctance machines. This thesis is fully dedicated to the analysis of high-speed PM machines.

High-speed PM machines are a very promising design alternative for high-speed applications because of their better efficiencies, power factors, and utilisation factors in comparison to the other types of high-speed electrical machines. But, on the other hand, high-speed PM machines have a much more complex rotor construction in comparison to the other types of high-speed machines. This causes the appearance of additional constraints that can restrict the design of the machine, especially, from the thermal and mechanical points of view. The rotor cross-section of a typical high-speed PM machine is presented in Figure 1.1. Unlike the other types of high-speed machines, high-speed PM machines have permanent magnets and a retaining sleeve (usually made of a carbon-fibre material) on the rotor and these are thermally sensitive materials. An overheating of the machine can cause a demagnetisation of the magnets and damage to the carbon-fibre sleeve. The smaller size of the machine, which is considered to be an advantage, can appear as a disadvantage from the thermal point of view because the smaller size contributes to a higher loss density and this makes the cooling of the machine more difficult. Besides that, the complex construction of the rotor causes some disadvantages from the mechanical point of view. For example, the magnets, the carbon-fibre sleeve, and the eddy-current shield have very low stiffness so they cannot improve the overall rotor stiffness, which is mainly dependent on the solid-steel shaft. In fact, they represent an additional mass that lowers the values of the critical speeds of the rotor. If one of the critical speeds appears to be very close to the rated speed of the machine, it can lead to unpleasant phenomena such as excessive acoustic noise emissions and catastrophic failures during operation like bending and damaging of the rotor shaft. In order to create a design that will ensure the safe operation of a high-speed PM machine, the methods used for the thermal and mechanical analysis of the machine should be very reliable.

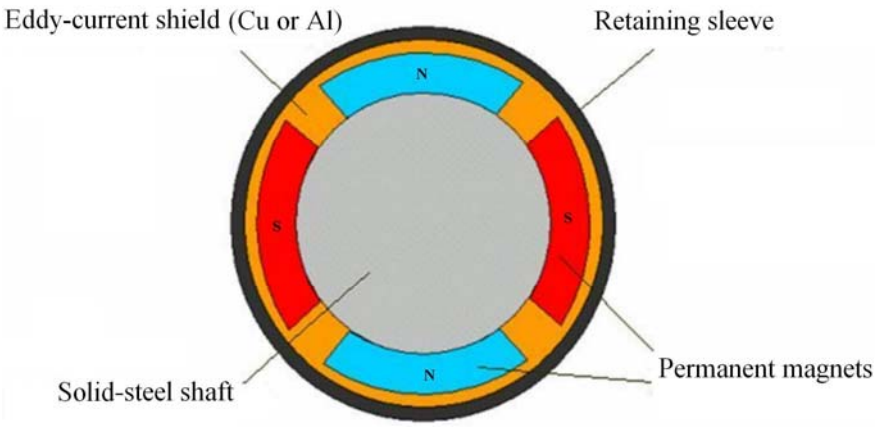

Figure 1.1: Cross-section of a typical high-speed PM rotor.

One of the most commonly used methods for the thermal analysis of electrical machines is the traditional thermal-network method. The method is simple and reliable but its main disadvantage is its coarse nature, which results in a rough thermal view of the machine. The advanced numerical techniques that are being developed today give the opportunity for more sophisticated thermal analysis that can show a very fine temperature distribution throughout the whole domain of an electrical machine. Using the computational fluid dynamics (CFD), a more realistic modelling of the turbulent flow in the complex machine geometry can be performed in comparison with the empirical methods, which mostly refer to simple geometries and rely on many approximations. The numerical techniques also offer the possibility of an advanced rotordynamics analysis of the rotors used in high-speed applications.

1.2 Aim of the work

The main objective of this study is to make a contribution to the methods for the thermal and mechanical analyses of high-speed PM electrical machines. The study is focused on the development of a multiphysics method that couples the heat-transfer method with the CFD. In this case, the heat and turbulent phenomena in the whole machine domain can be analysed simultaneously. Concerning the mechanical analysis, this study is mostly focused on the application of numerical methods for rotordynamics in order to determine the influence of the rotor elements on the rotordynamics properties of the rotor. The estimation of the stress in the retaining material is performed using analytical equations. The methods that are proposed in the thesis also serve for comparative thermal and mechanical analyses of high-speed PM rotors that are equipped with parts that have different thermal and mechanical properties. In this case, the most optimal construction that fulfils the best thermal and mechanical criteria can be determined. This study is also aimed at estimating the maximum power limits of high-speed PM electrical machines for compressor applications when the proposed thermal and mechanical methods are applied simultaneously.

1.3 Scientific contributions

This thesis contains scientific contributions in the field of high-speed PM electrical machines, especially, in their thermal and mechanical analyses. The most important contributions of the thesis are listed below.

1. A multiphysics method for the thermal analysis of a high-speed PM electrical machine is developed and validated with measurements. The method makes a direct coupling between the CFD and heat-transfer equations. As an output result, it gives a simultaneous estimation of the turbulent properties of the fluid and the temperature distribution in the solid and fluid domains in the electrical machine. The method is a compromise between 2D axi-symmetric multiphysics rough modelling and 3D thermal fine modelling, a compromise that allows a fast and accurate estimation of the thermal and turbulent phenomena in an electrical machine with the use of a low amount of computational resources. The experimental validation of the method is performed in Publications P3 and P4.

2. Using the multiphysics method, a special consideration is given to the convection phenomena in the machine. As an output result, the local coefficients of thermal convection are numerically estimated on each surface between the solid and fluid domain, with particular consideration of the inlet and outlet parts of the machine. The results are compared with the results obtained using traditional semi-empirical equations that give average values of the coefficients of thermal convection only for basic geometries.

3. A comparative thermal analysis of high-speed PM rotors that are retained with different types of sleeves is performed. The accuracy of the analysis is verified with indirect measurements of the temperatures of the permanent magnets. The analysis shows what type of titanium alloy used as a material for a retaining sleeve is suitable from thermal point of view besides the mostly used carbon-fibre material. The experimental validation of the methods used is performed in publication P3.

4. A critical thermal operation of a high-speed PM electrical machine is determined. As an output result, the minimum value of the fluid flow in the air gap for different types of eddy-current shields on the rotor is determined in order to keep the temperatures of the thermally sensitive parts of the machine below the critical limit.

5. A comparative rotordynamics analysis of high-speed PM rotors that are retained with different types of sleeves is performed. The analysis shows what type of titanium alloy used as a material for a retaining sleeve is the most suitable for high-speed PM applications from the mechanical point of view. The methods used for the rotordynamics analysis are validated with measurements. The experimental validation of the methods used is performed in Publication P6.

6. The methods developed for the thermal and rotordynamics analysis are used for the determination of the maximum power limits of high-speed PM electrical machines for compressor applications. As an output result of the analysis, the theoretical limit of the maximum powers is estimated in the speed range 20,000-100,000 rpm. For this purpose, all the important thermal and mechanical constraints are considered simultaneously.

1.4 Structure of the work

The dissertation consists of the following parts:

- Chapter 1 presents the introduction, aim, and scientific contribution of the work.

- Chapter 2 presents the literature study that was performed. The most significant references related to the previous research in the field of high-speed PM machines are listed and briefly discussed. The references are listed according to their specific subtopics, which refer to general design considerations, applications, the determination of losses, thermal analysis, mechanical analysis, and the determination of the power-speed limits of high-speed PM machines. The need for further research activities is also expressed here.

- Chapter 3 gives a brief presentation of the methods for thermal and mechanical analyses of high-speed PM machines that are used in this thesis. Regarding the thermal analysis, at the beginning, the numerical methods for modelling the fluid domain and the solid domain of the machine are presented. In addition, a short description of the traditional thermal-network method is also given. The methods considered for rotordynamics analysis include a finite-element beam-like model and a 3D model of the rotor geometry.

- Chapter 4 presents the general results that are obtained from the methods for the thermal and mechanical analyses of the machine. At the beginning, the results for the electromagnetic and mechanical losses are presented. The coefficients of thermal convection for each cooling surface are calculated using the numerical-multiphysics method and using traditional semi-empirical equations. The temperature rises in the fluid domain and in all parts of the solid machine domain are calculated by the numerical-multiphysics method and the traditional thermal-network method. The values of the first four critical speeds (two rigid and two flexural) of the machine examined are also presented.

- Chapter 5 presents comparative thermal and mechanical analyses of rotors with different sleeve materials. The aim of the analyses is to examine the possibility of using titanium alloys to retain of the rotor structure and to examine their influence on the thermal and rotordynamics behaviours of the rotors. The first alloy used is Ti-6%Al-6%V-2%Sn and the second one is a Ti-2.5%Cu alloy. The results of the thermal and mechanical analyses in the cases when these alloys are

used are compared with the results when a carbon-fibre material is used for retaining the rotor structure.

- Chapter 6 presents the maximum power limits for high-speed PM electrical machines for air compressor applications, determined in the speed range 20,000-100,000 rpm. For this purpose, five permanent-magnet machines are designed and the electromagnetic, thermal, and mechanical designs of the machines are performed simultaneously. The critical values of all the thermal and mechanical constraints are considered in order to obtain the maximum powers of the electrical machines. The obtained maximum powers define the theoretical limit of performance of the high-speed compressor applications.

- The results presented in the thesis are discussed in Chapter 7.

The publications that are included in the thesis are reprinted in Appendix C. Chapters 4, 5, and 6 are based on these publications. Some new results that are not presented in the publications are included in Chapter 4. The experimental validation of the theoretical methods is given only in the publications.

Publication P1

The paper determines the critical thermal operation of a high-speed PM electrical machine. The electrical machine under consideration is a high-speed PM machine designed for a rated speed n_r=31,500 rpm and power P_r=130 kW. An aluminium shield on the rotor is used for the reduction of the eddy-current losses in the permanent magnets. The machine has air-flow cooling. The aim of the paper is to determine the type of aluminium shield, as well as the minimum value of the airflow, that can provide safe operation of the machine from the thermal point of view.

The thermal analysis of the high-speed PM machine is performed using a thermal-network model developed by the author. The input parameters for the model are the dimensions and thermal properties of the machine parts, the rotating speed, the properties of the airflow, and all types of losses. The calculation of the electromagnetic losses is based on a time-stepping FEA. The ohmic losses in the winding, the air-friction and cooling losses as well as the coefficients of thermal convection, are calculated using analytical and semi-empirical equations. In the thermal network model, the whole structure of the machine is divided into thermal elements that are linked together with nodes. The thermal elements are the thermal resistances, heat sources, and heat sinks. The output parameters of the model are the average temperatures in each part of the machine. Using the described thermal-network model, we can determine the maximum temperatures of the permanent magnets, the carbon-fibre sleeve, and the outlet part of the end winding of the stator versus the airflow in the air gap. These parts are the most sensitive ones from the thermal point of view and therefore they are used for the determination of the critical thermal point. The critical temperatures of the permanent magnets and the carbon-fibre sleeve are $T_{\text{max pm}}$=100 ^{0}C and $T_{\text{max cfs}}$=130 ^{0}C,

respectively. The class of insulation of the stator winding is F, and this means that its critical temperature is $T_{\max sw}$=155 ^{0}C. The value of the airflow in the air gap is varied in order to determine the critical thermal point of each of the aforementioned parts. Three different types of rotor designs are considered, according to the type of the aluminium shield: a rotor without an eddy-current shield, a rotor with an aluminium cage, and a rotor with an aluminium screen. In the rotor without an eddy-current shield, the eddy-current losses have the highest value and they are mainly generated in the permanent magnets. This causes an occurrence of a very high temperature in the magnets, which is much higher than the critical one. The airflow is not enough to cool the magnets and this type of rotor design is not justified. If we use an aluminium cage on the rotor consisting of bars that are placed between the magnets, then the eddy-current losses are reduced in comparison with the previous case. An airflow in the air gap of at least q_2=0.05 m^3/s is enough to maintain safe temperature of the magnets. The eddy-current losses have their lowest value when an aluminium screen is used on the rotor. In this case, an airflow of at least q_2=0.033 m^3/s is enough to maintain temperature of the magnets that is lower than the critical one. At the end, we can conclude that the magnets cannot be cooled effectively if they are not properly shielded from eddy currents.

Publication P2

The paper presents different methods for the thermal design of a high-speed PM electrical machine. The machine under consideration is the same one that is described in the previous publication. The main point of the paper is to explain the development of the numerical-multiphysics method for the thermal analysis of the electrical machine and to emphasise the advantages of this method over the traditional methods. The numerical-multiphysics method couples CFD and heat-transfer equations. The heat-transfer and CFD modelling are performed simultaneously and a 2D axi-symmetric model of the machine is used. This model performs a simultaneous estimation of the temperature rise in the fluid and solid domains of the machine. The turbulent flow of the fluid is modelled using the κ-ε turbulent model. The velocity, pressure, and temperature fields are solved simultaneously in the model. The idea of creating a 2D axi-symmetric turbulent model is only to estimate the turbulent properties of the fluid domain, such as the temperature rise of the air flow and the coefficients of thermal convection on each surface of the machine parts. This model can also give a rough estimation of the temperature rise in the solid domain of the machine but it is primarily intended for modelling the fluid domain since this domain is considered to have an axial symmetry. The temperature rise of the whole solid domain of the machine is estimated by using a 3D thermal model of the machine. The parameters of the fluid, such as its temperature rise and the coefficients of thermal convection, are taken from the 2D multiphysics model and they are imported into the boundary conditions of the 3D heat-transfer model. Because the 3D heat-transfer method is inherently dependent on the 2D multiphysics method, these two methods can be considered as a one numerical-multiphysics method. The temperature rises of all the parts in the machine are also determined by using the thermal-network method. In this paper, this method is used just for a comparison of its results with the results obtained by the numerical-multiphysics

method. Although both of these methods are based on completely different theoretical approaches, the comparison between the results obtained from them shows a good agreement.

Publication P3

The paper presents a thermal analysis of three different rotor constructions for a high-speed PM electrical machine designed for rated power P_r=130 kW and rotational speed n_r=31,500 rpm. The differences between the constructions are in the types of the retaining material and the eddy-current shield. The first rotor construction has a carbon-fibre sleeve as a retaining material and an aluminium shield for eddy currents. The other two rotors have retaining sleeves made of titanium alloys that also take the role of shielding the magnets from eddy-current losses. The titanium alloy used for the second rotor is Ti-6%Al-6%V-2%Sn and the alloy for the third rotor is Ti-2.5%Cu. The thermal analysis of the paper is performed using the numerical-multiphysics method and the thermal-network method already described in the Publications P1 and P2. Because these methods are based on a theoretical nature, their accuracy should be validated with measurements. In this paper, the validation of the theoretical methods is performed by indirect measurements of the temperature of the permanent magnets of the machine. In fact, the direct measurement of the temperature of the magnets during the operation is very difficult because they are totally enclosed in the rotor structure. The temperature rise of the magnets is determined by measuring the change in the magnetic flux generated from the magnets. In fact, a certain change of the temperature in the magnets directly influences the value of the magnetic flux. The change in the rotating magnetic flux is determined by measuring the electromotive force that is induced on a search coil that is mounted on the stator slots.

During the thermal analysis, the outer diameters of the three rotor structures are kept the same. It means that in all three cases the air gap has the same length. This will ensure that the thermal properties of the coolant are the same and we can make a more objective comparison between the thermal behaviours of all the rotor types. Only the inner dimensions of the rotor parts are not the same because, when using different materials, we need different inner dimensions to design the different rotors in order to provide the same power. The numerical-multiphysics method and the thermal-network method give very close results for the temperature rises in the different rotors. The rotor with a carbon-fibre sleeve and an aluminium shield has the lowest temperature rise because the lowest value of eddy-current losses is generated in this rotor construction. The rotor with a titanium retaining sleeve made of the Ti-6%Al-6%V-2%Sn alloy offers promising thermal properties. Although it does not contain an additional eddy-current shield and the temperature rise in the magnets is somewhat higher than in the previous case, that temperature rise is still below the critical limit. The analysis shows that this type of rotor construction fulfils the thermal criteria and it can also be used in high-speed applications. The rotor with a titanium retaining sleeve made of the Ti-2.5%Cu alloy develops temperature rises that can exceed the critical thermal limits of the rotor elements and this fact calls into question its applicability in high-speed applications.

Publication P4

The paper deals with a thermal analysis of the stator winding of a high-speed PM electrical machine. The thermal analysis is performed using the numerical-multiphysics method already described in the Publication P2. The machine under consideration is the same one that is described in the Publications P1 and P2. The temperature in the whole stator domain is determined, with the asymmetry of the cooling being taken into account. This asymmetry occurs at the place at which the cables of the stator winding are connected with the terminal box. These cables pass through the region between the stator yoke and the frame and they block the air flow. This causes a significant reduction of the convection and therefore causes higher temperatures in this part of the machine. The multiphysics method is validated by direct measurement of the temperature at different points of the stator winding. Ten thermocouples are used for this purpose, of which five are placed along the side of the stator where the terminals are in order to measure the highest temperature of the winding; the other five are placed along the opposite side of the stator, which is exposed to normal cooling. A comparison of the results shows that there is a good agreement between the temperatures estimated by the numerical-multiphysics method and the temperatures that are directly measured using the thermocouples.

Publication P5

In this paper, a coupled CFD and heat-transfer analysis of the fluid domain of a high-speed PM electrical machine is presented. The machine under consideration is the same one that is described in the previous publications. The CFD and heat-transfer modelling are performed simultaneously using a 2D axi-symmetric model of the fluid domain of the machine. The turbulent and thermal properties of the fluid in the machine, such as the velocity field, the local coefficient of thermal convection in the air gap, and the temperature rise of the fluid are estimated.

Publication P6

In this paper, a rotordynamics analysis of different rotor structures for high-speed PM electrical machines is presented. The analysis is performed on two different high-speed electrical machines intended for different applications. The first machine is a high-speed compressor with a rated speed n_r=30,000 rpm and power P_r=130 kW. The actual rotor has a carbon-fibre sleeve and an aluminium cage for shielding the magnets from eddy currents. It is a subcritical rotor that operates close to the first flexural critical speed, which is around n_c=36,000 rpm. The rotor is supported by oil-film bearings. The same rotor is redesigned twice by implementing a retaining sleeve made from the titanium alloys Ti-6%Al-6%V-2%Sn and Ti-2.5%Cu. The redesigns of the two rotor constructions are made for the same rated speed and power. The second rotor type that is analysed in the paper is an experimental solid-steel shaft. Three different rotor constructions are designed for this rotor shaft. The first construction is retained with a

carbon-fibre sleeve and the other ones are retained with sleeves made from the titanium alloys Ti-6%Al-6%V-2%Sn and Ti-2.5%Cu. These rotor constructions for the second type of rotor are designed for a rated speed n_r=36,000 rpm and power P_r=100 kW. The rotors retained with titanium-alloy sleeves do not have separate eddy-current shields. An extensive comparative FE rotordynamics analysis of the aforementioned constructions of the two types of rotors is presented. Each rotor construction is modelled using a beam-like model and a 3D model. The accuracy of the models is validated with measurements. For this purpose, the natural frequencies of the two actual rotor constructions are measured by performing impact-hammer tests. The measured values are close to the values of the natural frequencies of the rotors estimated by the beam-like and 3D models. During the impact-hammer tests, the rotors were not supported by the bearings and because of this, the influence of the bearings was not included in the numerical models.

The rotordynamics analysis in this paper takes into account only the influence of the electrical machine parts on the rotordynamics properties of the different rotor structures. During the design of the different rotor structures for the same type of rotor, the outer diameters are kept the same because they should fit the same stator. Only the dimensions of the inner parts of the electrical machine are not the same. The analysis shows that the rotors retained with a sleeve made from the titanium alloy Ti-6%Al-6%V-2%Sn provide the best rotordynamics properties and these constructions are superior to the other types of rotor constructions. The main reason is that this type of rotor construction has a thicker solid-steel shaft and permanent magnets with a lower mass because of the thinner retaining sleeve and the absence of an additional eddy-current shield. The analysis also shows that if the length of the high-speed PM electrical machine represents a significant part of the total rotor length, using a retaining sleeve made from the titanium alloy Ti-6%Al-6%V-2%Sn may significantly improve the rotordynamics properties of the rotor.

Publication P7

In this paper, the maximum power limits for high-speed PM electrical machines for air compressor applications are determined in the speed range 20,000-100,000 rpm. In order to fulfil the task, five high-speed PM machines for compressor applications with rated speeds 20,000 rpm, 40,000 rpm, 60,000 rpm, 80,000 rpm and 100,000 rpm are designed in order to determine their maximum powers. The obtained values of the maximum powers at the end of the analysis are: 1,500 kW, 425 kW, 181kW, 93 kW and 55 kW, respectively. The machines have the same basic construction and only their dimensions are different since they are dependent on the power and speed. The rotor in each machine has surface mounted Nd-Fe-B magnets, aluminium eddy-current screen and carbon-fibre retaining sleeve. The stator of each machine contains a radial cooling duct. The cooling air is blown in the duct and proceeds in the air-gap of the machine. The end-windings use impingement air jets for cooling. The compressor wheel is attached to the rotor shaft of each machine. The maximum powers of the machines are limited by their thermal and mechanical constraints. In order to determine the maximum

power limit of each machine, the critical values of all the thermal and mechanical constraints are considered in the design process. These constraints are summarised in Table 6.2, page 69. The electromagnetic, thermal, and mechanical designs of each machine are performed simultaneously. The electromagnetic design is almost the same as the design of a conventional electrical machine and its final step is to calculate the electromagnetic losses generated in the machine. The electromagnetic losses are the input parameters of the thermal design. The thermal design is performed using the numerical-multiphysics method described in the Publication P2. The mechanical design considers the rotordynamics properties of the rotor using the method described in the Publication P6 and also the retention of the rotor elements against the centrifugal forces that arise during the high-speed operation. The reliability of the design techniques used in this paper is validated with measurements. The results for the estimated maximum powers determine the speed-power region of safe operation of high-speed PM machines intended for compressor applications.

The publications that are part of this thesis contain the scientific contributions listed in Section 1.3. The relation between the scientific contributions and the publications is given in Table 1.1.

Table 1.1: Relation between the scientific contributions and the publications.

Scientific contribution	Publication						
	P1	P2	P3	P4	P5	P6	P7
1. Multiphysics method for thermal analysis		X	X	X	X		X
2. Local coefficients of thermal convection		X	X	X	X		X
3. Comparative thermal analysis			X				X
4. Critical thermal operation	X						
5. Comparative rotordynamics analysis						X	X
6. Maximum power limits							X

1.5 Author's contribution to the publications

The ideas, research methodologies, and writing of the publications that are part of this thesis are mainly attributed to the author of the thesis, who is also the first author of all the publications. The other co-authors contributed to the papers mainly through revisions, comments, scientific expertise in their fields, providing some experimental data etc. A detailed description of the authors' contributions to each paper is given in the list below:

P1. The idea, research methodology, and writing of the paper are solely attributed to the author.

P2. The idea, research methodology, and writing of the paper are mainly attributed to the first author. The co-authors contributed to the paper through revisions and comments.

P3. The idea, research methodology, and writing of the paper are mainly attributed to the first author. The co-authors contributed to the paper through revisions and comments.

P4. The idea, research methodology, and writing of the paper are solely attributed to the author.

P5. The idea, research methodology, and writing of the paper are solely attributed to the author.

P6. The idea, research methodology, and writing of the paper are mainly attributed to the first author. The second co-author provided the experimental data from the impact-hammer tests of the two rotors that were examined. The third and the fourth co-authors contributed to the paper through revisions and comments.

P7. The research methodology and writing of the paper are mainly attributed to the first author. The second co-author gave the main idea of the paper and he also contributed through revisions and comments. The third co-author helped in the determination of the dimensions of the compressor wheels. The fourth co-author provided experimental data obtained from the impact-hammer test.

2 Literature study

2.1 Design of high-speed PM machines for different applications

The design considerations for high-speed PM electrical machines are reported in many references. According to the basic application, three main types of references can be distinguished. The first type is related to high-speed PM machines that are used in real applications in industry. The second type of references also considers the practical applications of high-speed PM machines but when they are exploited in laboratories as test machines. The third type of references is related to purely theoretical analyses of high-speed PM machines in the field of a certain scientific area, mainly simulating the electromagnetic design of the machines.

2.1.1 High-speed PM electrical machines intended for real industrial applications

There are many papers that deal with the use of high-speed PM machines for real applications in industry. The design of the machines described in these papers can be considered as the most reliable one, since if a high-speed machine is used in a real application, it must fulfil all the thermal, mechanical, and electromagnetic constraints. The papers found in the literature consider permanent magnet machines used mostly in compressor applications, electrical power generation with gas turbines, flywheel systems and drilling tools.

Some design considerations for high-speed PM machines applied in compressor applications used in the petrochemical industry were reported by Bailey et al. (2009). The paper re-examines the usual assumptions about deploying synchronous machines in high-speed applications. The machine examined has a rated power P_r=8 MW and a target speed n=15,000 rpm. The stator has thin low-loss silicon-steel laminations and multistrand coils and it was designed for high-frequency operations using commercial FEA software. A rotordynamics analysis of the rotor was performed for two different types of bearings. In the first case, the rotor was supported on active-magnetic bearings and in the second case the rotor was supported by ball bearings. The rotordynamics analysis showed that the operation of the machine was sub-critical and the first forward-flexural mode was about 20% above the nominal operating speed for both types of bearings. The cooling of the machine was performed by air entering a stator duct in the middle of the stator and in the end-winding regions and also by a water/glycol cooling flow in a cooling jacket placed on the outer surface of the stator. The thermal analysis was performed using lumped-parameter and CFD modelling. The models used in the paper were experimentally validated by Saban at al. (2008).

The number of references that deal with electrical power generation with gas turbines is very high. A hybrid variable-reluctance/PM generator for aircraft generation systems was presented by Mellor et al. (2005). The aim was to utilise the windmill effect of the low-pressure turbine of the aircraft engine for emergency power generation. The

requirement of the generator is to generate a regulated emergency power supply with power P_r=20 kW and voltage U=270 V within the operating speed range of n=3,000-30,000 rpm. The paper indicates that high-speed PM and switched reluctance machines are the strongest contenders for this kind of application. Because these two different types of high-speed machines have different operating characteristics and limitations, a detailed comparison of their design features was made. The paper presents the benefits of using high-speed PM machines as being their high efficiency and potentials for their sensor-less control and the drawbacks as being their complicated construction. The authors reported that a certain saliency in the rotor geometry was recommended for an efficient operation in the field-weakened constant-power region and to exploit the reluctance torque in the low-speed region. The PM rotor topology does not produce this saliency and the desired characteristic was achieved by using a hybrid rotor structure with separate PM and variable reluctance sections. The PM section contains a Halbach array of samarium-cobalt magnets retained with a carbon-fibre sleeve and the variable reluctance section is made from islands of cobalt-iron laminations held within a high-strength retaining structure. The losses of the electrical machine were determined experimentally and the overall efficiency of the system was estimated to be up to η=84 %, considering also the efficiency of the power converter.

An industrial high-speed PM generator with a rated power P_r=75 kW and a rated speed n_r=45,000 rpm for gas-turbine applications was presented by Agahi and Schröder (1996). In this arrangement, the radial inflow expander turbine is mounted on the shaft of a high-speed PM machine. The whole rotor construction is supported on active-magnetic bearings and the high-speed drive is oil-free. The expander was designed to expand pure gases (hydrogen, helium, nitrogen, etc) and also mixed process gases (air, natural gas, hydrogen reach natural gas, etc) up to a 12/1 pressure ratio. The design is suitable for hazardous and also for non-hazardous environments. Variable vanes were used to provide effective control of the process and high efficiency over a wide range of the fluid flow. The paper gives a detailed description of the construction of the electrical machine and the AC-AC converter used that converts the electric power coming from the high-speed generator to electric power with a constant voltage and frequency that are suitable for feeding the grid. The system allows operation in a motor performance without any modifications. The drive was tested in two test stages. In the first stage, a special test stand was built in order to perform tests in steady-state and transient load conditions. Two identical machines linked with a high-speed flexible coupling were used. One machine was the tested generator and the other one was used in a motor mode in order to simulate the turbine. In the second stage of the test, the turbine-generator package was tested in real conditions with pressurised air and connected to the grid.

A design solution of a power unit for a research submersible was presented by Jokinen et al. (1998). The unit charges the batteries of a submarine being able to operate at a depth of 6,000 metres. The small size of the high-speed drive makes it very suitable for this kind of application. The generator of the unit is a high-speed PM generator with a rated power P_r=25 kW and speed n_r=40,000 rpm and it is directly coupled to a gas turbine on the same rotor shaft. Samarium-cobalt magnets embedded in an aluminium cylinder are used and the whole construction is retained with a titanium sleeve. The

efficiency of the generator is estimated to be η=94%. The number of stages of the gas turbine is two. The construction is supported by two radial tilting pad bearings and one thrust bearing. The bearings are lubricated with pressurised toluene. The whole power unit was tested in a hydraulic test chamber and in a natural ocean environment. The self-controlled operation, the self start as well as the emergency-stop operations of the power unit were proved.

Zwyssig et al. (2005) presented a design for an ultrahigh-speed PM generator. The rated speed of the electrical machine is n_r=500,000 rpm and the rated power is P_r=100 W. The authors reported that the generator could be implemented in a gas-turbine application. The design method starts with the selection of the machine type and the types of the bearings. Because of the simplicity, robustness, small size, and the avoidance of auxiliary equipment, ball bearings are selected for the test setup. The electromagnetic, thermal, and mechanical analyses are also presented in the paper. Some of the theoretical considerations are validated by an experimental test bench which consists of two machines on a common shaft, one acting as a motor and the other one as a generator. Another high-speed PM generator for gas-turbine applications was presented by Offringa et al. (1996). The rated power of the generator is P_r=1,400 kW and the rated speed is n_r=18,000 rpm. The paper presents the electromagnetic design of the machine, including calculation of the electromagnetic losses of the rotor and stator. The verification of the electromagnetic design is performed experimentally by means of a high-speed PM test generator with a rated power P_r=80 kW and rotational speed n_r=12,000 rpm.

Kenny et al. (2005) presented a control for a high-speed flywheel energy storage system for space applications. The system is intended to replace chemical batteries for current energy storage in space applications. Flywheels have the advantage of a longer lifetime, higher efficiency, and a greater depth of discharge than batteries. A high-speed PM electrical machine was used to perform as a motor or generator. It has surface-mounted samarium-cobalt magnets retained with a carbon-fibre sleeve. The rated power of the electrical machine is P_r=1.5 kW and the full speed is n_r=60,000 rpm. Field orientation and a combination of mechanical sensor-less techniques are used to control the machine from zero speed up to full-speed operation. The flywheel system was designed for energy storage of W=364 Wh and the maximum surface speed of the rim is v_s=700 m/s.

Boglietti et al. (1991) presented motor drives for spindle applications in the speed range between 10,000 and 25,000 rpm and power range between 20 and 60 kW built using high-speed PM machines. The paper also analyses different types of converters for feeding high-speed PM machines. At the end of the paper, an experimental test at a rated speed and torque on a machine with a rated power P_r=45 kW and rated speed n_r=10,000 rpm is performed.

2.1.2 High-speed PM electrical machines intended for laboratory applications

The laboratory test machines are used in laboratories in order to examine some of the electromagnetic, thermal, and mechanical properties of high-speed applications. They usually serve for the examination of one type of properties without taking care of the other types. For example, if the electrical and thermal properties of the machine should be examined and the rotordynamics ones are not within the scope of the analysis, then the mechanical drive (turbine or compressor wheel) is substituted by another electrical machine. In this case, the real mechanical constraints are not properly fulfilled since the type and size of the mechanical drive have a great impact on the critical speeds.

An experimental method for the determination of the losses of a high-speed PM electrical machine was presented by Diop and Schröder (1998). The machine under consideration has a rated power P_r=70 kW and speed n_r=45,000 rpm and is supported on active magnetic bearings. The method is based on back-to-back tests performed on two identical machines linked on a flexible high-speed coupling. One machine operated as a generator (the machine being tested) and the other one was used in a motor mode, replacing the turbine. The machines used identical bearings and frequency converters. The losses under no-load conditions were determined by performing retardation tests. The test results showed a good agreement with the calculated ones and the efficiency of the machine was estimated to be η=95%.

Mekhiche et al. (1999) discussed different steps involved in the design process of high-speed PM and induction motor drives. For that purpose, a high-speed PM machine with a rated power P_r=20 kW and speed n_r=47,000 rpm and a high-speed induction machine with a rated power P_r=45 kW and speed n_r=92,500 rpm were considered. The paper gives some general considerations about the electromagnetic, mechanical, and thermal designs of high-speed machines. The mechanical analysis includes FE calculation of the stresses in the retaining material and the design considerations from the rotordynamics point of view were not reported. The analysis is dedicated only to the part of the electrical machine without any mechanical considerations. Another paper that is dedicated to the general design and experimental testing of high-speed PM machines was published by Jang at al. (2005). The machine under consideration has rated power P_r=50 kW and speed n_r=70,000 rpm. The paper mostly explains the electromagnetic design criteria using a 2D analytical method that is validated by FEA. A brief rotordynamics analysis of the electrical machine is given but the influence of the mechanical part (the compressor wheel) is not taken into account. The paper does not emphasise the importance of introducing a thermal analysis during the design process of the machine. Some details about the fabrication of the electrical machine and the power-conversion device are listed. At the end, the paper shows some experimental results about the magnetisation test of the rotor, the back EMF measurement, and the input-voltage test. Some of the test results are compared with the results obtained with the FEM and there is a very good agreement between the results obtained with the different methods.

Binder et al. (2006) analysed high-speed PM machines with the permanent magnets fixed to the rotor in different ways. The first rotor construction has surface-mounted magnets retained by a carbon-fibre bandage and the second one has magnets that are buried in the rotor steel. The authors examined the mechanical stress that arises in the material used for fixing the magnets during high-speed operation and they used analytical and FE calculations. The study examines the fixing of the magnets in the two different types of high-speed PM rotors designed for the same rated speed n_r=40,000 rpm and power P_r=40 kW. The analysis shows that the rotor with surface-mounted magnets fixed by a carbon-fibre bandage is the better choice because the mechanical strength of the construction is much higher when compared with the rotor with buried magnets. Another high-speed PM machine with magnets buried inside the solid-steel rotor shaft was presented by Hippner and Harley (1992). The rated power of the machine was P_r=10 kW and the speed was n_r=30,000 rpm. The rotor of the machine was a solid-steel cylinder with rectangular spaces for the Sm-Co magnets. In order to reduce the leakage flux, holes were drilled in the solid rotor body in the space between the magnets, leaving thin bridges of steel between the magnets. This preserved the smooth outer surface of the solid steel and the leakage flux in the rotor was significantly reduced. The performance of the machine was estimated by developing a 2D FEM. A prototype of the machine with the rated power and speed was built. The induced stator voltage of the machine was measured at a rotor speed n=30,000 rpm and no-load and load tests were performed. The thermal and mechanical properties of the machine were not reported in the paper.

A study that examines the influence of the sleeve on the rotor losses was presented by Takahashi et al. (1994). The examined high-speed PM motor had a rated power P_r=5 kW and speed n_r=180,000 rpm. The paper examines the influence of the type of the retaining sleeve and the radial length of the air gap on the motor efficiency. First, sleeves made of stainless steel were employed. In order to investigate how the rotor losses change with the thickness of the sleeve, two types of motors with the same stator but with different sleeves on the rotor were manufactured and tested. In the case of the thicker sleeve, the air gap length was δ=0.5 mm and in the case of the thinner sleeve, the air gap length was δ=3 mm. In the case of the longer air gap, the slot ripples were reduced, which resulted in lower eddy-current losses in the sleeve. After that, a carbon-fibre sleeve was employed. In this case, the eddy-current losses in the sleeve were almost eliminated and the efficiency of the motor was higher in comparison with the previous cases. The mechanical stresses in the sleeves, the losses, and the temperatures in the magnets were not investigated.

A design optimisation of a high-speed PM electrical machine with a rated power P_r=30 kW and speed n_r=24,000 rpm was reported by Schätzer and Binder (2000). The power output of the machine was maximised and the volume of the magnets was minimised. Three rotor dimensions were varied: the magnet height, the pole coverage angle, and the rotor radius. The optimised solution is compared with a previously built machine of similar design and equal ratings, designed without this optimisation method. For power P=30 kW, the optimised solution resulted in a rotor design with a magnet volume 16%

less. For the optimised machine, the strength limit of the retaining sleeve and the demagnetisation condition in the case of a short circuit are fulfilled.

There are some papers that are dedicated to the development and laboratory analysis of bearingless high-speed PM machines. A design procedure for bearingless high-speed PM motors was given by Schneider et al. (2005). An existing high-speed PM machine with active magnetic bearings was redesigned in a bearingless technology. The novel type of design is an alternative to the popular use of active magnetic bearings in high-speed applications. The idea is to integrate the levitation forces into the motor itself. In the so-called bearingless motor, besides the main three-phase winding with a certain number of pole pairs p_p, there is an additional three-phase winding with $p_p \pm 1$ number of pole pairs that produces the lateral forces. The bearingless rotor is split into two identical halves of the length, i.e. two identical motors are obtained, with half of the rated output power each. In that case they provide two identical points of support. The main advantage of this construction is from a rotordynamics point of view. The active magnetic bearings elongate the rotor shaft, which results in lower values for its critical speeds. The total axial length of the machine that is modelled in the paper is reduced by about 12 %. The rated speed of the modelled machine is n_r=40,000 rpm and the total rated power of the drive is P_r=40 kW (two machines of 20 kW each). The procedure of the electromagnetic design is explained in detail. Further thermal and mechanical analyses are needed in order to provide a complete reliable design of the machine for real applications. Schneider and Binder (2007) reported a different design solution of a bearingless high-speed motor. Instead of the classical topology of one high-speed machine with two active magnetic bearings, the authors proposed one active magnetic bearing to be replaced by the bearingless motor. The motor had the double role of electrical machine and bearing, and, together with the remaining active magnetic bearing, presented the two points of radial suspension. A prototype of a high-speed PM motor with a rated power P_r=500 W and speed n_r=60,000 rpm was investigated. The prototype machine was loaded with an eddy-current brake for low and medium speeds and with a compressor wheel for high-speed. An axial magnetic bearing was required since the compressor wheel could produce an axial force. The complete support of the rotor was realised with a combination of one bearingless motor (motor and radial bearing) and one combined radial-axial active magnetic bearing. The whole drive was designed following the design rules for high-speed PM machines, except the stator slots, which were dimensioned to fit both the phase and the levitation windings. The prototype machine was successfully tested. The analytical and FEM values of the EMF, torque, lateral force, levitation voltage, and levitation current that were obtained during the design were very close to the measured values. The authors expressed the expectation that it would be possible to design bearingless high-speed PM motors with much higher power rates that will satisfy the industrial needs in future. The principles of radial force production in bearingless high-speed PM machines were analysed by Oshima et al. (1996). At the beginning, the relationships between the rotor diameters and inductances were found and the radial magnetic forces were derived from the inductances. The relationships between the radial forces and the voltages and currents on the terminals of the levitation windings were also established. The analysis was done on a prototype

bearingless motor with thin permanent magnets. The relationships of the radial forces, voltages, and currents were confirmed experimentally.

2.1.3 Simulated design of high-speed PM electrical machines

There are some references in which the high-speed PM machine is under a theoretical design and the design ideas and solutions are implemented by performing a simulated design. In most of the cases, the simulated design takes into account only one type of constraints, for example only the electromagnetic ones, with the thermal and the mechanical constraints being left out.

The influence of the material used for the stator laminations on the iron losses in a high-speed PM machine was evaluated by Paulides et al. (2004). It was shown that the iron loss in the stator could be reduced considerably if instead of 3 % SiFe laminations, 6.5 % SiFe laminations were used. The electromagnetic FEA was performed on a high-speed PM machine with a rated power P_r=1.5 MW and speed n_r=20,000 rpm. The theoretical results were not validated with measurements.

There are some papers that deal with the design of the retaining sleeve and eddy-current shield and their influence on the electromagnetic losses of the machine. Zhou et al. (2006) studied the influence of the conductivity of the retaining sleeve on the rotor eddy-current losses in a high-speed PM motor. A comparison was performed between a rotor retained with a titanium alloy and a rotor retained with a carbon-fibre material. The loss in the titanium alloy sleeve was much higher than the loss in the carbon-fibre sleeve, but the titanium sleeve provided better shielding effects for the magnets and its better thermal conductivity enabled better cooling for the magnets. The total loss in the rotor was almost equal in both cases. Additionally, the influence of a copper shield on the thermal behaviour of the machine was described. With the introduction of the copper shield, the eddy-current losses were mostly developed in the shield and the total loss in the rotor was dramatically reduced. The examined electrical machine had a rated power P_r=3 kW and speed n_r=150,000 rpm. The eddy-current losses were calculated using a time-stepping FEA. The authors provided a thermal analysis of the machine for the cases of different sleeves with and without the shield. The analysis proved that only in those cases when the copper shield was used, the maximum rotor temperature was in the acceptable range, regardless of the type of the sleeve. The thermal analysis was quite rough since the air between the stator and rotor was assumed to be motionless and the air-friction losses were neglected.

An analysis of the unbalanced forces of high-speed PM machines was given by Jang et al. (2003). Two machines with a rated power P_r=1 kW and speed n_r=40,000 rpm were considered. They both had a slotless stator, the first one had a radial magnetised rotor and the second one had a Halbach magnetised rotor. 2D FEA was used to study the electromagnetic unbalanced forces in the machines. The comparative analysis showed that the machine with the Halbach magnetised rotor had a lower radial traction than the one with the radial magnetised rotor. Another paper that shows the advantage of the

Halbach magnetised rotor was published by Jang et al. (2004). In the paper, an analytical field analysis and 2D FEA were used to estimate the rotor eddy-current losses of a high-speed PM machine with a Halbach magnetised rotor and also with a radial magnetised rotor. In both cases, the machine was designed for a rated power P_r=5 kW and speed n_r=40,000 rpm. The comparative study proved that the machine with the Halbach magnetised rotor had lower eddy-current losses in the rotor than the machine with the radial magnetised rotor.

A design proposal for a high-speed PM electrical machine intended to operate in cryogenic applications was given by Zheng et al. (2005). The machine with a rated power P_r=2 kW and speed n_r=200,000 rpm was designed to operate at a cryogenic temperature T=77 K. The criteria for selecting the materials for cryogenic applications for the machine parts were presented. Sm-Co permanent magnets were selected for this application as they were considered a better choice than Nd-Fe-B magnets. Nd-Fe-B permanent magnets were not recommended for temperatures below T=140 K since they could easily demagnetise. The permanent magnet (in one piece) was located centrally in a hollow shaft. The shaft material was chosen to be a high-stress titanium, also recommended in the paper for cryogenic applications. The structure of the stator was slotless. Mechanical stress and rotordynamics simulations were also performed. All types of losses were determined analytically and by using the FEM and the total efficiency was estimated to be above η=90 % at T=77 K.

2.2 Calculation of losses in high-speed electrical machines

In the references dealing with high-speed PM machines that are dedicated to the determination of various types of losses, the losses are divided into two general types: electromagnetic and mechanical losses.

The calculation of the electromagnetic losses in a high-speed electrical machine does not differ from the calculation of these types of losses in a conventional machine. Arkkio (1987) reported a method for the calculation of the electromagnetic losses in a conventional induction motor based on a time-stepping FEA. In this work, a two-dimensional FEA was performed and the 3D end-winding effects were included in the circuit equations. Second-order isoparametric triangular elements were used for generating the FE mesh. The time dependence of the variables was modelled by the Crank-Nicolson time-stepping method. The motion of the rotor was achieved by changing the finite-element mesh in the air gap at each time step.

The mechanical losses are generated as a result of the coolant flow in the machine and they are usually divided into air-friction and cooling losses. These types of losses are not very significant in conventional machines but they can be very significant and even dominant in high-speed machines. Because of the high rotating speed, the amount of air-friction and cooling losses that are generated in a high-speed machine can be very significant. A method for the estimation of these types of losses is discussed in more detail by Saari (1995). The air-friction losses occur as a result of the friction between

the moving rotor parts and the air. The proposed method estimates the air friction losses in the air gap with the equation

$$P_{\mathrm{af\,ag}} = k_1 C_{\mathrm{f}} \rho_{\mathrm{air}} \pi \Omega^3 r_{\mathrm{r}}^4 l_{\mathrm{r}} \tag{2.1}$$

Here k_1 is the roughness coefficient of the outer rotor surface, C_{f} is the friction coefficient dependent on the length of the air gap and the Couette Reynolds number and ρ_{air} is the air density. The air-friction losses are heavily dependent on the angular velocity of the rotor Ω, the outer radius r_{r}, and length l_{r} of the rotor. The same equation can be applied for the ends of the rotor shaft. The air-friction losses on the rotor ends can be modelled as for rotating discs and the method proposes the next equation:

$$P_{\mathrm{af\,re}} = \frac{1}{2} C_{\mathrm{M}} \rho_{\mathrm{air}} \Omega^3 \left(r_{\mathrm{r2}}^5 - r_{\mathrm{r1}}^5 \right) \tag{2.2}$$

C_{M} is the friction coefficient, which depends on the clearance and the tip Reynolds number. r_{r2} and r_{r1} are the outer and inner radii of the rotor end, respectively. The method divides the cooling losses into friction losses in fluid passages and losses associated with the acceleration of the cooling fluid. The friction losses in the fluid passages are the result of some amount of power that is needed to blow the cooling fluid through the electrical machine. Because of the friction, there is a pressure drop Δp in the fluid in the fluid passages and the losses are

$$P_{\mathrm{fp}} = \Delta p q_{\mathrm{f}} \tag{2.3}$$

where q_{f} is the flow rate in the fluid passage. The second type of cooling losses is the type of losses that are due to the acceleration of the air-flow in the air gap. Actually, when the cooling fluid enters the air gap, the rotating rotor accelerates the fluid to a tangential movement. The power needed for this acceleration is

$$P_{\mathrm{acc}} = \frac{2}{3} \pi \rho_{\mathrm{air}} v_{\mathrm{a}} v_{\mathrm{t}} \left(r_{\mathrm{s1}}^3 - r_{\mathrm{r}}^3 \right) \Omega \tag{2.4}$$

v_{a} and v_{t} are the mean axial and tangential fluid velocities, respectively, and r_{s1} is the inner stator radius. The power for the acceleration of the cooling fluid is provided by the machine. This power is turned into heat usually at the outlet side of the machine, where the circumferential movement of the fluid is stopped.

A paper in which all the types of losses in a high-speed PM generator are calculated was presented by Aglén (2003). The paper briefly explains the determination of air-friction losses, bearing losses, iron losses, stator-winding losses, and the harmonic losses in the rotor. The total losses of the generator were also determined experimentally by performing a back-to-back test. The losses were determined calorimetrically, the input and output temperatures, as well as the flow rate were measured in the stator cooling water, the cooling air, and the oil of the bearings. Another extensive analysis of the

losses in a high-speed PM machine was presented by Binder et al. (2004). The authors explained the calculation of all types of losses in detail and the results were validated with measurements. The temperature rises in various parts of the machine were also measured. Luomi et al. (2009) presented a method for the optimisation of the efficiency of ultrahigh-speed PM machines. The air-friction losses of the machine were taken into account, in addition to the iron, copper, and eddy-current losses. Analytical models were used for the calculation of the loss components. The loss-minimisation procedure was applied for selecting the internal dimensions of the machine. A comparative analysis of rotor losses for two high-speed PM rotors was reported by Cho at al. (2006). The two machines they considered had identical rated speed and power, only the materials of the retaining sleeves on the rotors were different. The first rotor has a retaining sleeve made of the Inconel718 material and the second one has a carbon-fibre sleeve. The comparative study shows that the rotor retained with a carbon-fibre sleeve has rotor losses that are about six times lower. Another study concerning the rotor losses in a high-speed electrical machine was presented by Jiqiang et al. (2005). The paper presents methods for the calculation of air-friction losses and eddy-current losses caused by time and space harmonics.

2.3 Thermal analysis of electrical machines

The methods that are used for the thermal analysis of the high-speed PM machines are usually divided into traditional thermal-network methods and numerical methods. The thermal-network method is based on analytical and semi-empirical equations for thermal analysis of the machines. Recent developments in the computer technology have enabled numerical methods to be used for the thermal analysis of the high-speed PM machines. A summary of the evolution of the methods for the thermal analysis of electrical machines is given by Boglietti et al. (2009a). The paper compares the most common methods: the traditional thermal-network method, the numerical method for heat transfer, and the CFD method. The strengths and the weaknesses of these methods are also discussed.

2.3.1 Traditional methods for thermal analysis

There are many references in which the thermal analysis of electrical machines using traditional methods is reported. An extensive description of a thermal-network model that is intended for the analysis of conventional induction motors was reported by Mellor at al. (1991). The model provides both steady-state and transient solutions of the temperatures in the electrical machine. The paper also gives the equations for the thermal modelling of all the parts in the machine and represents a fundamental study for many subsequent papers in the same field. The proposed model was simplified by Boglietti et al. (2003). Boglietti et al. (2008) gave an extensive analysis of the following important thermal parameters of an induction motor: the equivalent thermal resistance between the external frame and ambient at zero fan speed, the equivalent thermal conductivity between the winding and laminations, the forced-convection heat-transfer

coefficient between the end-winding and the end-caps, the radiation heat-transfer coefficient between the external frame and ambient, the interface gap between the laminations and the external frame, the air-cooling speed, and the equivalent thermal resistance of the bearing.

Another thermal-network model for the modelling of small cage induction motors was given by Kylander (1995). A thermal analysis of two high-speed induction machines using a thermal-network model was elaborated by Saari (1998). The model is validated with measurements and is used for the estimation of the maximum power limits of high-speed induction motors. A thermal analysis of a high-speed PM generator using a thermal-network method was reported by Aglén and Andersson (2003). The model shows how the temperature distribution depends on the losses, especially the magnets temperature resulting from the rotor losses. The study also shows that when a copper screen is used in the rotor, the rotor losses are reduced to a reasonable level. In a high-speed electrical machine, the temperature rise in the flow cannot be neglected. It is quite high because of the huge loss density in the machine. A method proposed by Jokinen and Saari (1997) can be used for the estimation of the temperatures rise of the flow in the machine. The proposed method deals with modelling the coolant flow in the thermal networks. The coolant flow is modelled by heat-flow controlled temperature sources.

The heat transfer resulting from thermal convection is the most usual and the most effective way to cool an electrical machine. That is why reliable methods are needed for the accurate determination of the coefficients of thermal convection on each surface of the machine. There are many references in which the coefficients of thermal convection are determined using traditional empirical or semi-empirical methods. The coefficients of convection in each part of a high-speed induction machine were determined by Saari (1995). The method is quite reliable when applied to simple geometries as the air-gap region. At the beginning, the method proposes the calculation of the Taylor number of the tangential flow using the equation

$$T_{\mathrm{a}} = \frac{\rho_{\mathrm{air}}^2 \Omega^2 r_{\mathrm{m}} \delta^3}{\mu^2} \tag{2.5}$$

Here μ is the dynamic viscosity of the air, δ is the length of the radial air-gap, and r_m is the mean value of the stator and rotor radii. The equation is valid for a very small air-gap length but if the length of the air gap is comparable with the rotor radius, the modified Taylor number should be used, expressed with the equation

$$T_{\mathrm{am}} = \frac{T_{\mathrm{a}}}{F_{\mathrm{g}}} \tag{2.6}$$

In electrical machines, the length of the air gap is much smaller than the rotor radius and the geometrical factor F_{g} is assumed to be $F_{\mathrm{g}} \approx 1$ and therefore $T_{\mathrm{am}} \approx T_{\mathrm{a}}$ (Saari (1995)). The modified Taylor number can determine the Nusselt number in three different regimes:

$$\begin{aligned} &\mathrm{Nu} = 2 && (T_{\mathrm{am}} < 1,700) \\ &\mathrm{Nu} = 0.128 T_{\mathrm{am}}^{0.367} && (1,700 < T_{\mathrm{am}} < 10^4) \\ &\mathrm{Nu} = 0.409 T_{\mathrm{am}}^{0.241} && (10^4 < T_{\mathrm{am}} < 10^7) \end{aligned} \tag{2.7}$$

The heat-transfer coefficient of convection on the rotor and stator surfaces in the air gap can be calculated by the equation

$$h_{\mathrm{ag}} = \frac{\mathrm{Nu} k_{\mathrm{f}}}{\delta} \tag{2.8}$$

where k_{f} is the thermal conductivity of the fluid. For more complicated geometries than the air-gap region, such as the end-space region of the machine, the method faces some difficulties. The coefficients of convection in the end-space regions in induction motors were experimentally determined by Boglietti and Cavagnino (2007) and also by Boglietti et al. (2009b). Their proposed procedure enables the forced convection to be separated from the other heat exchange phenomena in the end-space region. The values of the coefficients obtained agree well with the results reported in some older references, such as Mellor et al. (1991).

Although the thermal analyses of electrical machines performed using traditional thermal-network methods are quite reliable and give good agreements with measured results, they have some big disadvantages. The representation of the machine geometry is very coarse and the thermal-network method usually gives a rough output of the thermal profile of the machine. In fact, this method gives only the mean temperatures of the machine parts but not a detailed temperature distribution throughout the whole domain. The determination of the coefficients of thermal convection over a cooling surface in the traditional methods is usually limited to simple geometries and based on empirical equations that give the mean values of the coefficients.

2.3.2 Numerical methods for thermal analysis

The basics of the numerical calculation of the heat transfer were summarised by Minkowycz et al. (2006). The modern numerical techniques give the opportunity for an advanced thermal analysis of the electrical machines. The fine thermal view of the machine gives the temperature distribution at each point and there is a better opportunity to find the hot spots in the machine. Using CFD, the fluid flow can be modelled more realistically. The fundamentals of the finite-element method for fluid dynamics were summarised by Zienkiewicz et al. (2005). The complex geometry of the machine has a strong influence on the properties of the flow and much better analysis can be performed in comparison with the traditional methods that mostly refer to simple geometries. When CFD is coupled with heat-transfer equations, the main benefits of this modelling are the estimation of the temperature at each point of the fluid domain and the calculation of the local heat-transfer as a result of convection from the machine parts to the cooling fluid.

A numerical thermal analysis of a conventional induction motor is reported by Huai et al. (2003). Only the temperature distribution in the motor was estimated numerically but the coefficients of thermal convection in the paper were calculated by empirical equations. A thermal analysis of permanent-magnet synchronous motors was reported by Chin et al. (2003). The analysis was performed using thermal-network and finite-element models of the machine. Wang et al. (2008) reported a numerical thermal analysis of a high-speed PM machine. The coefficients of thermal convection in the paper were calculated using empirical equations. The results were verified by measuring the temperature of the stator winding.

Trigeol et al. (2006) gave a thermal analysis of an induction machine that was a combination between the thermal-network method and CFD modelling. The thermal network method was used for modelling the solid domain of the machine and the CFD model was used only for modelling the convection. Liao at al. (1999) reported a numerical method for the thermal analysis of an induction motor and a conjugate solution included the temperature distribution and the fluid flow solution. Another application of CFD in the field of electrical machines was reported by Shanel et al. (2000). In their paper, the coefficients of thermal convection at different surfaces in a salient pole electrical machine were determined. The results were obtained using the κ-ε turbulence model and they were compared with results obtained from some older references. The method was improved by Shanel et al. (2003) by introducing the combined heat transfers of conduction and convection on the rotor of a salient pole, air-cooled synchronous generator. The study emphasises the advantage of the simultaneous modelling of the heat transfer of conduction inside the rotor together with the heat transfer of convection occurring on the outer rotor surface. The method is used in order to find an improved way to cool of the rotor, leading to an increased effect of convection and reduced temperature of the field winding.

An extensive numerical CFD approach to the estimation of the turbulent fluid properties in the air gap in a high-speed induction machine was reported by Kuosa at al. (2004). The fluid temperature in the air gap and the local coefficients of thermal convection on the rotor and stator surfaces in the air gap were determined and experimentally validated. The analysis was performed using three different turbulent models: κ-ε, κ-ω, and the Baldwin-Lomax model. The proposed method does not estimate the temperature distribution in the solid domain of the machine, so the temperatures of the stator and rotor surfaces are accepted only as constant values at the boundaries of the CFD model.

In a paper reported by Micallef et al. (2008), CFD modelling was used in order to investigate the cooling of the end-winding of an induction motor. The local coefficients of thermal convection on the surface of the end-winding were estimated using CFD and the results were validated by measurements. The temperature inside the end-winding was not determined. The surface temperatures of the end-winding and the frame were only assumed as constant values and they were put into the boundary conditions of the CFD model. CFD analysis of the impingement jet cooling of end-windings in a high-speed electrical machine was reported by Punnonen (2007). The turbulence of the fluid

was modelled using the κ-ε and κ-ω turbulence models. Measurements of the fluid velocity were used in order to validate the CFD results.

2.4 Rotordynamics analysis of electrical machines

The rotordynamics analyses of electrical machines are mainly based on the FEM. The fundamentals of the application of the FEM in the field of rotordynamics were reported in detail by Genta (2005) and also by Chen and Gunter (2005). A numerical and experimental study of the effects of the properties of the bearings on the first forward and backward critical speeds of a flexible rotor was reported by Sinou et al. (2005). Murphy et al. (2001) reported a numerical rotordynamics design for a model scale compulsator rotor and the analysis is accompanied by test results. The vibration analysis of a high-speed rigid rotor on flexible bearings was reported by Sakata et al. (1995) and the same analysis was repeated by Okamoto et al. (1995) but for a high-speed flexible rotor on flexible bearings. Merrill (1994) made a summary of the various terms, phrases and concepts associated with the rotordynamics of electrical machines. He summarised the concepts of natural frequency, critical speed, excitation, mechanical resonance, damping, torsional excitation, torsional critical speeds, unbalanced magnetic pull, and magnetic instability. Some general considerations and practical applications of rotordynamics in industry are reported by Gutzwiller and Corbo (2003) and Matsushita et al. (2000).

The literature available for the rotordynamics analysis of high-speed PM magnet machines is not very wide. Bailey at al. (2009) reported a rotordynamics analysis as a part of a design procedure for subcritical high-speed PM machines used in the petrochemical industry. A rotordynamics analysis was reported by Canders (1998) in order to establish the design concepts and to determine the power limits of high-speed PM machines supported by active magnetic bearings. A paper that is fully dedicated to the rotordynamics analysis of a high-speed PM machine is reported by Ede et al. (2002). In that paper, the natural frequencies of the rotor were determined using FEA and experimental measurements. The effects that arise during rotation, such as the gyroscopic effects are not considered. Some rotor parts, such as the permanent magnets and the carbon-fibre sleeve, are considered to increase the natural frequencies since they contribute to the stiffness of the rotor shaft. This can be valid when the rotor is not rotating but it is not a safe conclusion for a rotor in high-speed operation. If the rotor is rotating at a high speed, the huge centrifugal forces can displace the rotor elements in an outward direction so that only the carbon-fibre sleeve is retaining them and it is questionable whether or not they can improve the rotor stiffness.

2.5 Estimation of the maximum power and speed limits of high-speed PM electrical machines

The estimation of the maximum power limits of high-speed electrical machines is still a challenge. There are some existing references that consider this topic. Some of them are

mainly based on only one high-speed machine designed for a certain challenging speed and power. In some of them, the authors collect many practical cases that have already been published in other references in order to find out where the practical limitations on the operation of high-speed machines could be. There are some cases in which the authors are trying to make their own design intended for a theoretical electromagnetic analysis of a machine with a high rated power and speed without any consideration of the thermal and mechanical constraints of the machine. In order to estimate the power limitations of high-speed machines for real industrial applications, all the electrical, thermal and mechanical constraints should be implemented at the same time.

Bianchi et al. (2004) reported the potentials and limits of high-speed PM motors. The properties of the materials chosen for the permanent magnets, stator core and retaining sleeve were discussed. Nd-Fe-B magnets were recommended because of their high remanence and coercive force. Slotted and slotless stator topologies were considered and the losses for each topology were calculated and compared. The rotor losses for different types of metallic sleeves were compared. Despite the lower no-load flux density and complex winding manufacturing, the authors proposed a slotless topology. It was characterised by lower rotor losses and was considered to be less sensitive to the demagnetisation of the permanent magnets. Both the thermal limits and the demagnetisation limits of the permanent magnets were also evaluated. An optimisation procedure was described in order to obtain the maximum torque of the motor. The paper does not consider the influence of the mechanical constraints on the limitations of high-speed PM motors.

The current state of the speed and power limitations of high-speed machines was reported by Antipov and Danilevich (2007). The study presents only a collection of data from recent publications about the limits of operation of different kinds of high-speed machines: PM, induction, and switched-reluctance machines. Another similar collection of data was published by Rahman et al. (2004). A more extensive study was published by Arkkio et al. (2005). The paper suggests that the power of high-speed electrical machines is mainly limited by their thermal and mechanical constraints. Modern frequency converters do not restrict the speeds and the powers of high-speed drives any more. Three high-speed PM machines and three high-speed induction machines were designed with the same rated speeds and powers. The first machine is designed for a rated speed n_r=30,000 rpm and power P_r=540 kW, the second machine is designed for a rated speed n_r=60,000 rpm and power P_r=95 kW, and the third machine is designed for a rated speed n_r=100,000 rpm and power P_r=30 kW. The comparisons between the two types of machines show that the high-speed PM machines have better electromagnetic characteristics. They have better efficiency, a better power factor, and a better utilisation factor than the high-speed induction machines. Their disadvantage is in their higher thermal and mechanical constraints, which restrict their maximum powers. Binder and Schneider (2007) reported collected data for rated powers and speeds of different types of high-speed electrical machines. The data covers a wide power range from P_r=0.1 kW up to P_r=80 MW and circumferential speed from v_s=100 m/s up to v_s=250 m/s. Several design details for high-speed electrical machines are discussed, such as electromagnetic

utilisation, loss components, types of machines, bearing aspects and inverter-motor interaction.

A high-speed PM electrical machine with a rated power P_r=155 kW and speed n_r=69,000 rpm was designed by Castagnini et al. (2002). This combination of rated power and speed is one of the highest found in the available literature. The machine has two poles and a slotless stator construction. Besides being developed in order to reach high power and a high speed, it was also developed to operate with a high efficiency. The electrical and mechanical designs of the machine are given in detail. The mechanical design considered the stresses in the rotor resulting from the centrifugal forces and also the rotordynamics properties of the rotor. It is notable that the mechanical part of the high-speed application that should be attached to the same shaft of the electrical machine is not taken into account in the rotordynamics analysis. The machine was tested under no-load conditions up to a speed n=67,000 rpm (Castagnini and Leone (2002)). No full load test to check the possibility of a real industrial application of this machine was performed.

Canders (1998) presented the basic design concepts for high-speed PM electrical machines. The study is mostly dedicated to the influence of the air-friction losses and critical speeds on the design of the machine. The end of the paper is briefly dedicated to the maximum power limits of high-speed PM machines. The power limits versus rotor speed were estimated for surface speeds of the rotor v_s=200 m/s and v_s=280 m/s and also for different numbers of rotor poles, $2p_p$=2, 4, 6, and 8. In the region of lower rotational speeds, almost the same values of the maximum powers are obtained for rotor surface speeds of v_s=200 m/s and v_s=280 m/s. In general, the higher surface speed is preferable at higher rotational speeds, but for two-pole machines with rotational speeds higher than 60,000 rpm, the maximum power is not heavily dependent on the value of the surface speed. The thermal constraints that are used during the design process of the machines are not reported in the paper.

The recent research is related to the design and development of ultrahigh-speed PM machines. These machines operate at extremely high speeds and have low rated powers. An ultrahigh-speed PM machine with a rated speed n_r=500,000 rpm and power P_r=100 W was presented by Zwyssig et al. (2008). The authors considered this type of machine useful in different applications that require low power and very high speeds such as air-compressors, gas turbines, small drills, and spindles. The standard machine design and power electronics topology were considered as inapplicable in this case. In order to achieve simple mechanical construction and a small rotor diameter, the permanent magnet is placed inside a titanium sleeve. The stator is toothless, with a litz-wire winding. The machine has two poles, high efficiency, and a high power density. High-speed ball bearings were used for the initial testing of the machine because of their simplicity, robustness, small size, and avoidance of auxiliary equipment. The most optimal choice for the power electronics in this case was a voltage source inverter with block commutation and an additional dc-dc converter because of the low volume, low switching losses, no heat-sink cooling, small number of semiconductor devices and a relatively simple control. Further research performed by Zwyssig et al. (2009) was

dedicated to targeting rotational speeds towards and beyond n=1,000,000 rpm. The main reason for striving towards the so called megaspeed region was the emerging applications in the areas of medicine, dental technology, material processing, air compressors for fuel cells and gas-turbine systems. The authors recommended the PM machine technology as the best choice for very high speeds because in the other types of high-speed machines the flux density in the machine decreases with a reduction in the size of the machine, but in the PM machine it remains constant. Therefore, only the PM machines were considered for the applications with a very low system volume. The mechanical rotor construction and the minimisation of the high-frequency losses were considered as the main challenges during the design. Besides the high-speed drive designed for a rated speed n_r=500,000 rpm and power P_r=100 W, the authors reported another design of a high-speed drive for a gas-turbine application for a rated speed n_r=500,000 rpm and power P_r=1 kW. After that, in order to demonstrate the feasibility of a drive system in the megaspeed region, a high-speed PM machine for a rated speed n_r=1,000,000 rpm and power P_r=100 W was constructed. The machine was tested in high-speed, no-load operation and the maximum speed achieved was approximately n=1,100,000 rpm. This was considered a world record speed achieved by an electrical drive system.

2.6 Conclusion

High-speed PM electrical machines have been studied intensively and with greater interest in recent years. There are many references that are dedicated to their design, possible types of applications, loss estimation, and developing methods for electromagnetic, thermal, and mechanical analyses, as well as the examination of their power and speed capabilities. The references that deal with the general design considerations, practical applications, and loss calculation of high-speed PM electrical machines are numerous and they give a detailed view of the topics. New references are appearing every day that report the new challenges in the design, the new applications and the efforts to improve the efficiency of the machines. A contribution can be made to the existing methods for the thermal and mechanical analysis of the high-speed PM machines. There is an obvious lack of publications dealing with coupled heat-transfer and CFD analyses of the whole domain of an electrical machine. In fact, because of the highly specific thermal properties of the high-speed PM machines, there is a need for the simultaneous estimations of the turbulent phenomena in the fluid and thermal phenomena in the solid machine parts. Using CFD modelling, the local heat-transfer coefficients of convection on each surface of the machine can be numerically estimated, with a particular consideration of the inlet and outlet parts of the machine. The existing literature deals with CFD estimations of the local coefficients of convection only in the air-gap and end-winding regions of electrical machines. There is also a lack of comparative thermal and mechanical analyses of different rotor types in order to check which rotor construction will be the most suitable one for high-speed applications. The lack of references in which a complete electromagnetic-thermal-mechanical analysis is performed in order to determine the power-speed limits of the rated operation of high-speed PM machines is also obvious.

3 Methods for thermal and mechanical analysis

The methods for thermal and mechanical analysis are applied to a four-pole high-speed PM machine designed for a rated power P_r=130 kW and speed n_r=31,500 rpm intended for a compressor application. The supply voltage of the machine has a rectangular waveform. The machine uses airflow cooling. The rotor has a carbon-fibre sleeve as a retaining material and an aluminium cage for shielding the magnets from eddy currents. The permanent magnets are of the Nd-Fe-B type. The rotor is subcritical, it operates at a speed close to the first flexural critical speed, and it is supported on oil-film bearings.

3.1 Thermal analysis

Several modelling techniques that are used for the estimation of the temperature-rise distribution in the high-speed PM machine under consideration are elaborated in this chapter. The first method that is applied is a numerical-multiphysics method which couples the CFD and numerical heat-transfer calculations. At the beginning, this method considers the machine geometry as 2D axi-symmetric in order to estimate the turbulent and heat properties of the cooling fluid. The numerical estimation of the temperature distribution in the solid domain of the machine is performed by a 3D heat-transfer model. The aforementioned numerical techniques are based on the FEM and performed using the Comsol Multiphysics® software. The traditional thermal-network method based on analytical and semi-empirical equations is also used for the thermal analysis of the machine. The common input parameters for all the methods are the dimensions of the machine, the thermal properties of the machine parts, the properties of the cooling fluid, and the losses of the machine. The thermal coefficients of convection are input parameters only for the thermal network method and their mean values are calculated using empirical equations. The numerical multiphysics method uses values of these coefficients that are calculated using CFD. The algorithms of the methods for thermal analysis described in this chapter are explained in flow-chart in Appendix A.

3.1.1 Numerical modelling of the fluid domain

A multiphysics model that couples CFD and heat-transfer equations was created for modelling the fluid domain in the machine. The geometry of the fluid domain is considered to be 2D axi-symmetric. The airflow in the high-speed PM machine is desired to be turbulent since, in the case of a turbulent flow the heat extraction resulting from convection is much more effective than in a laminar flow. The flow of an incompressible fluid can be described by the Reynolds Averaged Navier-Stokes Equations (RANS):

$$\rho\frac{\partial \mathbf{V}}{\partial t} - \mu\nabla\cdot\nabla\mathbf{V} + \rho\mathbf{V}\cdot\nabla\mathbf{V} + \nabla p + \nabla\overline{(\rho\mathbf{v}'\otimes\mathbf{v}')} = \mathbf{F} \tag{3.1}$$

$$\nabla\cdot\mathbf{V} = 0 \tag{3.2}$$

Here μ denotes the dynamic viscosity, **V** is the averaged velocity field, **v** is the velocity vector, ρ is the density of the fluid, p is the pressure, and **F** is the volumetric force vector. The last term on the left-hand side in Equation (3.1) represents the fluctuations around a mean flow and is called the Reynolds stress tensor. The derivation of the governing equation for the Reynolds stress tensor in a general 3D case will introduce six additional equations and six additional unknowns that will complicate the solving of the problem. The solving procedure can be significantly simplified by introducing a closure of a turbulence model. One of the most commonly used turbulence models is the κ-ε model and it is also used for the CFD analysis that is performed here. The turbulent model gives a closure to the system and results in the following equations for the conservation of momentum and continuity:

$$\rho\frac{\partial \mathbf{V}}{\partial t}-\nabla\cdot\left[\left(\mu+\rho C_{\mu}\frac{\kappa^2}{\varepsilon}\right)\cdot\left(\nabla\mathbf{V}+(\nabla\mathbf{V})^{T}\right)\right]+\rho\mathbf{V}\cdot\nabla\mathbf{V}+\nabla p=\mathbf{F} \tag{3.3}$$

$$\nabla\cdot\mathbf{V}=0 \tag{3.4}$$

The two new variables in Equation (3.3) are the turbulent kinetic energy κ and the dissipation rate of the turbulent energy ε. Two extra equations for κ and ε are solved

$$\rho\frac{\partial \kappa}{\partial t}-\nabla\cdot\left[\left(\mu+\rho\frac{C_{\mu}}{\sigma_{\kappa}}\frac{\kappa^2}{\varepsilon}\right)\nabla\kappa\right]+\rho\mathbf{V}\cdot\nabla\kappa=\rho C_{\mu}\frac{\kappa^2}{2\varepsilon}\left(\nabla\mathbf{V}+(\nabla\mathbf{V})^{T}\right)^2-\rho\varepsilon \tag{3.5}$$

$$\rho\frac{\partial \varepsilon}{\partial t}-\nabla\cdot\left[\left(\mu+\rho\frac{C_{\mu}}{\sigma_{\varepsilon}}\frac{\kappa^2}{\varepsilon}\right)\nabla\varepsilon\right]+\rho\mathbf{V}\cdot\nabla\varepsilon=\rho C_{\varepsilon 1}\frac{\kappa}{2}\left(\nabla\mathbf{V}+(\nabla\mathbf{V})^{T}\right)^2-\rho C_{\varepsilon 2}\frac{\varepsilon^2}{\kappa} \tag{3.6}$$

The values of the model constants are: C_{μ} = 0.09, $C_{\varepsilon 1}$ = 1.44, $C_{\varepsilon 2}$ = 1.92, σ_{κ} = 0.9, and σ_{ε} = 1.3. They were determined from experimental data in the literature dealing with CFD.

The κ-ε turbulence model is isotropic, which means that it models the turbulence as being constant in all directions. This can be a good enough approximation for the parts of the fluid that are far from the solid walls. Close to the solid walls, the turbulence of the fluid cannot be considered as isotropic since the fluctuations in the turbulence vary greatly in magnitude and direction. The properties of the thin boundary layer near the solid wall are modelled by using an empirical relation between the values of velocity and wall friction. This approach is implemented and it has the best accuracy for high Reynolds numbers and cases in which pressure variations along the wall are not very large. If we assume a flow parallel to a solid wall, there is one velocity component parallel to the wall, which is a function of y, the coordinate perpendicular to the wall. Another assumption in this approach is that the flow close to the wall is not influenced by the flow in a region far from the wall. The complete set of boundary conditions for the solid wall is elaborated by Comsol Multiphysics® (2006) and the following boundary conditions for κ and ε are obtained:

$$\kappa = \frac{v_\tau^2}{\sqrt{C_\mu}}; \quad \varepsilon = \frac{v_\tau^3}{k_a y} \tag{3.7}$$

In Equation (3.7), v_τ is the friction velocity and $k_a \approx 0.42$ is the Kármán's constant.

When the machine is cooled, the heat is transferred by convection from the hotter rotor and stator surfaces to the cooler air in the turbulent flow. It means that the thermal interaction between the flow and the solid objects should be modelled. A multiphysics coupling between the turbulence and heat-transfer equations is performed. The thermal conductivity of the fluid is corrected in order to take into account the effect of mixing resulting from eddies. The turbulence results in an effective thermal conductivity, k_{eff}, described by the equations

$$k_{\text{eff}} = k_{\text{f}} + k_{\text{t}} \tag{3.8}$$

$$k_{\text{t}} = C_{\text{p}} \eta_{\text{t}} \tag{3.9}$$

in which k_{f} is the physical thermal conductivity of the fluid, k_{t} is the turbulent conductivity, η_{t} denotes the turbulent cinematic viscosity, and C_{p} is the heat capacity. On each boundary between the fluid and solid domains, the correct amount of heat flux across the boundary is calculated according to the equation

$$q = \frac{\rho C_{\text{p}} C_\mu^{1/4} \kappa_{\text{w}}^{1/2} \left(T_{\text{w}} - T_{\text{f}} \right)}{T^+} \tag{3.10}$$

where C_μ is a constant of the turbulence model and κ_{w} is the value of the turbulent kinetic energy at the wall. T_{w} is the temperature on the solid side of the wall, while T_{f} is the temperature of the fluid on the other side of the wall. The quantity T^+ is defined with the equation

$$T^+ = \frac{\text{Pr}_{\text{t}}}{0.41} \ln\left(y^+ \right) + 3.27 \tag{3.11}$$

Here Pr_{t} is the turbulent Prandtl number and y^+ is the dimensionless wall distance. The modelled fluid domain ends at the top of the laminar boundary layer, where the fluid experiences a significant wall-tangential velocity. The fluid velocity and temperature in the laminar sub-layer are not modelled. Instead of assuming a continuity of the temperature across the layer, there is a jump in the temperature from the solid surface to the fluid as a result of the omitted laminar sub-layer and T_{f} in Equation (3.10) is the temperature of the turbulent fluid close to the wall. If the local values of the heat flux $q_{\text{h local}}$ on a surface and the local temperatures of the solid wall $T_{\text{w local}}$ and fluid $T_{\text{f local}}$ are known, the local value of the coefficient of thermal convection is calculated using the equation

$$h_{\text{local}} = \frac{q_{\text{h local}}}{T_{\text{w local}} - T_{\text{f local}}} \tag{3.12}$$

The velocity, pressure, and temperature fields are solved simultaneously in the multiphysics model. More detailed mathematical description of the fundamentals of the CFD are given by Comsol Multiphysics® (2006) and Zienkiewicz et al. (2005).

A disadvantage of the κ-ε turbulence model is that it shows poor results in the description of rotating flows (Comsol Multiphysics® (2006)). This disadvantage can influence the accuracy of the CFD modelling of the turbulent flow in the air gap because the rotor accelerates the fluid to a tangential movement. A good circumstance in a high-speed machine is that the rotational movement of the fluid is undeveloped (Kousa et al. (2004)). Using the methods reported by Saari (1998) and Kousa et al. (2004), the rotating speed of the fluid can be calculated according to the surface speed of the rotor. Further, taking into account this rotating speed together with the axial speed of the fluid and the axial length of the machine, it is easy to calculate that the fluid makes only a small part of one rotation when passing through the machine under consideration. It will be illustrated by numerical and analytical calculations in Chapter 4. This means that the fluid does not have a developed rotational movement in the air gap and the κ-ε turbulence model can also be implemented in this part of the machine.

The finite-element mesh of the 2D axi-symmetric geometry of the high-speed PM machine and some main dimensions are presented in Figure 3.1. The mesh is refined at the boundaries between the solid and fluid domains and also close to the sharp corners. The idea of creating a 2D turbulent model was only to model the coolant flow in the machine and to estimate the temperatures in the flow and the coefficients of thermal convection. These fluid parameters can be considered as constant in the third (circumferential) direction and they can be used as input values in the 3D heat-transfer model. This will avoid the building of a 3D multiphysics model for the whole machine domain that couples CFD and heat-transfer analyses. This kind of model would require much greater computational resources and it could be much more time-consuming.

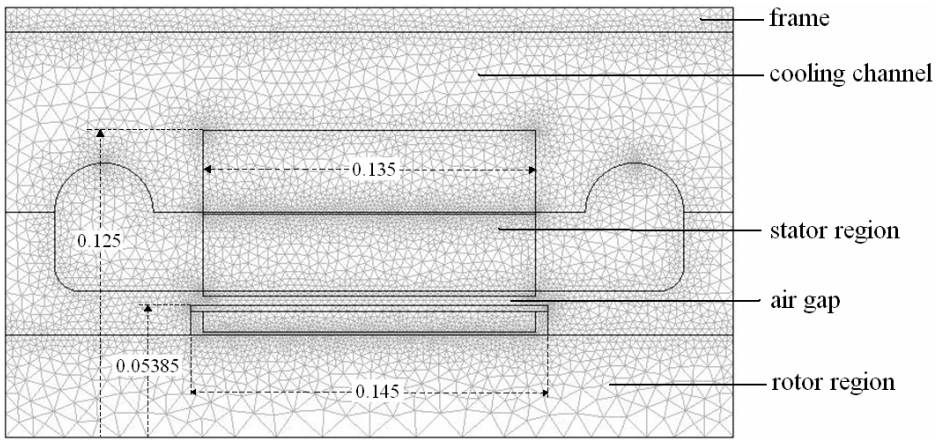

Figure 3.1: Finite-element mesh and main dimensions (rotor and stator lengths and radii) [m] of the 2D axi-symmetric geometry of the high-speed PM machine.

3.1.2 Numerical modelling of the solid domain of the machine

The 2D turbulent axi-symmetric model is quite rough for the thermal modelling of the solid domain of the high-speed PM machine. The areas of the machine that do not have axial symmetries cannot be successfully modelled in an axi-symmetric geometry. In fact, the domain of the magnets and the spaces between them filled with electrical conductor bars can be modelled only as a domain of equivalent average thermal conductivity between the two materials. The same way of modelling is valid for the stator teeth and slots. It means that the 2-D axi-symmetric model would estimate only the average temperature of the equivalent domain but it would not give the exact temperatures for the magnets and bars, separately. For all parts of the solid domain of the machine that have axi-symmetric geometry, the 2D axi-symmetric model can give reliable results.

The temperatures in the whole solid domain of the machine can be estimated by introducing a 3D numerical thermal model, the boundary conditions of which are dependent on the 2D axi-symmetric multiphysics model. The finite-element meshes of the 3D geometry of the machine rotor and stator are presented in Figure 3.2. The rotor and the stator are modelled separately in the 3D model but their mutual thermal influence is modelled in the 2D axi-symmetric multiphysics model. It was stated earlier that the fluid domain was not modelled in the 3D heat-transfer model. The fluid parameters, such as the fluid surface temperature and the heat-transfer coefficients of convection, are taken from the 2D axi-symmetric multiphysics model and they represent the input parameters for the boundary conditions of the 3D model. The phenomena on the surface of a solid machine part that is in contact with the cooling fluid are modelled using the boundary condition for the heat flux $\boldsymbol{q}_\mathrm{h}$

$$-\boldsymbol{n}_\mathrm{s} \cdot \boldsymbol{q}_\mathrm{h} = h\left(T_\mathrm{f} - T\right) + q_\mathrm{h0} \tag{3.13}$$

The heat-transfer coefficient of convection h on a surface is calculated in the 2D multiphysics model using Equation (3.12). The term q_h0 represents a general heat flux entering the domain and in this case it models the air-friction and cooling losses calculated using the method given by Saari (1995). The boundary condition that models an ideal thermal insulation or symmetry of the model is given by the equation

$$-\boldsymbol{n}_\mathrm{s} \cdot \boldsymbol{q}_\mathrm{h} = 0 \tag{3.14}$$

This boundary condition is used for modelling the boundaries at which the solid domain is thermally insulated. In this case there is no temperature gradient across the boundary and so the heat flux across the boundary is zero. This condition is used for modelling the symmetry of the machine in order to reduce the size of the model geometry. The prescribed constant temperature at a boundary is modelled by the boundary condition

$$T = T_0 \tag{3.15}$$

This condition is used for modelling a boundary of the machine at which the temperature T_0 is known in advance. The heat generation of an inner surface between two solid materials is modelled using the boundary condition

$$-\boldsymbol{n}_{\mathrm{s}} \cdot \left(\boldsymbol{q}_{\mathrm{h\,up}} - \boldsymbol{q}_{\mathrm{h\,down}} \right) = q_{\mathrm{h0}} \tag{3.16}$$

The heat flux q_{h0} generated on the inner surface can model the eddy-current losses at the surface of the eddy-current shield that is in contact with the carbon-fibre sleeve. If there is no heat generation at the boundary between two solid materials, $q_{\mathrm{h0}} = 0$. According to Equation (3.16), the difference between the normal heat fluxes on the upper and lower sides of the boundary is equal to the heat source.

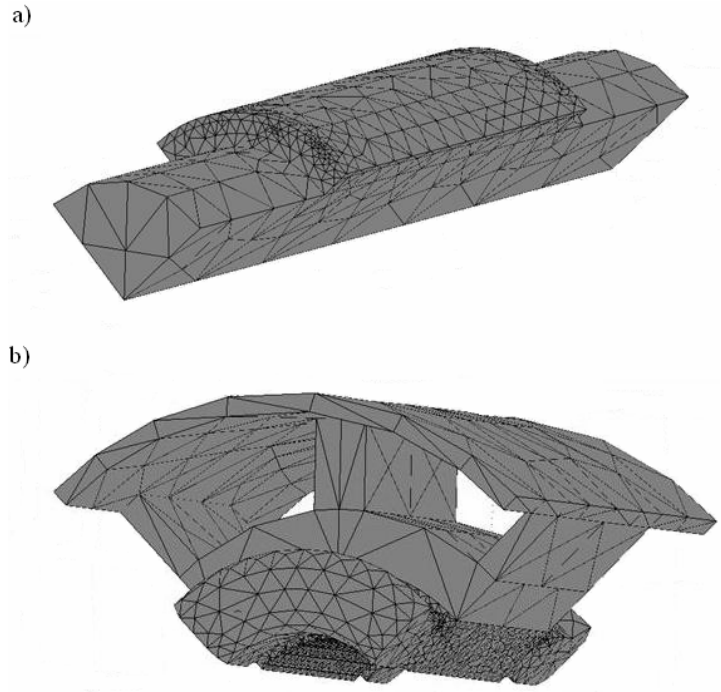

Figure 3.2: Finite-element mesh of the 3D geometry of the high-speed PM machine: a) rotor, b) stator.

3.1.3 Traditional thermal-network model

In addition to the previously described numerical methods, the traditional thermal-network method is also used for the thermal modelling of the solid and fluid parts of a high-speed PM machine. This method uses traditional analytical and semi-empirical approaches to thermal modelling and here it is used just for a comparison of its results with the results obtained by the numerical methods. This method is well elaborated and experimentally validated in many references and here it will be only briefly described. The thermal-network model that is used here is based on the equations given by Mellor et al. (1991) and Saari (1998). A thermal-network model of the high-speed PM machine under consideration is shown in Figure 3.3. The model consists of 112 thermal resistances connected to each other by 80 nodes. The heat generation resulting from the

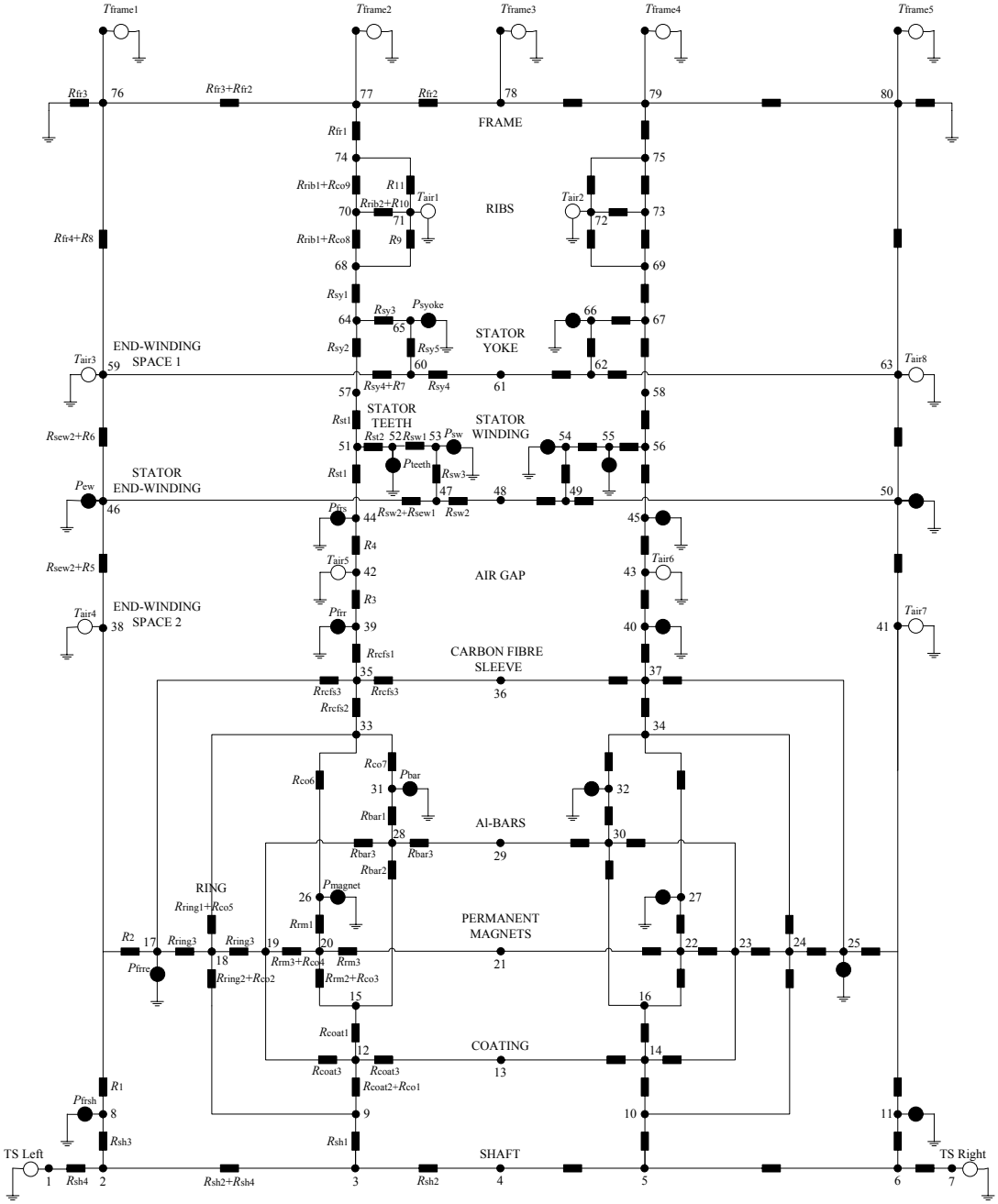

Figure 3.3: Thermal network of the high-speed PM machine.

losses is modelled by 20 heat sources and the boundary temperatures on the machine sides are modelled by 7 temperature sources. When the thermal circuit is being solved, the input parameters are the dimensions and thermal properties of the machine parts, the rotational speed, the airflow properties, the ohmic losses in the windings, and the electromagnetic losses calculated by the FEM. The air-friction and cooling losses, as well as the heat-transfer coefficients of convection, are calculated using analytical and empirical equations reported by Saari (1995), Saari (1998) and Incropera et al. (1990). Using the method reported by Jokinen and Saari (1997), the temperature rise in the fluid

flow is modelled using 8 heat-flow controlled temperature sources. This is an important task when a high-speed machine is modelled since the temperature rise in the flow cannot be neglected as it is quite high because of the huge loss density in the machine. This contributes to an asymmetrical temperature distribution in the machine, making the outlet part much hotter than the inlet part of the machine. All equations for the thermal resistances as well as other data about the developed thermal-network model are given in Appendix B. The thermal circuit is solved for the temperatures at each node, which is in fact the average temperature rise in each part of the machine. The temperature rise for each node of the network is calculated according to the next matrix equation:

$$\mathbf{T} = \mathbf{G}_{\mathrm{T}}^{-1}\mathbf{P} \tag{3.17}$$

Here $\mathbf{T}$ is the temperature matrix, $\mathbf{G}_{\mathrm{T}}$ is the thermal conduction matrix, and $\mathbf{P}$ is the loss matrix.

3.2 Rotordynamics analysis

The rotordynamics analysis in this thesis is based on the FEM. The examined rotor (Figure 3.4) is modelled in beam-like and 3D geometries. The beam-like model of the rotor under examination is presented in Figure 3.5. A basic description of the determination of the deformed shape, critical speeds, and the unbalance response, as well as some discussion about the effects of rotation and the implementation of 3D rotordynamics models, is given below. More details about the method applied here are given by Genta (2005). The displacement of a point with coordinates *x, y, z* is assumed:

$$\mathbf{u}(x,y,z,t) = \mathbf{N}(x,y,z)\mathbf{q}(t) \tag{3.18}$$

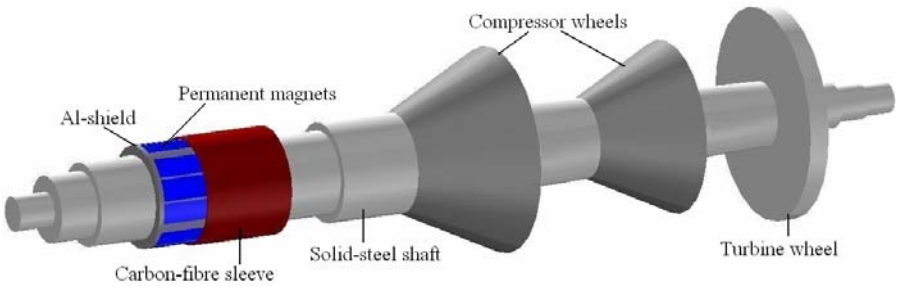

Figure 3.4: Geometry of the examined rotor.

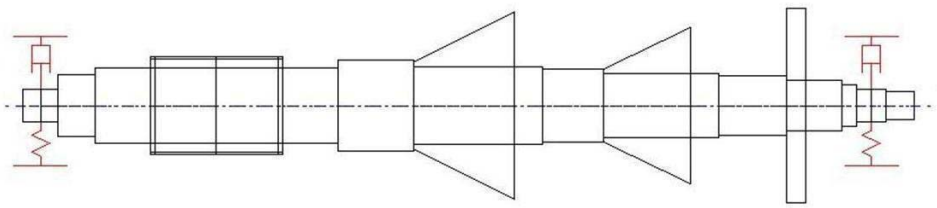

Figure 3.5: Beam-like model of the rotor geometry.

In a general case, the displacement **u** is a vector defined in three dimensional space and time *t*. It may be of a higher order if it also includes the rotations. **N** is the matrix that contains the shape functions and **q** is a vector in which the generalised coordinates of the element are listed. Because the shape functions are time invariant, the generalised velocities can be expressed as

$$\dot{\mathbf{u}}(x,y,z,t) = \mathbf{N}(x,y,z)\dot{\mathbf{q}}(t) \tag{3.19}$$

If the system is undamped, discrete and non-rotating, the equation of motion of the element is

$$\mathbf{M}\ddot{\mathbf{q}} + \mathbf{K}\mathbf{q} = \mathbf{f}(t) \tag{3.20}$$

Here **M** is the mass matrix, **K** is the stiffness matrix and **f** is the vector that contains all the forces acting on the element. If the matrices of each element *j* are computed, it is possible to obtain the mass matrix **M**, gyroscopic matrix **G**, stiffness matrix **K** and force matrix **f** of the whole rotor structure when the structure of the elements is assembled. Because the kinetic and potential energies of the whole structure can be obtained simply by adding the energies of the various elements, it follows that

$$\mathbf{M} = \sum_j \mathbf{M}_j, \quad \mathbf{G} = \sum_j \mathbf{G}_j, \quad \mathbf{K} = \sum_j \mathbf{K}_j, \quad \mathbf{f} = \sum_j \mathbf{f}_j \tag{3.21}$$

The general equation of an axi-symmetrical rotor that is rotating with an angular speed Ω is

$$\mathbf{M}\ddot{\mathbf{q}} + (\mathbf{C}_\mathrm{n} + \mathbf{C}_\mathrm{r} - \mathrm{i}\Omega\mathbf{G})\dot{\mathbf{q}} + (\mathbf{K} + \Omega^2\mathbf{K}_\Omega - \mathrm{i}\Omega\mathbf{C}_\mathrm{r})\mathbf{q} = \Omega^2\mathbf{f}_\mathrm{r}e^{\mathrm{i}\Omega t} + \mathbf{f}_\mathrm{n}(t) \tag{3.22}$$

$\mathbf{C}_\mathrm{n}$ and $\mathbf{C}_\mathrm{r}$ are matrices of non-rotating and rotating damping, respectively. The term $\Omega^2\mathbf{K}_\Omega$ takes the centrifugal stiffening into account and i is the imaginary unit. The term $\mathbf{f}_\mathrm{r}$ is a rotational force caused by the unbalance and $\mathbf{f}_\mathrm{n}$ is a non-rotational force vector that is a function of time.

The computation of the deformed shape is performed by the static solution of the problem. The static displacement is obtained by leaving the vector of non-rotating forces on the right-hand side of Equation (3.22) and omitting the terms that contain the time derivatives

$$(\mathbf{K} + \Omega^2\mathbf{K}_\Omega - \mathrm{i}\Omega\mathbf{C}_\mathrm{r} - \mathrm{i}\mathbf{K}''_\mathrm{r})\mathbf{q} = \mathbf{f}_\mathrm{n} \tag{3.23}$$

The new term $\mathbf{K}''_\mathrm{r}$ is the hysteretic damping matrix, i.e. the imaginary part of the complex stiffness matrix related to the rotating part of the system in the equation of motion. Equation (3.23) takes the centrifugal stiffening into account.

The computation of the critical speeds is performed in the free whirling mode, when the system is considered to be undamped. In this case, all the damping matrices in the homogenous Equation (3.22) are set to zero. If the free circular whirling has a solution of the type $\mathbf{q}=\mathbf{q}_0 e^{i\Omega t}$, the following homogenous equation is obtained:

$$\left(-\Omega^2\left(\mathbf{M}-\mathbf{G}\right)+\mathbf{K}\right)\mathbf{q}_0=0 \tag{3.24}$$

The critical speed of the system is determined when the following eigenproblem is solved:

$$\det\left(-\Omega^2\left(\mathbf{M}-\mathbf{G}\right)+\mathbf{K}\right)=0 \tag{3.25}$$

The unbalance response can be obtained by computing a particular integral of Equation (3.23), in the form $\mathbf{q}=\mathbf{q}_0 e^{i\Omega t}$. For a damped system, the equation for the determination of the unbalance response is

$$\left(-\Omega^2\left(\mathbf{M}-\mathbf{G}\right)+i\Omega\mathbf{C}_n+\mathbf{K}\right)\mathbf{q}_0=\Omega^2\mathbf{f}_r \tag{3.26}$$

If the system is undamped, Equation (3.26) does not give any solution when the spin speed is equal to the critical speed of the system. The computation of the unbalance response in a rotational system is similar to the computation of the unbalance response of a vibrating system excited by a harmonic forcing function.

In order to consider the effects of the rotation of the system, it is necessary to calculate the whirl frequencies of the system as functions of the spin speed, i.e. to plot the Campbell diagram. The damping should be taken into account when the stability of the system is studied. In the case of viscous damping, the basic equation is the homogeneous equation

$$\mathbf{M}\ddot{\mathbf{q}}+\left(\mathbf{C}_n+\mathbf{C}_r-i\Omega\mathbf{G}\right)\dot{\mathbf{q}}+\left(\mathbf{K}+\Omega^2\mathbf{K}_\Omega-i\Omega\mathbf{C}_r\right)\mathbf{q}=0 \tag{3.27}$$

The roots locus can be obtained by computing the eigenvalues of the dynamic matrix

$$\begin{bmatrix} -\mathbf{M}^{-1}\left(\mathbf{C}_n+\mathbf{C}_r-i\Omega\mathbf{G}\right) & -\mathbf{M}^{-1}\left(\mathbf{K}+\Omega^2\mathbf{K}_\Omega-i\Omega\mathbf{C}_r\right) \\ \mathbf{I} & 0 \end{bmatrix} \tag{3.28}$$

In order to take the structural damping into account, it is sufficient to add the expression $\pm i\mathbf{K}''_n \pm i\mathbf{K}''_r$. It is possible to obtain the complex whirl frequencies as eigenvalues of the matrix

$$\begin{bmatrix} \mathbf{M}^{-1}\left(\Omega\mathbf{G}+i\mathbf{C}_n+i\mathbf{C}_r\right) & \mathbf{M}^{-1}\left(\mathbf{K}+\Omega^2\mathbf{K}_\Omega\pm i\mathbf{K}''_n\pm i\mathbf{K}''_r-i\Omega\mathbf{C}_r\right) \\ \mathbf{I} & 0 \end{bmatrix} \tag{3.29}$$

The matrix in Equation (3.29) shows that there are various effects that can cause a change in the critical speeds as a result of the rotation of the rotor. The gyroscopic effect can cause an increase in the forward whirl speed and a decrease in the backward whirl speed (in terms of absolute values). The centrifugal stiffening is another effect that can increase the whirl speed of the forward and backward whirling. The effect of the rotating damping on the whirl speed is usually negligible. The forward and backward whirl speeds are determined by plotting the Campbell diagram. If structural damping is present, several eigenproblems with the different signs included in Equation (3.29) must be solved for each value of the spin speed. After obtaining the solutions, the real part of the various solutions should be located in the Campbell diagram.

The beam-like modelling of rotor structures with axial symmetries is the most typical for rotordynamics because it is simple and not very time consuming and usually yields to results that are accurate enough for most practical purposes. If the rotor being modelled does not have an axial symmetry, three-dimensional modelling is required. In many cases of rotordynamics, a good circumstance is that the rotors have cyclic axial symmetries i.e. they can be considered as being made up of a number of identical sectors. Any cyclic symmetry with an order equal to or higher than three is equivalent to a symmetry with an infinite order, i.e. to an axial symmetry (Genta (2005)). A body that has a cyclic symmetry with an order equal to or higher than three is dynamically equivalent to a disc and can be modelled as a circular beam. Because the machine under consideration has four poles, the geometry of the rotor has a cyclic symmetry of an order of four and this part of the rotor can be modelled as an equivalent disc in a beam-like model. To make the analysis more reliable and to check the validity of the beam-like model, a 3D model of the rotor is made. The model contains the real 3D geometry of the solid-steel shaft, the permanent magnets, the aluminium shield and the carbon-fibre sleeve. The finite-element mesh of the 3D model is presented in Figure 3.6.

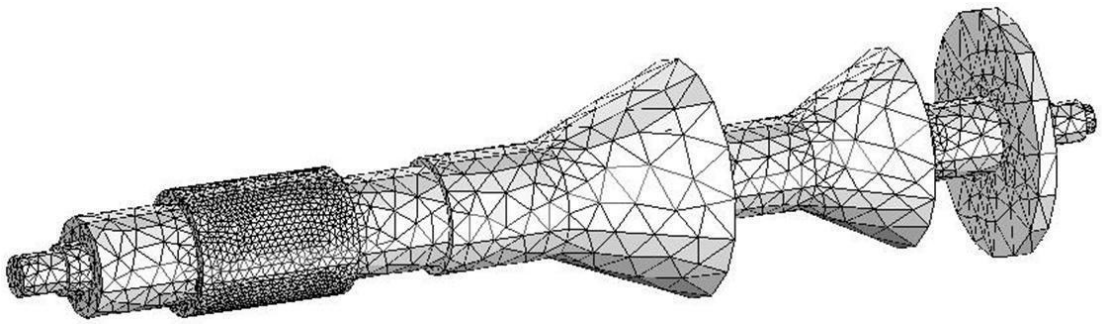

Figure 3.6: Finite-element mesh of the 3D geometry of the rotor.

4 Results

The results shown in this chapter are related to the rated operating point of the machine under examination. The rated data of the machine are shown in Table 4.1.

Table 4.1: Rated operating data of the examined high-speed PM machine.

Speed	n_r=31,500 rpm
Power	P_r=130 kW
Voltage	U_r=400 V
Current	I_r=210 A
Winding connection	delta
Displacement factor	$cos\ \varphi$=0.98
Torque (air gap)	T_{ag}=43.8 Nm
Rotor temperature	T_{rot}=80^{0}C
Stator temperature	T_{stat}=100^{0}C

4.1 Results for the losses

The methods used for the determination of the temperature rises in the high-speed PM machine use common input values for the losses that are generated in the machine. The electromagnetic losses are determined using the FEM (Arkkio (1987)) and the mechanical losses were calculated with empirical equations (Saari (1995)). The results for all types of losses generated for rated performance of the machine are presented in Table 4.2. The stator core losses are increased by 50% due to the punching and welding factors.

Table 4.2: Results for all types of losses generated for rated performance of the high-speed PM machine.

Types of losses		Power [W]
Electromagnetic losses	Resistive losses in the permanent magnets	123
	Resistive losses in the aluminium cage	135
	Resistive losses in the stator winding	936
	Core losses in the stator yoke	335
	Core losses in the stator teeth	355
Mechanical losses	Air-friction losses in the air gap	166
	Air-friction losses on the rotor end-disks	72
	Air-friction losses on the rotor end-shafts	76
	Air-friction losses in the fluid passages	23
	Losses of rotational acceleration of the fluid	295

4.2 Results for the fluid domain of the machine

The air used for supplying the compressor first passes through the electrical machine as a coolant. When it flows through the machine, it is divided into two parts. The main part

of the coolant flows in the channel between the stator yoke and the frame of the machine. This amount is q_1=2 m^3/s. One small part of the coolant flows in the air gap, extracting the heat which is generated in the rotor and some of the heat generated in the stator. This flow is estimated to be q_2 = 0.05 m^3/s. The axi-symmetric representation of the geometry of the fluid domain can be justified if we take into account the fact that the rotational flow in the air gap is not fully developed. This can be checked by making a 3D CFD model of the fluid flow in the air gap. The results obtained from this model are presented in Figure 4.1. From Figure 4.1.a we can see that the flow makes a small part of one rotation when passing through the air gap, it is just deflected. As we can see in Figure 4.1.b, the initial speed of the flow when entering the air gap is about v_{f1}=40 m/s and the flow is accelerated to a total speed of about v_{f2}=45 m/s, which is a superposition of the axial and tangential components. The part of the fluid that is close to the rotor surface is accelerated more than the part of the fluid that is close to the stator surface. The high axial speed of the flow and the short axial length of the machine make the time that is needed by the flow to pass through the machine very short and not long enough for the flow to develop a spiral movement. The tangential component of the flow movement is minor when compared to the axial component. The same can be proven using analytical equations. The tangential velocity of the flow can be expressed as a product between the velocity factor of the flow k_2 and the surface speed v_s of a rotor with outer radius r_r rotating at rotational speed n

$$v_t = k_2 v_s = k_2 \Omega r_r = k_2 2\pi \frac{n}{60} r_r \tag{4.1}$$

If the fluid enters the air gap with axial speed $v_a = v_{f1}$, the time needed for the flow to pass through the effective axial length of the rotor l_r is l_r/v_a. The ratio between the path of the flow in tangential direction and one full rotation around the rotor is

$$\frac{v_t t}{2\pi r_r} = \frac{k_2 2\pi \frac{n}{60} r_r \frac{l_r}{v_a}}{2\pi r_r} = k_2 \frac{n l_r}{60 v_a} = 0.15 \frac{31{,}500 \cdot 0.135}{60 \cdot 40} = 0.27 \tag{4.2}$$

In Equation (4.2), the velocity factor k_2=0.15 for high-speed machines is defined by Saari (1998). The equation shows that the flow makes only 27% of one rotation while passing through the machine. We can conclude that only the axial component of the flow can be considered to be dominant and the fluid domain in the air gap can be modelled in the 2D axi-symmetric model.

Results for the temperature rise distribution of the fluid and the velocity field of the coolant flow are presented in Figure 4.2. The inlet side of the machine is on the left and the outlet side is on the right-hand side. Figure 4.2.a shows that the temperature rise of the fluid cannot be neglected since it extracts a huge amount of heat as a result of the very high loss density which is typical for high-speed electrical machines. As we can see later, this temperature rise in the fluid causes a higher temperature rise in the solid parts of the machine that are close to the outlet side.

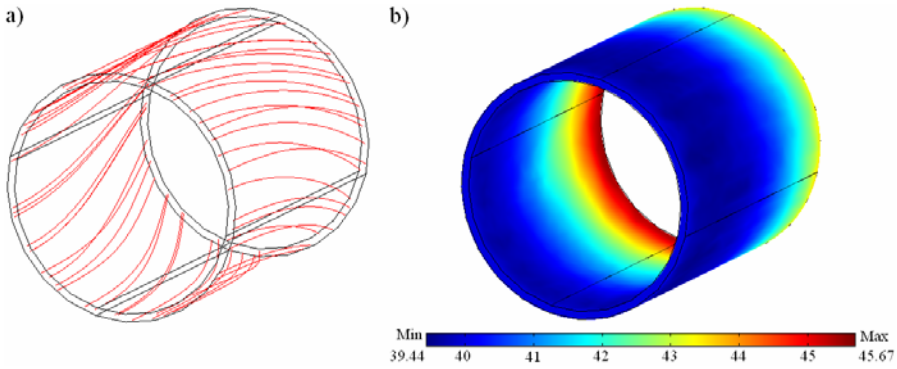

Figure 4.1: Results from the 3D modelling of the fluid flow in the air gap: a) streamlines of the fluid flow; b) magnitude of velocity field v [m/s] of the flow.

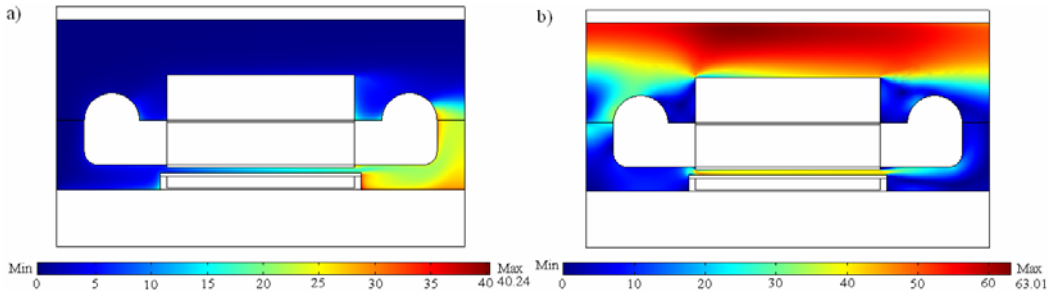

Figure 4.2: Results for the fluid domain: a) distribution of the temperature rise ΔT [K]; b) velocity field v [m/s] of the coolant flow.

Another important parameter that is obtained with this method is the coefficient of thermal convection on each surface between the solid and fluid domains. The local value of this coefficient is calculated in the postprocessor using Equation (3.12). The local heat-transfer coefficient is presented as a function of either the axial or radial position along the flow of the fluid. The local coefficients of thermal convection in the air gap (rotor and stator surface), end-shafts, rotor end-discs, end-windings (outer and inner surface), yoke end-discs and the space between the stator yoke and frame are presented in Figures 4.3-4.9, respectively. In this way, all the local heat-transfer coefficients of convection over all the outer surfaces of the solid domain in the machine are determined. The values of the local coefficients of thermal convection on the rotor and stator surfaces in the air gap are very close to each other (Figure 4.3). The peaks in Figure 4.3 are due to the increased turbulence that occurs around the edges when the fluid enters and leaves the air gap. Large fluctuations occur in Figures 4.6 and 4.7 in the regions of the round parts of the end-windings. These peaks and strong fluctuations that can be seen in all the Figures 4.3-4.9 are mainly due to the changes in geometry which influences the level of turbulence and due to the nature of the method. The coefficient of convection on the end-shafts, rotor end-discs, end-windings and yoke end-discs is determined for the inlet side and outlet side surfaces, separately. We can conclude that the convection is more effective at the inlet side of each surface and this also contributes for higher temperature rise in the solid parts of the machine that are close to the outlet.

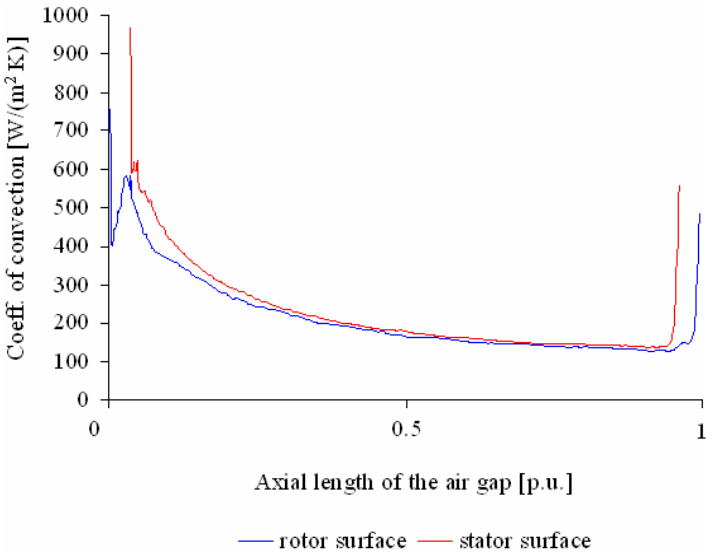

Figure 4.3: Local coefficient of thermal convection h_{loc} [W/(m^{2}K)] on the rotor and stator surfaces in the air gap. The direction of the flow is from left to right.

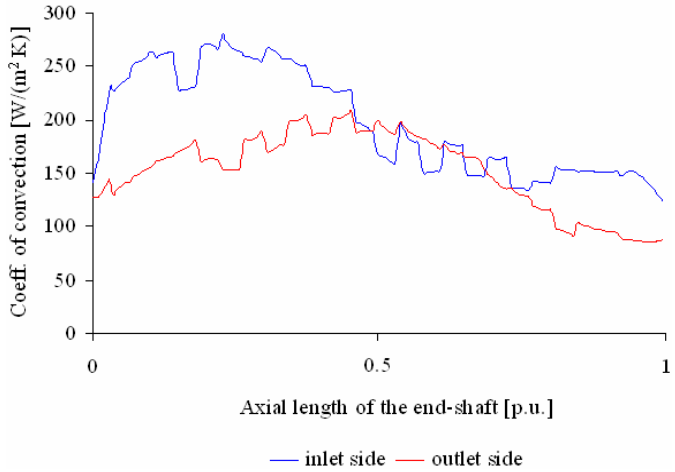

Figure 4.4: Local coefficient of thermal convection h_{loc} [W/(m^{2}K)] on the end-shaft surfaces.

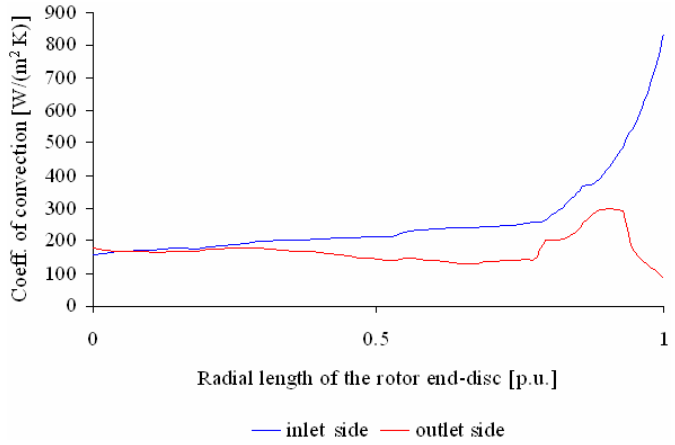

Figure 4.5: Local coefficient of thermal convection h_{loc} [W/(m^{2}K)] on the rotor end-discs surfaces.

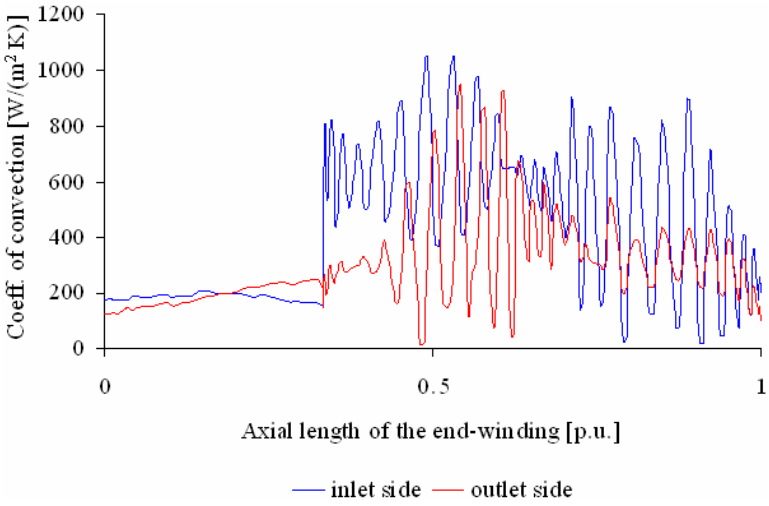

Figure 4.6: Local coefficient of thermal convection h_{loc} [W/(m^{2}K)] on the outer end-winding surface.

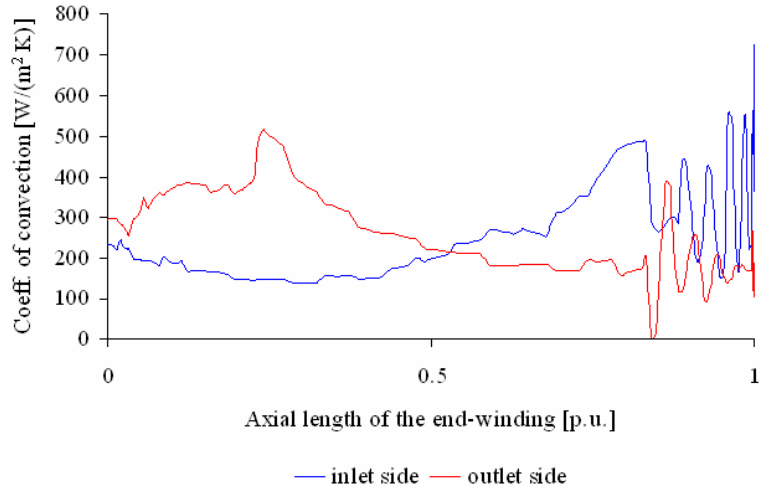

Figure 4.7: Local coefficient of thermal convection h_{loc} [W/(m^{2}K)] on the inner end-winding surface.

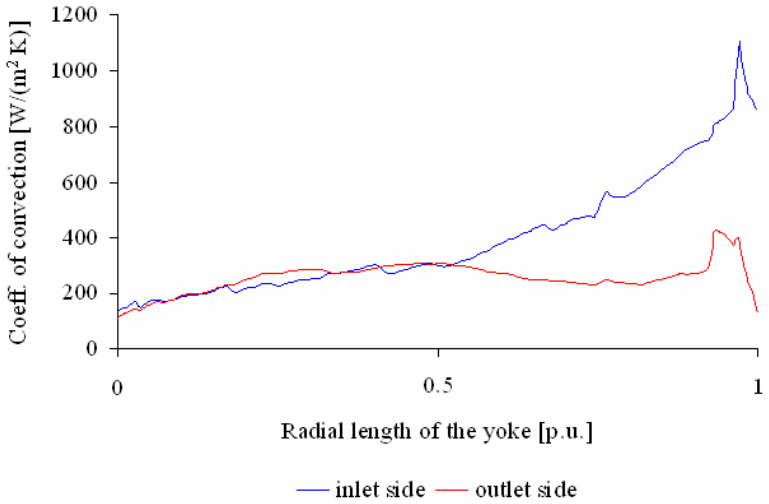

Figure 4.8: Local coefficient of thermal convection h_{loc} [W/(m^{2}K)] on the yoke end-discs surfaces.

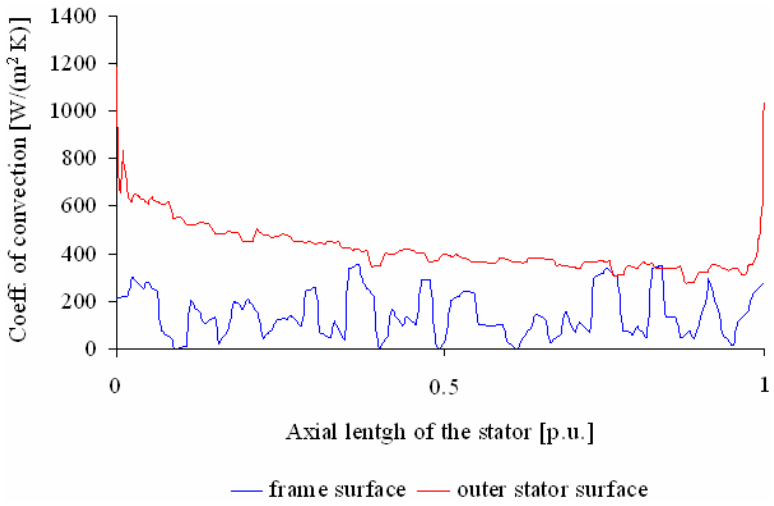

Figure 4.9: Local coefficient of thermal convection h_{loc} [W/(m^{2}K)] on the frame and outer stator surfaces.

4.3 Results for the temperature rise in the solid domain of the machine

The final 3D view of the temperature rise distribution in all parts of the machine is obtained from the 3D heat-transfer model. Using boundary conditions for symmetry, only a quarter of the machine (one pole pitch) has been modelled. The temperature-rise distribution in the inner rotor geometry is presented in Figure 4.10.a. Figure 4.10.b presents the temperature-rise distribution at the rotor boundaries. The temperature-rise distributions in the inner stator geometry and at the stator boundaries are presented in Figure 4.11. The results are related to the rated performance of the machine. It is obvious that the outlet part of the machine is much hotter than the inlet one because of the asymmetrical temperature distribution in the fluid domain and the unequal coefficient of thermal convection.

4.4 Comparison of the results obtained with the different methods for thermal analysis of the machine

The distribution of the temperature rises in the machine was estimated using a 2D multiphysics method, 3D heat-transfer method, and a traditional thermal-network method. Below, the results for the temperature rises in the machine obtained with the different methods will be compared. Because the 3D heat-transfer method for estimation of the temperature rise in the solid-part of the machine is dependent on the 2D multiphysics method, these two methods can be considered together as a numerical-multiphysics method. The temperature rise of the airflow along the air gap is estimated

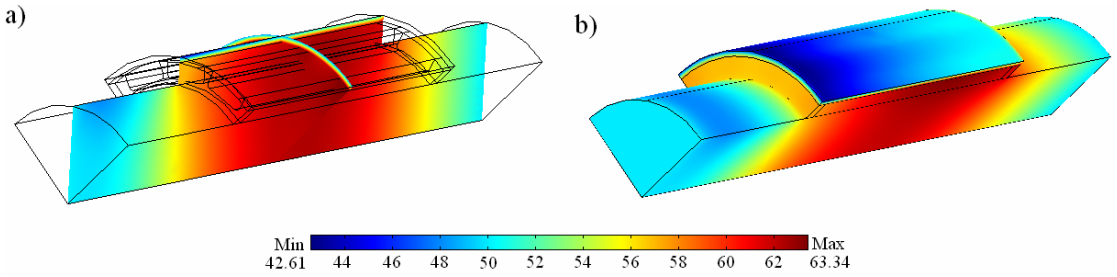

Figure 4.10: Calculated temperature-rise distribution ΔT [K] of the rotor: a) inner geometry; b) outer surface.

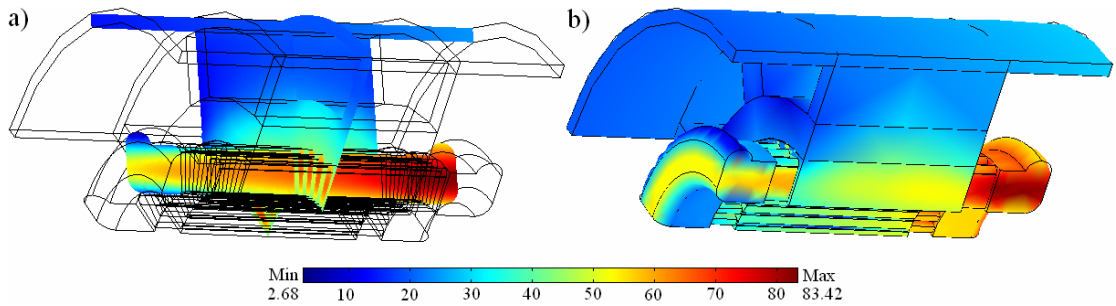

Figure 4.11: Calculated temperature-rise distribution ΔT [K] of the stator: a) inner geometry; b) outer surface.

using the 2D multiphysics model. These values are compared with the thermal-network method and presented in Figure 4.12.a. A comparison of the results that are obtained with the different methods for the temperature rises in the rotor shaft, aluminium cage, permanent magnets, carbon-fibre sleeve, stator winding, stator teeth, and stator yoke is presented in Figures 4.12.b-h, respectively. The best agreement between the results is achieved during the estimation of the temperature rises in the rotor parts. There are certain deviations among the results because the methods implemented have a completely different nature and because of the vagueness in the determination of the coefficients of thermal convection. The average values of the heat-transfer coefficients of convection for different cooling surfaces in the machine determined by using the numerical-multiphysics method and semi-empirical equations are presented in Table 4.3. The numerical results presented in the table are average values of the local coefficients of convection presented in Figures 4.3-4.9. The values of the coefficients of convection that are used in the thermal-network method are obtained with semi-empirical equations presented by Saari (1995), Saari (1998) and Incropera et al. (1990).

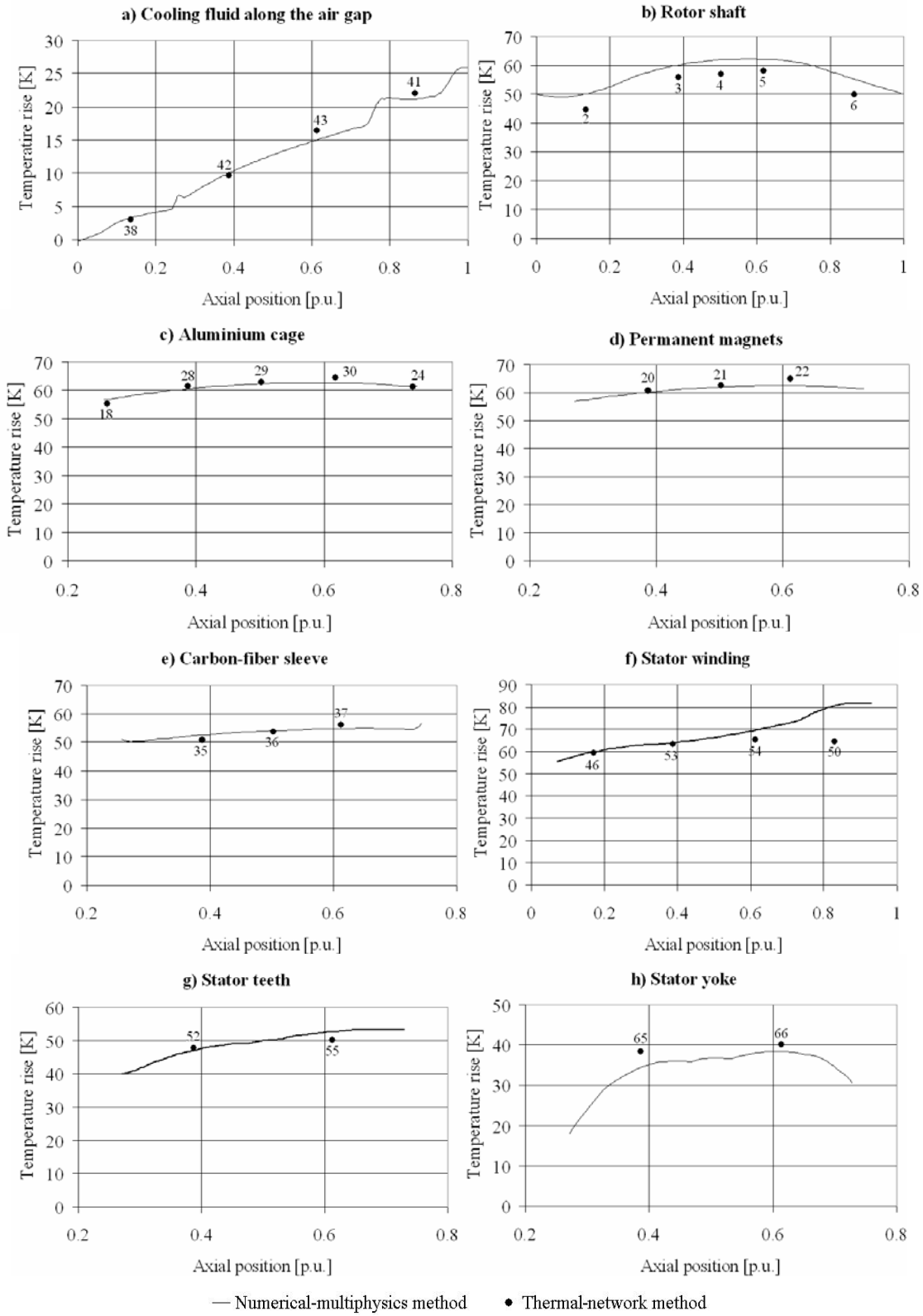

Figure 4.12: Comparison of the results for the temperature rises ΔT [K] in different parts in the machine predicted by the numerical-multiphysics method and the thermal-network method. Next to the results obtained with the thermal-network method is the number of the node that corresponds to Figure 3.3.

Table 4.3: Average values of the heat-transfer coefficients of convection h_{avg} [W/(m^{2}K)] for different cooling surfaces in the machine obtained using the numerical-multiphysics and thermal-network methods.

Cooling surface	Numerical-multiphysics	Semi-empirical
Air gap	231	276
Rotor end-discs	242	362
Rotor end-shaft	175	194
End-winding – inner side	280	221
End-winding – outer side	365	213
Yoke end-disc	335	266
Yoke and frame	293	182

4.5 Results from the rotordynamics analysis of the machine

During the rotordynamics analysis of the machine, the first four critical modes are considered: the first two rigid modes and the first two flexural modes. The first rigid mode (Figure 4.13.a) has a cylindrical shape and the second rigid mode (Figure 4.13.b) has a conical shape. The first and second flexural mode shapes are presented in Figure 4.13.c and d, respectively. The forward and backward values determined for the first four critical speeds are presented in Table 4.4. In each cell of the table, there is a range of critical speeds. The values range from a case in which the rotor elements (permanent magnets, Al-shield, and sleeve) do not contribute to the stiffness of the solid-steel shaft to a case in which they contribute fully to the stiffness. In the former case, these elements were modelled with zero stiffness and in the later case with their actual stiffness. The degree of contribution to the stiffness of the rotor shaft is difficult to predict since it depends on many factors, such as the quality of the manufacturing, the shrink-fitting of the rotor elements, the rotation speed, temperature, etc (Chen and Gunter (2005)). The real value of the critical speed is expected to be within the range. For calculation of the rigid modes, the value of the bearing stiffness was k=1.2·10^7 N/m and for calculation of the flexural modes, a value of k=2.2·10^7 N/m was used.

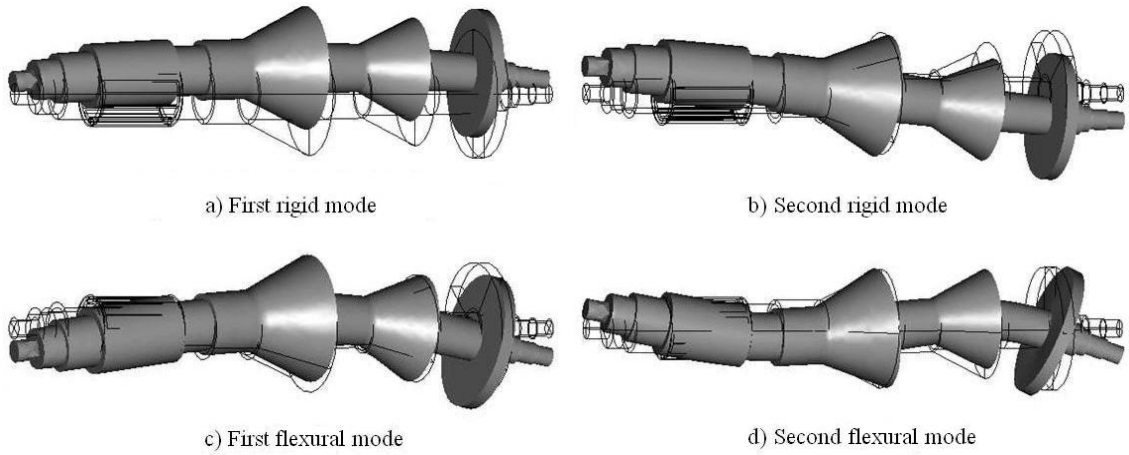

Figure 4.13: Mode shapes of the first four critical speeds of the examined high-speed rotor.

Table 4.4: Results for the forward and backward critical speeds n_c [rpm] of the examined high-speed rotor.

Direction	First rigid	Second rigid	First flexural	Second flexural
Fwd	6,073-6,106	10,200-10,343	35,833-36,249	76,107-81,287
Bwd	6,067-6,100	9,822- 9,945	30,791-30,999	52,636-54,429

5 Comparative thermal and mechanical analyses of rotor structures with different types of retaining sleeves

The retaining sleeves provide some key performance properties in high-speed PM machines, not only from the mechanical but also from the electrical and thermal points of view. A good retaining material must have a high allowed stress and low density in order to provide good retention of the magnets against the centrifugal forces that arise during the high-speed operation. Retaining material with a higher mechanical strength enables the retaining sleeve to be thinner. This is desirable from a thermal point of view since it provides better cooling of the inner rotor parts. The properties of the retaining material have a strong influence on the thermal behaviour of the rotor since most of the heat that is generated in the rotor must be transferred through the sleeve in order to be dissipated in the air gap. It means that a retaining material with a high thermal conductivity will enable the rotor to be cooled effectively. The electrical conductivity of the retaining material affects the eddy-current generation in the rotor.

The carbon-fibre-composite material is very frequently used as a material for retaining sleeves in high-speed PM machines. The main property that makes it very useful in this application is its high strength to weight ratio. It has a very low electrical conductivity, which results in a low generation of eddy-current losses in the sleeve. The drawback of this property is that it does not have any shielding effect. In fact, it must be used in combination with a shield made of an electrically highly conductive material in order to reduce the eddy currents in the magnets. Another drawback of the carbon-fibre material is its very low thermal conductivity, which makes the cooling of the inner rotor parts difficult. Another retaining material that is used in high-speed PM applications is titanium. Titanium alloys have a high tensile strength and better thermal conductivity than the carbon-fibre material. Their drawback is their higher electrical conductivity, which results in the generation of high eddy-current losses in the sleeve.

The aim of the comparative thermal and mechanical analyses is to examine the possibility of using titanium alloys, which besides the role of magnet retention, will also provide a shielding function from eddy-current loss generation in the magnets, and also to examine their influence on the rotordynamics behaviour of the rotors. Two different titanium alloys with different mechanical, thermal, and electrical properties are examined. The first one is the alloy Ti-6%Al-6%V-2%Sn and the second one is the alloy Ti-2.5%Cu. The results of the thermal and mechanical analyses in the cases when these alloys are used are compared with the results when a carbon-fibre material is used for a retaining sleeve. The analyses of the three different types of sleeves are performed on three high-speed PM machines designed for the same speed n=31,500 rpm and mechanical power P=130 kW. The differences in the construction of the machines are only in the type of the sleeve. The most important mechanical, thermal, and electrical properties of the materials used for the retaining sleeves are listed in Table 5.1.

Table 5.1: Properties of the materials for retaining sleeves.

Retaining material:	Proof stress [MPa]	Young's modulus [Pa]	Density [kg/m^3]	Thermal cond. [W/(K·m)]	Electrical cond. [S/m]
Carbon fibre - epoxy 70 %-30 %	800	$1.25 \cdot 10^{11}$ [1]	1,800	0.87 [2]	≈0
Titanium alloy Ti-6%Al-6%V-2%Sn	1,000	$1.16 \cdot 10^{11}$	4,540	7.20	$6.37 \cdot 10^5$
Titanium alloy Ti-2.5%Cu	540	$1.16 \cdot 10^{11}$	4,560	16.00	$13.30 \cdot 10^5$

5.1 Comparative thermal analysis of the different rotor structures

The results for the rotor resistive losses and temperature rises that are shown here are related to the steady state performances of the three different machines. During the analysis, the outer diameters of all the three rotor types are kept the same since they should fit the same stator. It means that the three rotor types have the same radial air gap length, the same amounts of air-friction losses, and the same constants of thermal convection on the rotor surface. In all three cases, this will provide the same thermal properties for the coolant and a more objective comparison between the thermal behaviours of all the rotor types can be made. The dimensions of the inner rotor parts are not the same. The retaining sleeves do not have the same thickness because the mechanical strengths of the materials used are different. The dimensions of the magnets are not the same in the three different cases. For instance, in the case of a thinner sleeve without a shield, less material is needed for the permanent magnets in order to achieve the same power for the machine because the magnetic reluctance is reduced and the magnets are closer to the stator.

The results for the calculated electromagnetic losses in different parts of the three types of rotor constructions are presented and compared in Table 5.2. The distribution of the temperature rises inside the rotor and at the rotor boundaries for the three types of rotor constructions determined by the numerical-multiphysics method is presented in Figure 5.1. Separate results for the temperature rises in the permanent magnets, retaining sleeve, rotor shaft, and the cooling fluid along the air gap are obtained with the implementation of the numerical-multiphysics and traditional thermal-network methods and they are presented in Figure 5.2.

[1] Young's modulus of the whole helical structure of the sleeve.
[2] Thermal conductivity in direction normal to fibres.

Table 5.2: Calculated eddy-current losses [W] in the rotors.

Part of the rotor	Type of rotor according to the retaining material		
	Carbon fibre	Titanium alloy Ti-6%Al-6%V-2%Sn	Titanium alloy Ti-2.5%Cu
Permanent magnets	123	229	128
Sleeve	≈0	353	734
Eddy-current shield	135		
Solid-steel shaft	≈0	≈0	≈0

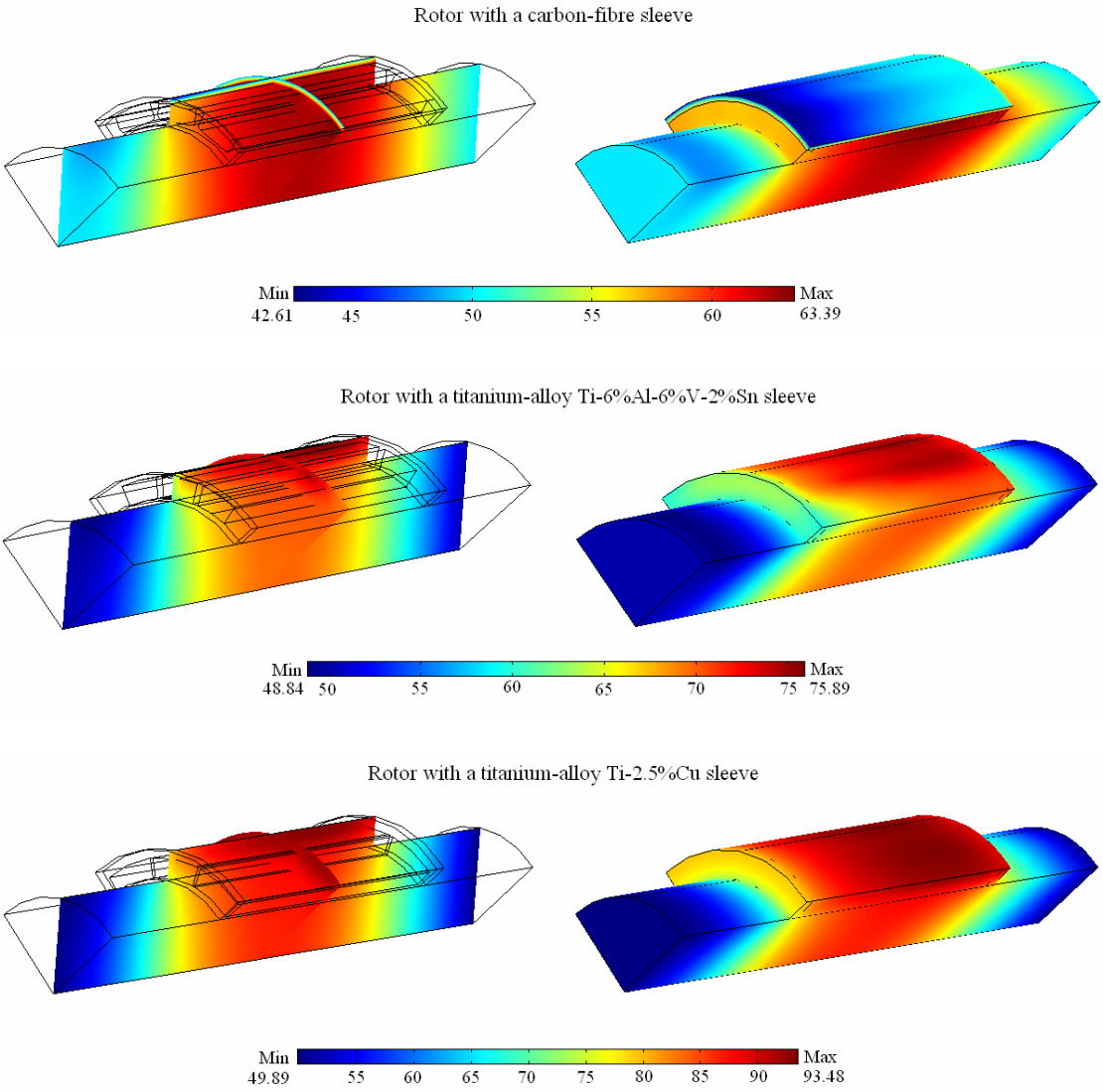

Figure 5.1: Distribution of the temperature rises ΔT [K] inside the rotor and at the rotor boundaries for the three different types of rotor constructions.

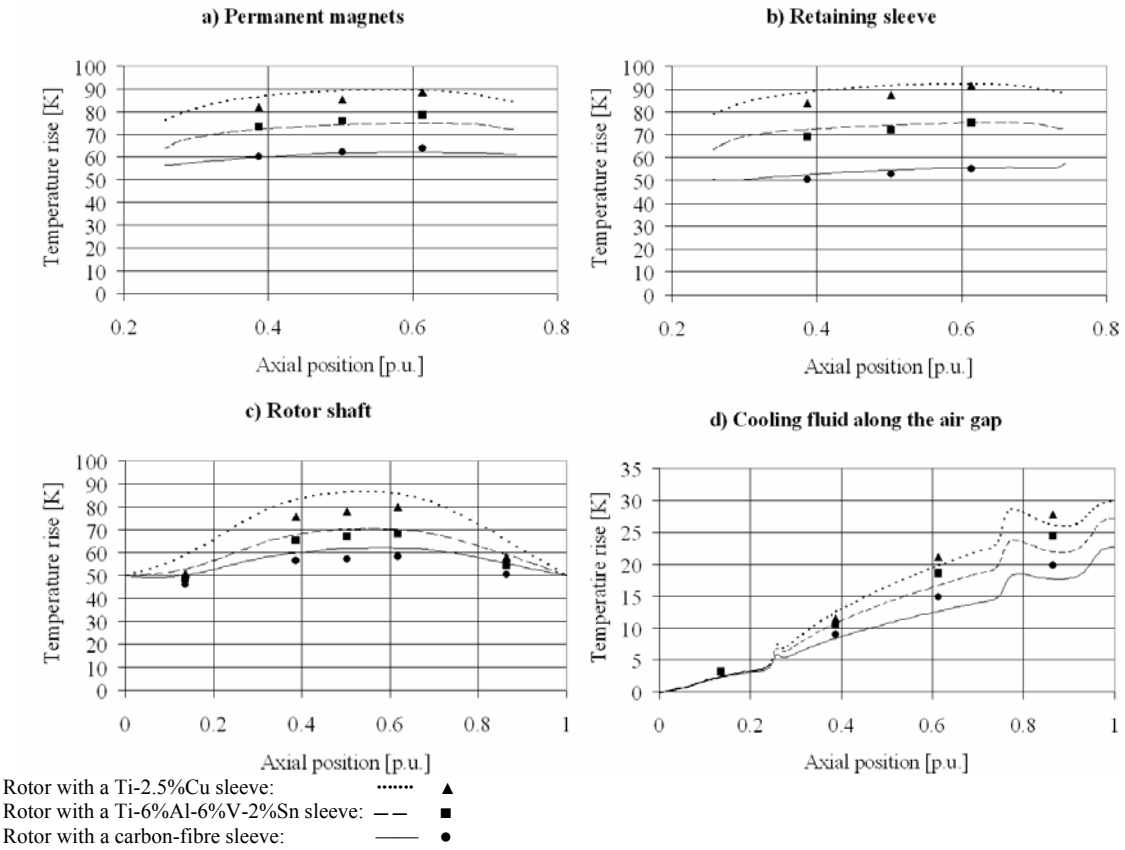

Figure 5.2: Results for the temperature rises ΔT [K] in different parts of the rotor predicted by the numerical-multiphysics method (lines) and the thermal-network method (markers).

5.2 Comparative rotordynamics analysis of the different rotor structures

A comparative rotordynamics analysis was performed for the same rotor structures. The constructions of the rotors are different only in the region of the electrical machine. The parameters of the other parts, such as the compressor and turbine wheels, the stiffness and damping of the bearings etc. are the same for each rotor construction. In this case, we can examine only the influence of the parts of the electrical machine on the rotordynamics properties of the different rotors. The bearings are assumed to be isotropic in all three cases. The outer diameters of the rotors in the part of the electrical machine are the same, only the inner dimensions are not the same, as was mentioned earlier in the comparative thermal analysis. The thickness of the sleeve and the mass of the permanent magnets can influence the rotordynamics properties of the rotor. If the thickness of the sleeve is reduced, the thickness of the solid-steel shaft can be increased by the same amount. The absence of an eddy-current shield in the constructions retained with the titanium alloys also leads to an increased thickness of the solid-steel shaft. A smaller amount of magnetic material results in a reduction in the mass of the rotor in that part of the electrical machine. If the titanium alloys are used for both retention and

shielding, they can increase the mass of the rotor since they have a much higher density than the carbon-fibre and aluminium materials. The use of an aluminium shield can reduce the mass of the rotor with a carbon-fibre sleeve, but it also reduces the stiffness because the aluminium has a lower Young's modulus than the titanium. All these variations in the dimensions and materials used can influence the rotordynamics properties of the rotor and without a comparative rotordynamics analysis of all the types of rotors we cannot conclude which rotor construction has the best behaviour. The changes in the design parameters of the rotors retained with the titanium-alloy sleeves compared to the rotor with a carbon-fibre sleeve are presented in Table 5.3. The first four critical speeds for the three rotor constructions under examination are calculated and the results are presented in Table 5.4.

Table 5.3: Changes in the design parameters of the rotors retained with titanium-alloy sleeves compared to the rotor with a carbon-fibre sleeve designed for the high-speed compressor.

Type of rotor according to the sleeve material	Thickness of the solid-steel shaft	Sleeve thickness	Mass of the permanent magnets
Ti-6%Al-6%V-2%Sn	+ 3.7 %	- 21 %	- 21 %
Ti-2.5%Cu	- 1.2 %	+ 58 %	+ 11 %

Table 5.4: Results for the forward and backward critical speeds n_c [rpm] for all rotor constructions.

Type of rotor according to the sleeve and shield	Dir.	First rigid	Second rigid	First flexural	Second flexural
Carbon fibre sleeve + Al shield	Fwd	6,073-6,106	10,200-10,343	35,833-36,249	76,107-81,287
	Bwd	6,067-6,100	9,822- 9,945	30,791-30,999	52,636-54,429
Titanium alloy Ti-6%Al-6%V-2%Sn	Fwd	6,033-6,066	10,129-10,225	35,944-36,293	77,860-82,197
	Bwd	6,028-6,061	9,759-9,843	30,749-30,938	53,217-54,685
Titanium alloy Ti-2.5%Cu	Fwd	6,036-6,082	10,191-10,336	35,727-36,179	75,298-80,976
	Bwd	6,030-6,077	9,813-9,938	30,665-30,914	52,209-54,223

The influence of the rotor type on the value of the critical speed in Table 5.4 is noticeable but it is not very strong since the electrical machine takes up only a small part of the whole rotor. More obvious results concerning the rotordynamics behaviour of the different types of rotors can be obtained if the electrical machine takes up a larger part of the whole rotor length. For this purpose, an experimental solid-steel rotor shaft (Figure 5.3) with a relatively short length was used and three different types of high-speed PM electrical machines were designed. As in the previous case of the rotor for a high-speed compressor, the same types of retaining sleeve materials were used. The three PM rotors are designed for a rated speed n_r=36,000 rpm, power P_r=100 kW, voltage U_r=400 V and displacement factor $cos\ \varphi$=0.98. Table 5.5 shows the changes in the design parameters of the rotors with titanium alloys in comparison to the dimensions

of the rotor with a carbon-fibre sleeve. The beam-like model of the rotor shaft with a designed high-speed PM rotor structure is presented in Figure 5.4. The dimensions of the model are presented in the same figure. During the analysis, one rigid conical mode and two flexural modes were determined and their shapes are presented in Figure 5.5. The cylindrical rigid-body mode was not determined in the analysis. The results for the critical speeds for all rotor structures are presented and compared in Table 5.6.

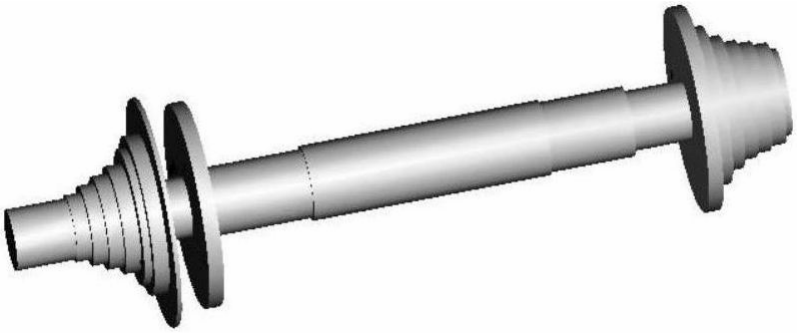

Figure 5.3: Geometry of the experimental solid-steel rotor shaft.

Table 5.5: Changes in the design parameters of the rotors retained with titanium-alloy sleeves compared to the rotor with a carbon-fibre sleeve designed for the experimental solid-steel rotor shaft.

Type of rotor according to the sleeve material	Thickness of the solid-steel shaft	Sleeve thickness	Mass of the permanent magnets
Ti-6%Al-6%V-2%Sn	+ 5.3 %	- 24 %	- 22 %
Ti-2.5%Cu	+ 1.6 %	+ 32.4 %	- 7.4 %

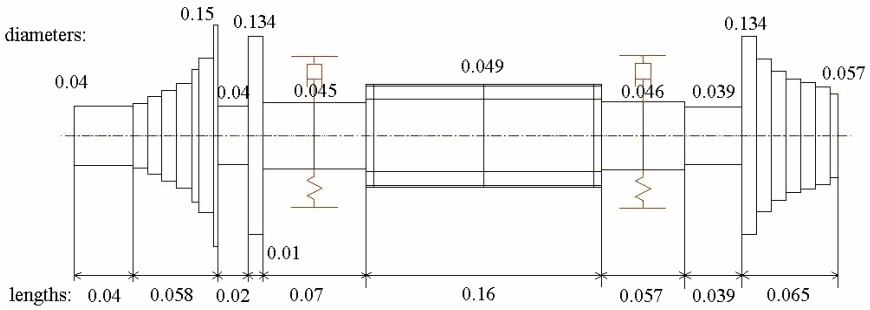

Figure 5.4: Beam-like model of the experimental solid-steel rotor shaft with a designed high-speed PM rotor structure and dimensions [m] of the geometry.

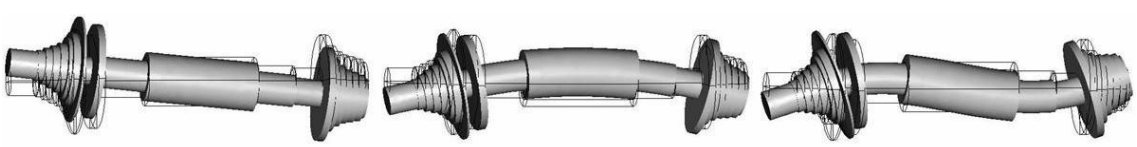

a) Conical mode b) First flexural mode c) Second flexural mode

Figure 5.5: Shapes for the first three critical modes of the experimental solid-steel rotor shaft with a designed high-speed PM rotor structure.

Table 5.6: Results for the forward and backward critical speeds n_c [rpm] for all constructions of the experimental solid steel rotor shaft.

Type of rotor according to the retaining sleeve	Dir.	Conical rigid	First flexural	Second flexural
Carbon fibre sleeve + Al shield	Fwd	20,107-20,587	59,549-66,235	129,730-140,050
	Bwd	19,339-19,751	44,530-47,576	72,686-75,907
Titanium alloy Ti-6%Al-6%V-2%Sn	Fwd	20,532-20,919	61,220-67,910	135,180-144,530
	Bwd	19,718-20,055	46,001-49,120	76,229-79,217
Titanium alloy Ti-2.5%Cu	Fwd	20,237-20,699	59,401-66,454	130,530-140,980
	Bwd	19,443-19,847	44,734-47,980	73,540-76,864

6 Maximum powers of high-speed PM electrical machines for compressor applications

Modern frequency converters can supply electrical machines with quite high powers and frequencies that can cause the thermal and mechanical limitations of the machines to be exceeded. In fact, the frequency converter does not restrict the power and the speed of a high-speed drive. A high-speed PM electrical machine usually operates close to the critical point of its thermal and mechanical constraints and these constraints place a limitation on the maximum power of the machine. The determination of the maximum power limits of high-speed PM electrical machines is a challenge because if a complete design of a high-speed drive for a real industrial application is done, then all the thermal and mechanical constraints should be implemented simultaneously. The electromagnetic constraints are usually correlated with the thermal and mechanical ones and they are not very different from the electromagnetic constraints that apply in conventional machines.

There are many references in the literature that deal with the design and the analysis of high-speed PM electrical machines. The data about the rated speed and power operation points of the machines that are analysed in the literature in the high-speed region up to n=120,000 rpm are presented in Table 6.1 and also graphically in Figure 6.1. These data were found in the scientific papers described in Chapter 2 and also on the web pages of some producers of high-speed PM machines such as Satcon®, Synchrony® and Mohawk Innovative Technology®. The data are divided into high-speed applications that are referred to simulations, laboratory test machines, and real high-speed applications in industry. As we can see, the simulations and the laboratory test machines have somewhat higher values for their power than the real industrial applications. The reason is that most of the simulated machine designs include an electromagnetic analysis without any consideration of the thermal or the mechanical constraints. The laboratory test machines are mostly used for the experimental testing of the electrical part of the high-speed drive and, in the references that are presented, only some of the thermal and mechanical design constraints are considered, but not all of them. We can suppose that only the high-speed industrial applications are designed in order to fulfil all the electrical, thermal, and mechanical constraints. However, we do not know how many of the industrial applications presented in Figure 6.1 are intentionally designed to operate at power levels that are close to the possible maximum power limit.

In order to find out the maximum power limits of high-speed PM machines intended for compressor applications, five machines for speeds of 20,000 rpm, 40,000 rpm, 60,000 rpm, 80,000 rpm, and 100,000 rpm are designed with a maximum power that is limited by the thermal and mechanical constraints. In each machine, one compressor wheel is attached to the same shaft and the whole rotor is supported on two radial and one axial active magnetic bearings. A simultaneous electrical, thermal, and mechanical analysis is performed during the design process fulfilling all the types of constraints. The constraints that limit the power of the five machines designed are listed in Table 6.2. They are divided into constraints for the high-speed PM electrical machine and constraints for the mechanical parts.

Table 6.1: Published speed-power data for high-speed PM electrical machines in various references.

Simulations			Laboratory test machines			Industrial applications		
Reference	n_r [rpm]	P_r [kW]	Reference	n_r [rpm]	P_r [kW]	Reference	n_r [rpm]	P_r [kW]
Paulides et al. (2004)	20,000	1,500	Hippner et al. (1992)	30,000	10	Rahman et al. (2004)	15,000	1,000
Arkkio et al. (2005)	30,000	540	Publication P1	31,500	130	Ofringa et al. (1996)	18,000	1,400
Wang et al. (2008)	40,000	40	Schneider et al. (2005)	40,000	40	Bianchi et al. (2004)	20,000	1.3
Jang et al. (2003)	40,000	1	Diop et al. (1998)	45,000	70	Synchrony®	20,000	400
Jang et al. (2004)	40,000	5	Mekhiche et al. (1999)	47,000	20	Boglietti at al. (1991)	25,000	20
Arkkio et al. (2005)	60,000	95	Rahman et al. (2004)	60,000	200	Canders (1998)	30,000	450
Jiqiang et al. (2005)	60,000	100	Wang et al. (2008)	60,000	75	Mellor et al. (2005)	36,000	20
Arkkio et al. (2005)	100,000	30	Castagnini et al. (2002)	69,000	155	Agahi et al. (1996)	45,000	75
			Jang et al. (2005)	70,000	50	Rahman et al. (2004)	45,000	70
			Aglén et al. (2003)	70,000	110	Satcon®	50,000	20
			Ede at al. (2002)	120,000	1.25	Synchrony®	60,000	100
						Rahman et al. (2004)	100,000	2.6
						Mohawk Inn. Technology®	120,000	12

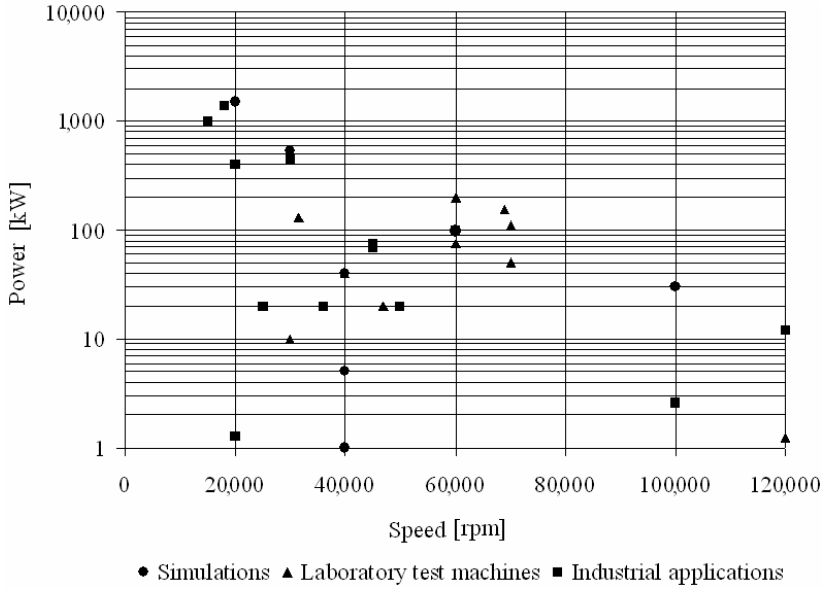

Figure 6.1: Published speed-power data for high-speed PM electrical machines.

Table 6.2: Design constraints for the high-speed PM electrical machine and the mechanical parts.

Constraints for the electrical machine	
Surface rotor speed	v_s=200 m/s.
Retaining material	Carbon-fibre sleeve, maximum stress σ_{max}=800 MPa.
Type of eddy-current shield	Aluminium screen.
Number of poles	$2p_p$=4.
Displacement factor	$cos\ \varphi$=0.98.
Type of permanent magnets	Nd-Fe-B, B_r=1.16 T, H_c=1900 kA/m at 20^0C.
Maximum temperatures of the permanent magnets and the carbon-fibre sleeve	$T_{max\ pm}$=$T_{max\ cfs}$=130 ^{0}C (or maximum temperature rise ΔT_{max}=90 K if the ambient temperature is T_{amb}=40 ^{0}C).
Maximum temperature of the stator winding	T_{max}=165 ^{0}C (or temperature rise ΔT_{max}=125 K if the ambient temperature is T_{amb}=40 ^{0}C) – defined by the class of insulation H.
Cooling	Air flow in a cooling duct in the stator and the air gap, an impingement flow on the upper side of the end-winding and water jacket on the outer stator surface. The air flow should provide average coefficients of convection of h_{avg}=250-300 W/(m^2·K) in the air gap and in the end winding region.
Constraints for the mechanical parts	
Type of application	Compressor.
Number of compressor wheels	One compressor wheel on the rotor shaft.
First flexural critical speed	10% higher than the rated operational speed (subcritical operation).
Bearings	Active magnetic bearing with stiffness k = 2·10^6 N/m

The five high-speed PM machines that are designed have the same basic construction, only their dimensions are different since they are dependent on the power and speed. The basic construction of the rotor is the same one as presented in Figure 1.1. The design procedure is exactly equal for all five cases and only the results for the machine with a rated speed n_r=60,000 rpm will be presented here. The electromagnetic and mechanical losses are the input parameters for the thermal part of the design of the machines. The results for all types of losses generated in the machine with a rated speed n_r=60,000 rpm are presented in Table 6.3.

Table 6.3: Results of all types of losses in the electrical machine with a rated speed n_r=60,000 rpm.

Types of losses		Power (W)
Electromagnetic losses	Resistive losses in the permanent magnets	23
	Resistive losses in the aluminium screen	358
	Resistive losses in the stator winding	1784
	Core losses in the stator yoke	437
	Core losses in the stator teeth	429
Mechanical losses from the airflow	Air-friction losses	434
	Losses resulting from the pressure for blowing the air and rotat. acceleration of the air in the air gap	464

The same methods that were described in Chapter 3 are implemented for the determination of the maximum powers of the electrical machines. A result of the fluid flow that is obtained from the 2D multiphysics method is presented in Figure 6.2.a. The first part of the fluid flows through a radial cooling duct in the middle of the stator core and after that in the air gap. The second part of the flow is an impingement jet that serves for direct cooling of the end-winding. The temperature rise distribution of the fluid is presented in Figure 6.2.b. The highest temperature rise of the air is on the outlet side of the machine.

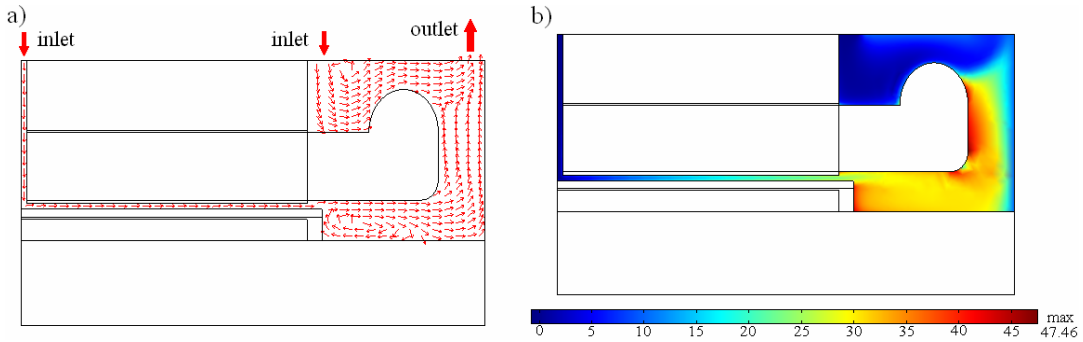

Figure 6.2: Results of the CFD modelling of the high-speed PM machine for speed n=60,000 rpm: a) fluid flow, b) temperature rise of the fluid ΔT (K).

The distribution of the temperature rise in the rotor that is determined by the 3D heat-transfer method is presented in Figure 6.3. During the design process, as required according to the thermal constraints of the rotor, the power of the machine is increased until the maximum temperature rise of $\Delta T_{\max\ rot}$≈90 K of the rotor is achieved. The distribution of the temperature rise in the stator, which is determined by the 3D heat-transfer method, is given in Figure 6.4. We can notice that the hot spot is located in the end-winding. The power of the machine is increased until a maximum temperature rise of $\Delta T_{\max\ sw}$≈114.5 K of the stator winding is achieved. This value is about 8.2% lower than the critical temperature rise for the class of insulation H because, according to the measured results presented in Publication P7, the method underestimates the temperature rise of the winding, so that the maximum deviation between the simulated and measured results for the determination of the stator winding temperatures was -8.2%. The main reason for this is that the losses that are generated by the circulation currents flowing in the parallel paths of the filamentary stator winding are not taken into account. The mechanical design of each machine is performed simultaneously with the thermal and electromagnetic designs. The first mechanical constraint is that the permitted stress of the carbon-fibre sleeve should be $\sigma_{\max}$=800 MPa. According to the second mechanical constraint, which is from the rotordynamics point of view, the maximum power of the machine is obtained when the dimensions of the electrical machine, the compressor wheel, and active magnetic bearings are changed in order to obtain the first flexural critical speed as being 10% higher than the rated speed of the machine. For example, for the machine designed for a rated speed n_r=60,000 rpm, the designed power will reach its limit when the first flexural critical speed is approaching the value n_c≈66,000 rpm. The shape of the flexural mode for this critical speed is shown in Figure 6.5.

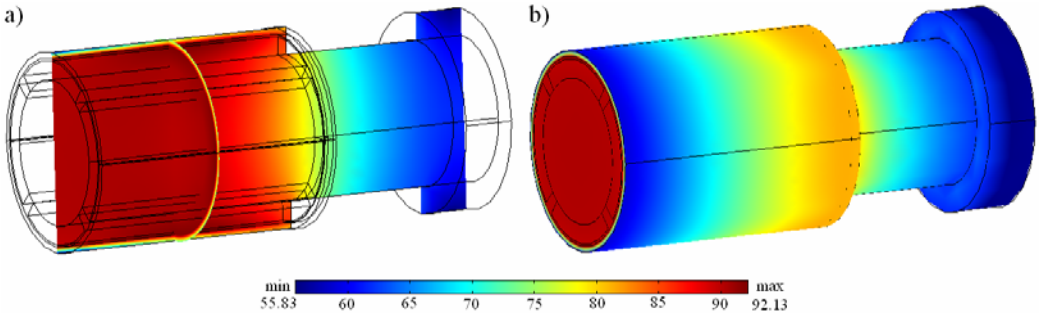

Figure 6.3: Temperature rise ΔT (K) of the rotor: a) inner geometry, b) outer surface.

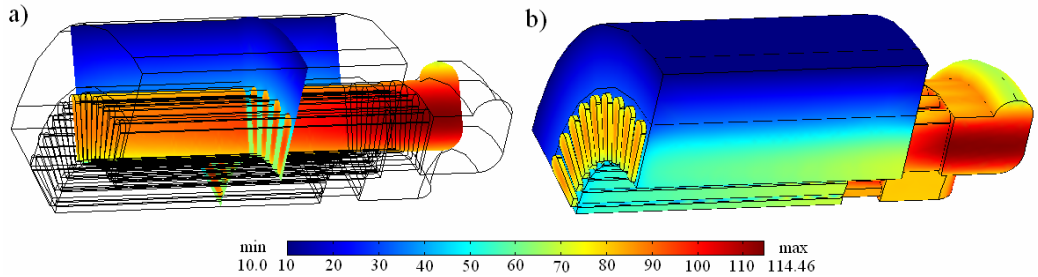

Figure 6.4: Temperature rise ΔT (K) of the stator: a) inner geometry, b) outer surface.

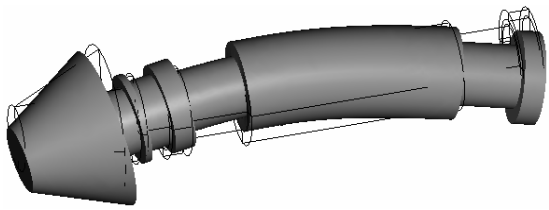

Figure 6.5. Rotor flexural mode for the first critical speed n_c=66,000 rpm of the machine for a rated speed n_r=60,000 rpm.

The electromagnetic, thermal, and mechanical designs described previously are performed simultaneously for each machine until the maximum power is achieved, when all constraints are fulfilled at their critical values. The estimated maximum powers for each machine are presented in Table 6.4. The same results of the maximum powers for high-speed PM machines for compressor applications in the range 20,000-100,000 rpm that are presented in Table 6.4 are also presented in Figure 6.6. They are compared with the speed-power values of the real industrial applications. The estimated values of the maximum powers that are presented establish a curve that shows the theoretical limit of the performance of high-speed compressor applications.

Table 6.4: Estimated maximum powers of the high-speed PM machines for compressor applications.

Machine No.	Speed (rpm)	Maximum power (kW)
1	20,000	1,500
2	40,000	425
3	60,000	181
4	80,000	93
5	100,000	55

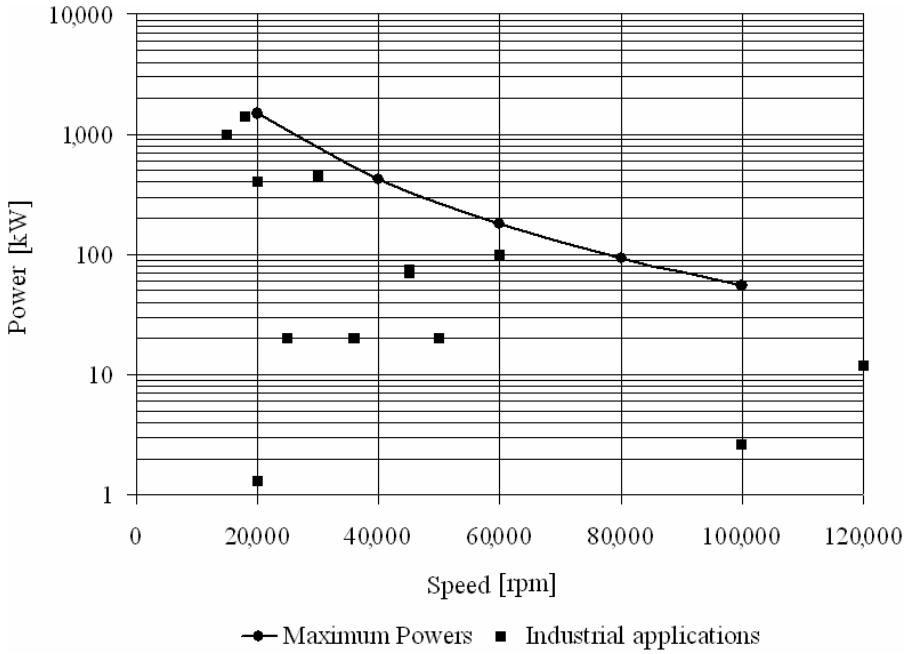

Figure 6.6. Estimated maximum powers for high-speed PM machines for compressor applications compared with the powers of the real industrial applications.

7 Discussion

7.1 Methods for thermal analysis

The distribution of the temperature rise in the machine and the properties of the cooling flow are estimated using the numerical-multiphysics method and the traditional thermal-network method. The comparison of the results for the temperature rises in all parts of the electrical machine is presented in Figure 4.12 and the comparison shows a good agreement between the results. Better agreement between the results is achieved for the estimated temperature rises in the rotor parts. The main advantage of the numerical-multiphysics method is that it gives a more realistic and detailed representation of the thermal and turbulent phenomena in the machine. The small deviations among the results for the temperature distributions are because the two methods that were implemented have completely different natures and because of the vagueness in the determination of the coefficients of thermal convection. Table 4.3 shows that there are certain discrepancies in the results of the coefficients of thermal convection that are obtained from the numerical-multiphysics method and the semi-empirical equations. The discrepancies in the results are mostly higher in the stator region since it has a more complex geometry than the rotor. The advantage of the numerical-multiphysics method lies in the fact that CFD, which is a part of the method, can model the coolant flow in more complex geometries and it can calculate the local values of the coefficient of convection, including their separate determination in the inlet and outlet parts of the machine. The methods being used today for accurate CFD modelling are still under development and being improved, so even more sophisticated and accurate models can be expected in the future.

7.2 Methods for mechanical analysis

The mechanical design of a high-speed electrical machine is a demanding task because, during high-speed performance, the retaining sleeve on the rotor is loaded with a stress that is quite close to the critical value and the machine is often designed to operate at a speed that is close to one of the flexural critical speeds. The rotordynamics analysis in this thesis is based on the FEM and the rotors under examination are modelled using beam-like and 3D FE models. These models are used for the determination of the shapes of the flexural modes and the values of the critical speeds. As we can see from Tables 4.4, 5.4, and 5.6, the highest values for the critical speeds are obtained in those cases when the rotor elements (permanent magnets, Al-shield, and sleeve) contribute fully to the stiffness. This desired case is very difficult to achieve in practice since the degree of contribution to the stiffness of the rotor shaft depends on many factors, such as the quality of the manufacturing, shrink-fitting of the rotor elements, rotation speed, temperature, etc. The real value of the critical speed should be expected to be within a range of critical speeds in which the lowest value is for a case in which the rotor

elements do not contribute to the rotor stiffness and the highest value is for a case in which they contribute fully to the rotor stiffness.

7.3 Comparative analysis of different rotor structures according to the retaining sleeve

The results from Figures 5.1 and 5.2 show that the rotor with a carbon-fibre sleeve and an aluminium shield has the lowest temperature rise. This is mainly due to the lowest eddy-current loss generation. The disadvantages of the carbon-fibre material are its very low thermal conductivity, which makes the cooling of the magnets more difficult, and its very low electrical conductivity, which does not provide a shielding effect from eddy-current loss generation in the magnets. The only way to protect the magnets from high temperatures in this case is to reduce the eddy-current loss generation in the rotor by using either an aluminium or copper shield. The rotor construction retained with a Ti-6%Al-6%V-2%Sn titanium-alloy sleeve and without any additional eddy-current shield has higher temperature rises than the rotor with a carbon-fibre sleeve because of the higher eddy-current loss generation. This titanium alloy is a better thermal conductor than the carbon-fibre material. The results obtained with the numerical-multiphysics method and the thermal-network method show that the temperature rise of the magnets is about 75 K. This temperature rise is still in the safe operating area, since for an ambient temperature of T_{amb}=40 ^{0}C, the temperatures of the magnets will be below their critical thermal limit $T_{max\ pm}$=130 ^{0}C. The thermal analysis shows that the thermal constraints are fulfilled and this type of rotor can be an interesting solution for high-speed applications. The rotor with a Ti-2.5%Cu titanium alloy sleeve and without any additional eddy-current shield has the highest temperature rises, which can exceed a value of 90 K. This means that for an ambient temperature of T_{amb}=40 ^{0}C, the total temperature of the magnets will approach the safe limit. The use of this material in high-speed applications is not justified, at least from the thermal point of view.

The rotordynamics analysis shows that the rotor constructions retained with the Ti-6%Al-6%V-2%Sn titanium-alloy sleeve show an advantage over the other rotor constructions since they have the highest first flexural critical speed and this advantage is even more apparent for the second flexural critical speed. The main reasons for this are the grater thickness of the solid-steel shaft and the lower mass of the rotor components. The rotor constructions retained with the Ti-2.5%Cu titanium-alloy sleeve have the lowest critical speeds values since in this construction the solid-steel shaft is less thick and the mass of the rotor parts is increased. If the electrical machine takes up a significant part of the total rotor length, the type of construction significantly influences the rotordynamics behaviour. In this case, it is more obvious that the experimental rotor shaft with the construction retained with the Ti-6%Al-6%V-2%Sn titanium-alloy sleeve shows much higher first and second flexural critical speeds and this emphasises its advantage over the rotor constructions retained with the other types of retaining sleeves.

7.4 Maximum power limits of high-speed PM electrical machines

The estimated values of the maximum powers of high-speed PM electrical machines for compressor applications are obtained when all the critical values of the thermal and mechanical constraints are considered at the same time and they establish the theoretical limit of the performance of the high-speed compressor applications. The power-speed data for high-speed PM electrical machines for compressor applications and other types of high-speed applications belong to the maximum-power region defined by the curve in Figure 6.6. The same figure shows that some high-speed industrial applications in the lower speed region have a power that is very close to the maximum power limit. We can also notice that in the region of higher speeds, the high-speed applications have powers that are somewhat lower than the maximum. This means that the future design of high-speed PM industrial applications with higher powers in the region of very high speeds can be a real challenge.

The power limits that were determined are valid only for the type of basic design that is reported in Chapter 6 and the constraints that are listed in Table 6.2. The basic design and the listed constraints are the most typical ones found in the literature that deals with the analysis and design of high-speed PM electrical machines. Certain changes in the basic design and an implementation of different standards for the constraints may automatically change the upper limit of the maximum powers. The power limit of the drives will be directly affected in those cases where use is made of different stator and rotor constructions, other types of bearings, more compressor stages, etc. For each specific type of basic design there will be a curve of maximum powers that is unique only for that design.

7.5 Significance of the research

This thesis contributes to several issues related to the thermal and mechanical analyses of high-speed PM electrical machines. A new approach to the thermal analysis of this type of machine is presented. Using this thermal approach in conjunction with a rotordynamics analysis, several important design issues related to high-speed PM machines are solved. The literature research shows that there is a lack of publications dealing with the coupled heat-transfer and CFD analyses of the whole domain of an electrical machine. For example, many authors perform a FE thermal analysis of the machine with a separate empirical estimation of the convection. On the other hand, there are authors who perform a CFD analysis with an assumption of constant surface temperatures at the boundaries of the solid parts of the machine. The methods for uncoupled, separated analyses of the solid and fluid domains of the machine can be fast and accurate enough, but there is still potential for them to be improved. A coupled analysis of both domains gain in importance in producing a more realistic thermal model of the whole machine domain, enabling a better view to be gained of the heat flux resulting from convection and conduction. This is especially beneficial for the thermal analysis of high-speed machines because the considerable differences in both the temperature rises of the cooling fluid and the local coefficients of convection

between the inlet and outlet regions contribute to a much greater temperature rise in the outlet part of the machine. If either a constant surface temperature in a single CFD model or an average convection on a surface in a single heat-transfer model of a high-speed machine is assumed, there is a risk of underestimating the temperatures in the outlet part of the machine. The coupled heat-transfer and CFD analysis performed in this thesis considers the interactions of all these thermal and turbulent phenomena in the machine at the same time. The numerical-multiphysics method proposed here gives a simultaneous estimation of the temperature rises in the solid and fluid domains of the whole electrical machine and, at the same time, it gives an estimation of the turbulent properties of the coolant. A major advantage of the method is that it is fast and requires low computational resources. The method also estimates the local coefficients of thermal convection on each surface between the solid and fluid domains, with a particular consideration of the inlet and outlet parts of the machine. The existing literature offers a semi-empirical estimation of the average coefficients of convection on each surface or a numerical CFD estimation of the local coefficients of convection, mostly in the air-gap and end-winding regions, which presupposes prescribed values of the temperatures of the solid boundaries. The traditional thermal-network method, which is widely used in the literature, is also used in the thesis. It is mostly used for a comparison of its results with the results obtained with the numerical-multiphysics method and for the determination of the critical thermal operation for high-speed PM machines. This kind of critical thermal operation, which includes an estimation of the temperatures of the most thermally sensitive parts of the machine as functions of the value of the fluid flow in the air gap and the type of eddy-current shield used, has not been reported in the literature.

The comparative thermal and mechanical analysis of different rotor structures according to the type of retaining sleeve used is not very widely covered in the literature. The analyses are usually performed only by means of an examination of the thermal properties of different rotors equipped with different types of sleeves, without any consideration of the mechanical implications, or vice versa. In this thesis, the comparative analysis of different rotor structures is carried out with respect to detailed thermal and rotordynamics analyses performed at the same time for each structure under examination. Additionally, the thermal and rotordynamics properties of the structures retained with titanium alloys were reported. This type of rotor structure is not widely reported in the literature.

The methods used for thermal and mechanical analysis in this thesis are used for the estimation of the maximum powers of high-speed PM electrical machines. In fact, the maximum power limits of high-speed PM machines have not been deeply investigated in the current literature. Some authors have made attempts to find out the power limitations of different types of high-speed machines, but their results were based on collections of speed-power data of machines from other references. There is a lack of publications in which the influence of the thermal and mechanical constraints on the power limitations of the machines is reported. In this thesis, the maximum power limits were estimated by a simultaneous consideration of the critical values of all the important thermal and mechanical constraints.

8 Summary

Within the thesis, methods for the thermal and mechanical analysis of high-speed PM electrical machines have been presented and implemented. A high-speed electrical machine always operates very close to its thermal and mechanical limits and that is why reliable methods for accurate thermal and mechanical analysis should be developed. A combined 2D-3D numerical method for the thermal analysis of an electrical machine is presented. The thermal properties of the flow, such as the coefficients of thermal convection and temperature rise of the flow, were estimated using a 2D multiphysics method. The precise distribution of the temperature rise in the whole solid domain of the machine was determined using a 3D numerical heat-transfer method. The results for the temperature rises in the machine from the numerical method are compared with the results obtained by the traditional thermal-network method, which uses a totally different approach to the heat-transfer analysis. The numerical-multiphysics method presented here is a novel compromise between 2D axi-symmetric multiphysics rough modelling and the 3D thermal fine modelling, a compromise that allows an accurate estimation of the local temperature rises in the electrical machine with a minimum amount of computational resources. The main goals of the mechanical analysis are to determine the rotordynamics behaviour of the rotor and also to calculate the stress that occurs in the retaining sleeve during the high-speed operation. The rotordynamics models are used for the determination of the values of the critical speeds and the shapes of the rigid and flexural modes. The stress in the retaining sleeve is determined using simple analytical equations and the rotordynamics analysis is based on the FE modelling of high-speed PM rotors using beam-like models and 3D models.

Extended thermal and mechanical analyses of three different rotor constructions of a high-speed PM electrical machine are performed. The first type of rotor construction is retained with a carbon-fibre sleeve and uses an aluminium shield for eddy currents. The second rotor construction is retained with a retaining sleeve made from the titanium alloy Ti-6%Al-6%V-2%Sn and the sleeve on the third rotor is made from the titanium alloy Ti-2.5%Cu. These two rotor constructions that have titanium-alloy sleeves do not have separate eddy-current shields. The temperature rises of the rotors are estimated using the numerical-multiphysics method and also with the thermal-network method. The rotor with a carbon-fibre sleeve and an aluminium shield has the lowest temperature rises in comparison with the other rotors because it generates the lowest amount of eddy-current losses. The rotor with a retaining sleeve made of the titanium alloy Ti-6%Al-6%V-2%Sn offers promising thermal properties because the temperature of the magnets is still below the critical value, although this construction does not contain any additional eddy-current shield. According to the rotordynamics analysis, the rotor with a Ti-6%Al-6%V-2%Sn titanium alloy sleeve provides the best rotordynamics properties when compared to the other rotor constructions. The main reason for this is that the thinner retaining sleeve and the absence of an eddy-current shield in this construction enable a thicker solid-steel shaft to be used and the rotor parts have a lower total mass. In a case when the electrical machine takes up a significant part of the total rotor length, the use of a rotor structure retained with the titanium alloy Ti-6%Al-6%V-2%Sn can significantly improve the rotordynamics properties of the rotor. The rotor

construction with a retaining sleeve made of the titanium alloy Ti-2.5%Cu is inferior from the thermal and mechanical points of view when compared with the previous rotor constructions.

At the end of the thesis, the maximum power limits for high-speed PM electrical machines for air-compressor applications are determined. Five high-speed PM electrical machines for the speeds 20,000 rpm, 40,000 rpm, 60,000 rpm, 80,000 rpm, and 100,000 rpm are designed in order to determine their maximum mechanical powers. For this purpose, the electromagnetic, thermal, and mechanical designs of each machine are performed simultaneously. In fact, in order to obtain the maximum powers of the high-speed machines, the critical values of the thermal and mechanical constraints should be considered in the design. The estimated maximum power limit defines the speed-power region of safe operation of high-speed PM electrical machines intended for compressor applications. The future design of high-speed PM electrical machines with higher powers than those of the existing industrial applications can be a real challenge especially in the region of very high speeds.

References

Agahi, R.R., Schröder, U. 1996. Industrial high speed turbogenerator system for energy recovery. *Proceedings of the 5th International Symposium on Magnetic Bearings*, August 1996, pp. 381-387.

Aglén, O., Andersson, Å. 2003. Thermal analysis of a high-speed generator. *Proceedings of the 38th IAS annual meeting*, Vol.1, 12-16 October 2003, pp. 547-554.

Antipov, V.N., Danilevich, Ya.B. 2007. High-speed electrical machines for power engineering: current state and development trends. *Russian Electrical Engineering*, Vol. 78, No.6, June 2007, pp. 277-279.

Arkkio, A. 1987. Analysis of induction motors based on the numerical solution of the magnetic field and circuit equations. *Acta Polytechnica Scandinavica, Electrical Engineering Series*, No. 59, Helsinki, 97 p. (Doctoral thesis)
Available at: http://lib.tkk.fi/Diss/198X/isbn951226076X/isbn951226076X.pdf

Arkkio, A., Jokinen, T., Lantto, E., 2005. Induction and permanent-magnet synchronous machines for high-speed applications. *Proceedings of the 8th International Conference on Electrical Machines and Systems - ICEMS 2005*, Vol. 2, 27-29 September 2005, pp. 871-876.

Bailey, C., Saban, D.M., Pinto, P.G. 2009. Design of high-speed direct-connected permanent-magnet motors and generators for the petrochemical industry. *IEEE Transactions on Industry Applications*, Vol. 45, No. 3, May/June 2009, pp. 1159-1165.

Bianchi, N., Bolognani, S., Luise, F. 2004. Potentials and limits of high-speed PM motors. *IEEE Transactions on Industry Applications*, Vol. 40, No. 6, November/December 2004, pp. 1570-1578.

Binder, A., Klohr, M. Schneider, T. 2004. Losses in high-speed permanent magnet motor with magnetic levitation for 40000/min, 40 kW. *Proceedings of the International Conference in Electrical Machines – ICEM'04*, on CD, September 2004, 6 p.

Binder, A., Schneider, T., Klohr, M. 2006. Fixation of buried and surface-mounted magnets in high-speed permanent-magnet synchronous machines. *IEEE Transactions on Industry Applications*, Vol. 42, No. 4, July/August 2006, pp. 1031-1037.

Binder, A., Schneider, T. 2007. High-speed inverter-fed AC drives. *Proceedings of the International Aegean Conference on Electrical Machines and Power Electronics - ACEMP'07*, 10-12 September 2007, pp. 9-16.

Boglietti, A., Pastorelli, M., Profumo, F. 1991. High speed brushless motors for spindle drives applications. *Proceedings of SM'100*, 27-29 August 1991, pp. 817-822.

Boglietti, A., Cavagnino, A., Lazzari, M., Pastorelli, M. 2003. A simplified thermal model for variable-speed self-cooled industrial induction motor. *IEEE Transactions on Industry Applications,* Vol. 39, No. 4, July/August 2003, pp. 945-952.

Boglietti, A., Cavagnino, A. 2007. Analysis of the endwinding cooling effects in TEFC induction motors. *IEEE Transactions on Industry Applications,* Vol. 43, No. 5, September/October 2007, pp. 1214-1222.

Boglietti, A., Cavagnino, A., Staton, D. 2008. Determination of critical parameters in electrical machine thermal models. *IEEE Transactions on Industry Applications,* Vol. 44, No. 4, July/August 2008, pp. 1150-1159.

Boglietti, A., Cavagnino, A., Staton, D., Shanel, M., Mueller, M., Mejuto, C. 2009a. Evolution and modern approaches for thermal analysis of electrical machines. *IEEE Transactions on Industrial Electronics,* Vol. 56, No. 3, March 2009, pp. 871-882.

Boglietti, A., Cavagnino, A., Staton, D. A., Popescu, M., Cossar, C., McGilp, M. I. 2009b. End space heat transfer coefficient determination for different induction motor enclosure types. *IEEE Transactions on Industry Applications,* Vol. 45, No. 3, May/June 2009, pp. 929-937.

Canders, W.R. 1998. High speed machines on magnetic bearings – design concepts and power limits. *Proceedings of International Conference in Electrical Machines – ICEM'98*, Vol. 1, 2-4 September 1998, pp. 20-25.

Castagnini, A., Garavaglia, M., Moriconi, F., Secondo, G. 2002. Development of a very high speed and power synchronous PM motor. *International Conference in Electrical Machines – ICEM'02*, on CD, 25-28 August 2002, 6 p.

Castagnini, A., Leone, I. 2002. Test results of a very high-speed PM brushless motor. *Proceedings of the International Conference in Electrical Machines – ICEM'02*, on CD, 25-28 August 2002, 6 p.

Chen, W.J., Gunter, E.J. 2005. Introduction to dynamics of rotor-bearings systems. *Trafford Publishing*, Victoria, BC, Canada, 448 p.

Chin, Y.K., Nordlund, E., Staton, D.A. 2003. Thermal analysis - lumped circuit model and finite element analysis, *Proceedings of the 6th International Power Engineering Conference IPEC'03*, 27-29 November, 2003, pp. 952-957.

Cho, H.W., Jang, S.M., Choi, S.K. 2006. A design approach to reduce rotor losses in high-speed permanent magnet machine for turbo-compressor. *IEEE Transactions on Magnetics*, Vol. 42, No. 10, October 2006, pp. 3521-3523.

Comsol Multiphysics®. 2006. Heat transfer module, user's guide, version 3.3.

Diop, A., Schröder, U. 1998. Experimental losses determination of high speed synchronous machines 70 kW – 45 000 rpm with magnetic bearings. *Proceedings of International Conference in Electrical Machines – ICEM'98*, Vol. 3, 2-4 September 1998, pp. 2106-2110.

Ede, J.D., Zhu, Z.Q., Howe, D. 2002. Rotor resonances of high-speed permanent-magnet brushless machines. *IEEE Transactions on Industry Applications*, Vol. 38, No. 6, November/December 2002, pp. 1542-1548.

Genta, G. 2005. Dynamics of rotating systems, *Springer*, New York, 658 p.

Gutzwiller, L., Corbo, M.A. 2003. Vibration and stability of 3000-hp, titanium chemical process blower, *International Journal of Rotating Machinery*, Vol. 9, No. 2, 2003, pp. 197-217.

Hippner, M., Harley, R.G. 1992. High speed synchronous machine with rare earth-cobalt magnets. *Proceedings of the International Conference in Electrical Machines – ICEM'92*, Vol. 2, 15-17 September 1992, pp. 771-775.

Huai, Y., Melnik, R.V.N., Thogersen, P.B., 2003. Computational analysis of temperature rise phenomena in electric induction motors. *Applied Thermal Engineering*, Vol. 23, No. 7, May 2003. pp. 779-795.

Incropera, F.P., DeWitt, D.P. 1990. Fundamentals of heat and mass transfer, 3rd edn., *J. Wiley & Sons*, New York, 919 p.

Jang, S.M., Lee, S.H., Cho, H.W., Cho, S.K. 2003. Analysis of unbalanced force for high-speed slotless permanent magnet machine with Halbach array. *IEEE Transactions on Magnetics*, Vol. 39, No. 5, September 2003, pp. 3265-3267.

Jang, S.M., Cho, H.W., Lee, S.H., Yang, H.S., Jeong, Y.H. 2004. The influence of magnetization pattern on the rotor losses of permanent magnet high-speed machines. *IEEE Transactions on Magnetics*, Vol. 40, No. 4, July 2004, pp. 2062-2064.

Jang, S.M., Cho, H.W., Choi, J.Y., Park, J.H., Choi, S.K. 2005. Development of high-speed brushless DC motor for turbo-compressor, *Proceedings of the 8th International Conference on Electrical Machines and Systems - ICEMS 2005*, Vol. 2, 27-29 September 2005, pp. 877-882.

Jiqiang, W., Fengxiang, W., Tao, Y. 2005. Analysis of rotor losses for a high speed PM generator. *Proceedings of the 8th International Conference on Electrical Machines and Systems - ICEMS 2005*, Vol.2, 27-29 September 2005, pp. 889-892.

Jokinen, T., Saari, J. 1997. Modelling of the coolant flow with heat flow controlled temperature sources in the thermal networks. *IEE Proceedings*, Vol.144, No.5, September 1997, pp. 338-342.

Jokinen, T., Larjola, J., Mikhaltsev, I. 1998. Power unit for research submersible. *Proceedings of the International Conference on Electric Ship*, 1 September 1998, pp. 114-118.

Kenny, B.H., Kascak, P.E., Jansen, R., Dever, T., Santiago, W. 2005. Control of a high-speed flywheel system for energy storage in space applications. *IEEE Transactions on Industry Applications*, Vol. 41, No. 4, July/August 2005, pp. 1029-1038.

Kuosa, M., Sallinen, P., Larjola, J. 2004. Numerical and experimental modelling of gas flow and heat transfer in the air gap of an electric machine. *Journal of Thermal Science*, Vol. 13, No. 3, August 2004, pp. 264-278.

Kylander, G. 1995. Thermal modelling of small cage induction motors. *Chalmers University of Technology, School of Electrical and Computer Engineering*, No. 265, Göteborg, 113 p. (Doctoral thesis)

Liao, C., Chen, C.L., Katcher, T. 1999. Thermal management of AC induction motors using computational fluid dynamics modeling. *Proceedings of the International Conference Electric Machines and Drives - IEMD '99*, 9-12 May 1999, pp. 189-191.

Luomi, J., Zwyssig, C., Looser, A., Kolar, J.W. 2009. Efficiency optimisation of a 100-W 500 000-r/min permanent-magnet machine including air-friction losses. *IEEE Transactions on Industry Applications,* Vol. 45, No. 4, July/August 2009, pp. 1368-1377.

Matsushita, O., Kanemitsu, Y., Azuma, T., Fukushima, Y. 2000. Vibration criteria considered from case studies of active magnetic bearing equipped rotating machines. *International Journal of Rotating Machinery*, Vol. 6, No. 1, 2000, pp. 67-78.

Mekhiche, M., Kirtley, J.L., Tolikas, M., Ognibene, E., Kiley, J., Holmansky, E., Nimblett, F. 1999. High speed motor drive development for industrial applications. *Proceedings of International Conference of Electric Machines and Drives - IEMD'99*, 9-12 May 1999, pp. 244-248.

Mellor, P.H., Roberts, D., Turner, D.R. 1991. Lumped parameter thermal model for electrical machines of TEFC design. *IEE Proceedings-B*, Vol. 138, No. 5, September 1991, pp. 205-218.

Mellor, P.H., Burrow, S.G., Sawata, T., Holme, M. 2005. A wide-speed-range hybrid variable-reluctance/permanent-magnet generator for future embedded aircraft generation systems. *IEEE Transactions on Industry Applications*, Vol. 41, No. 2, March/April 2005, pp. 551-556.

Merrill, E.F. 1994. Dynamics of AC electrical machines. *IEEE Transactions on Industry Applications*, Vol. 30, No. 2, March/April 1994, pp. 277-285.

Micallef, C., Pickering, S. J., Simmons, K.A., Bradley, K.J. 2008. Improved cooling in the end region of a strip-wound totally enclosed fan-cooled induction electric machine. *IEEE Transactions on Industrial Electronics,* Vol. 55, No. 10, October 2008, pp. 3517-3524.

Minkowycz, W.J., Sparrow, E.M., Murthy, J.Y. 2006. Handbook of numerical heat transfer, 2nd edn., *Wiley*, New Jersey, 984 p.

Mohawk Innovative Technology®, Available at: http://www.miti.cc/, accessed October 2009.

Murphy, B.T., Kitzmiller, J.R., Zowarka, R., Hahne, J., Walls, A. 2001. Rotordynamics design and test results for a model scale compulsator rotor. *IEEE Transactions on Magnetics*, Vol. 37, No. 1, January 2001, pp. 310-313.

Offringa, L.J.J., Kerkenaar, R.W.P, van der Veen, J.L.F. 1996. A high-speed 1400 kW permanent-magnet generator with rectifier. *Proceedings of International Conference in Electrical Machines – ICEM'96*, Vol. 3, 10-12 September 1996, pp. 308-313.

Okamoto, S., Sakata, M., Kimura, K., Ohnabe, H. 1995. Vibration analysis of a high speed and light weight rotor system subjected to a pitching or turning motion, II: A flexible rotor system on flexible suspensions. *Journal of Sound and Vibration*, Vol. 184, No. 5, August 1995, pp. 887-906.

Oshima, M., Miyazawa, S., Diedo, T., Chiba, A., Nakamura, F., Fukao, T. 1996. Characteristics of a permanent magnet type bearingless motor. *IEEE Transactions on Industry Applications*, Vol. 32, No. 2, March/April 1996, pp. 363-370.

Paulides, J.J.H., Jewell, G.W., Howe, D. 2004. An evaluation of alternative stator lamination materials for a high-speed, 1.5 MW, permanent magnet generator. *IEEE Transactions on Magnetics*, Vol. 40, No. 4, July 2004, pp. 2041-2043.

Punnonen, P. 2007. Impingement jet cooling of end windings in a high-speed electric machine. *Acta Universitatis Lappeenrantaensis*, No. 286, Lappeenranta, 91 p. (Doctoral thesis)
Available at: https://oa.doria.fi/handle/10024/29732

Rahman, M.A., Chiba, A., Fukao, T. 2004. Super high speed electrical machines – summary. *Proceedings of IEEE-PES Meeting*, Vol. 2, 6-10 June 2004, pp. 1272-1275.

Saari, J. 1995. Thermal modelling of high-speed induction machines. *Acta Polytechnica Scandinavica, Electrical Engineering Series*, No. 82, Helsinki, 82 p. (Licentiate thesis)

Saari, J. 1998. Thermal analysis of high-speed induction machines. *Acta Polytechnica Scandinavica, Electrical Engineering Series*, No. 90, Espoo, 73 p. (Doctoral thesis)
Available at: http://lib.tkk.fi/Diss/199X/isbn9512255766/isbn9512255766.pdf

Saban, D.M., Bailey, C., Gonzalez-Lopez, D., Luca, L. 2008. Experimental evaluation of a high-speed permanent-magnet machine. *Proceedings of the 55th IEEE Petroleum and Chemical Industry Technical Conference - PCIC 2008*. 22-24 September, 2008, 9p.

Sakata, M., Kimura, K., Okamoto, S., Oikawa, K. 1995. Vibration analysis of a high speed and light weight rotor system subjected to a pitching or turning motion, I: A rigid rotor system on flexible suspensions, *Journal of Sound and Vibration*, Vol. 184, No. 5, August 1995, pp. 871-885.

Satcon®. Available at: http://www.satcon.com, accessed October 2009.

Schneider, T., Binder, A., Chen, L. 2005. Design procedure of bearingless high-speed permanent magnet motors. *Proceedings of the XII International Symposium on Electromagnetic Fields in Mechatronics, Electrical and Electronic Engineering - ISEF'05*, on CD, 15-17 September 2005, 6 p.

Schneider, T., Binder, A. 2007. Design and evaluation of a 60 000 rpm permanent magnet bearingless high speed motor. *Proceedings of the 7th International Conference on Power Electronics and Drive Systems – PEDS'07*, 27-30 November 2007, 8 p.

Schätzer, Ch., Binder, A. 2000. Design optimization of a high-speed permanent magnet machine with the VEKOPT algorithm. *Conference Record of the Industry Applications Conference – IAS 2000*, Vol. 1, 8-12 October 2000, pp. 439-444.

Shanel, M., Pickering, S.J., Lampard, D. 2000. Application of computational fluid dynamics to the cooling of salient pole electrical machines. *Proceedings of International Conference in Electrical Machines – ICEM 2000*, Vol. 1, 28-30 August 2000, pp. 338-342.

Shanel, M., Pickering, S.J., Lampard, D. 2003. Conjugate heat transfer analysis of a salient pole rotor in an air cooled synchronous generator. *Proceedings of the IEEE International Electric Machines and Drives Conference - IEMDC'03*, 1-4 June 2003, pp. 737-741.

Sinou, J.J., Villa, C., Thouverez, F. 2005. Experimental and numerical investigations of a flexible rotor on flexible bearing supports. *International Journal of Rotating Machinery*, Vol. 2005, No. 3, 2005, pp. 179-189.

Synchrony®. Available at: http://www.synchrony.com, accessed October 2009.

Takahashi, I., Koganezawa, T., Su, G., Ohyama, K. 1994. A super high speed PM motor drive system by a quasi-current source inverter. *IEEE Transactions on Industry Applications*, Vol. 30, No. 3, May/June 1994, pp. 683-690.

Trigeol, J., Bertin, Y., Lagonotte, P. 2006. Thermal modeling of an induction machine through the association of two numerical approaches. *IEEE Transactions on Energy Conversion,* Vol. 21, No. 2, June 2006, pp. 314-323.

Wang, J., Wang, F., Kong, X. 2008. Losses and thermal analysis of high speed PM machine. *Proceedings of the Joint International Conference on Power System Technology and IEEE Power India Conference – POWECON'08*, 12-15 October 2008, 5 p.

Zheng, L., Wu, T.X., Acharya, D., Sundaram, K.B., Vaidya, J., Zhao, L., Zhou, L., Murty, K., Ham, C.H., Arakere, N., Kapat, J., Chow, L. 2005. Design of a super-high speed permanent magnet synchronous motor for cryogenic applications. *Proceedings of the IEEE International Conference on Electric Machines and Drives – IEMD'05*, 15 May 2005, pp. 874-881.

Zhou, F., Shen, J., Fei, W., Lin, R. 2006. Study of retaining sleeve and conductive shield and their influence on rotor loss in high-speed PM BLDC motors. *IEEE Transactions on Magnetics*, Vol. 42, No. 10, October 2006, pp. 3398-3400.

Zienkiewicz, O.C., Taylor, R.L., Nithiarasu, P. 2005. The finite element method for fluid dynamics, 6th edn., *Butterworth-Heinemann*, Burlington, MA, 427 p.

Zwyssig, C., Kolar, J.W., Thaler, W., Vohrer, M. 2005. Design of a 100 W, 500000 rpm permanent-magnet generator for mesoscale gas turbines. *Conference Record of the Industry Applications Conference – IAS 2005*, Vol. 1, 2-6 October 2005, pp. 253-260.

Zwyssig, C., Round, S. D., Kolar, J. W. 2008. An ultrahigh-speed, low power electrical drive system. *IEEE Transactions on Industrial Electronics,* Vol. 55, No. 2, February 2008, pp. 577-585.

Zwyssig, C., Kolar, J.W., Round, S.D. 2009. Megaspeed drive systems: Pushing beyond 1 million r/min. *IEEE/ASME Transactions on Mechatronics*, Vol. 14, No. 5, October 2009, pp. 564-574.

Appendix A

Flow-chart of the methods used for the thermal analysis

The flow-chart of the methods that are used for the thermal analysis in this thesis is presented in Figure A1. The thick lines represent results obtained using numerical methods and the thin lines represent results obtained using traditional analytical and empirical methods. The results for electromagnetic and air-friction losses are denoted with pink and brown colour, respectively. They represent common input values for all methods. The empirical results for the coefficients of convection (thin green lines) are input values only for the thermal-network method. The 3D numerical heat-transfer method uses local values of the coefficients of convection denoted with thick green lines. These values together with the local values of the temperatures in the fluid (thick blue lines) are obtained from the 2D multiphysics method which couples CFD and heat-transfer equations. It means that the 3D numerical heat-transfer method is dependent on the 2D method since it uses the turbulent and thermal properties of the fluid flow from the 2D method. The final results of the temperatures in the machine that are obtained from the 3D numerical heat-transfer method are denoted with the thick red line. Besides the results for the fluid domain, the 2D multiphysics method also gives results for the temperatures in the solid domain of the machine and they are denoted with the dashed red line. However, these results are rough for the regions in the machine that do not have axial symmetries. The results for the temperatures in the fluid and solid domains of the machine that are obtained from the thermal-network method are denoted with thin blue and red lines, respectively.

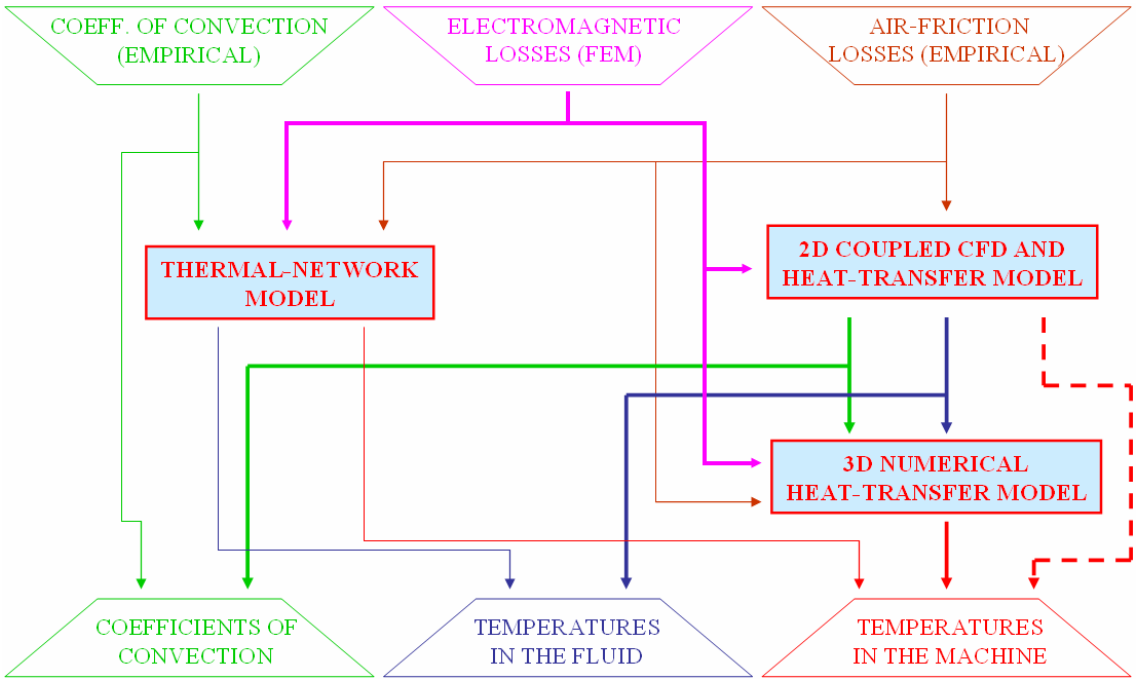

Figure A1: Flow-chart of the methods used for thermal analysis of the examined high-speed PM machines

Appendix B

Thermal resistances in the thermal network presented in Figure 3.3.

Rotor shaft:

$$R_{\mathrm{sh1}}=\frac{1}{2\pi l_{\mathrm{ra}}k_{\mathrm{sh}}};\ R_{\mathrm{sh2}}=\frac{l_{\mathrm{ra}}}{2\pi r_{\mathrm{sh}}^2k_{\mathrm{sh}}};\ R_{\mathrm{sh3}}=\frac{1}{2\pi l_{\mathrm{re}}k_{\mathrm{sh}}};\ R_{\mathrm{sh4}}=\frac{l_{\mathrm{re}}}{2\pi r_{\mathrm{sh}}^2k_{\mathrm{sh}}}.$$

Aluminium coating between the rotor shaft and the permanent magnets:

$$R_{\mathrm{coat1}}=\frac{1}{2\pi l_{\mathrm{ra}}k_{\mathrm{al}}}\ln\frac{2r_{\mathrm{coat}}}{r_{\mathrm{coat}}+r_{\mathrm{sh}}};\ R_{\mathrm{coat2}}=\frac{1}{2\pi l_{\mathrm{ra}}k_{\mathrm{al}}}\ln\frac{r_{\mathrm{coat}}+r_{\mathrm{sh}}}{2r_{\mathrm{sh}}};\ R_{\mathrm{coat3}}=\frac{l_{\mathrm{ra}}}{2\pi\left(r_{\mathrm{coat}}^2-r_{\mathrm{sh}}^2\right)k_{\mathrm{al}}}.$$

Aluminium ring:

$$R_{\mathrm{ring1}}=\frac{1}{2\pi l_{\mathrm{ring}}k_{\mathrm{al}}}\ln\frac{2r_{\mathrm{rm}}}{r_{\mathrm{rm}}+r_{\mathrm{sh}}};\ R_{\mathrm{ring2}}=\frac{1}{2\pi l_{\mathrm{ring}}k_{\mathrm{al}}}\ln\frac{r_{\mathrm{rm}}+r_{\mathrm{sh}}}{2r_{\mathrm{sh}}};\ R_{\mathrm{ring3}}=\frac{l_{\mathrm{ring}}}{2\pi\left(r_{\mathrm{rm}}^2-r_{\mathrm{sh}}^2\right)k_{\mathrm{al}}}.$$

Permanent magnets:

$$R_{\mathrm{rm1}}=\frac{1}{k_{\mathrm{m}}2\pi l_{\mathrm{ra}}k_{\mathrm{rm}}}\ln\frac{2r_{\mathrm{rm}}}{r_{\mathrm{rm}}+r_{\mathrm{coat}}};\ R_{\mathrm{rm2}}=\frac{1}{k_{\mathrm{m}}2\pi l_{\mathrm{ra}}k_{\mathrm{rm}}}\ln\frac{r_{\mathrm{rm}}+r_{\mathrm{coat}}}{2r_{\mathrm{coat}}};$$
$$R_{\mathrm{rm3}}=\frac{l_{\mathrm{ra}}}{k_{\mathrm{m}}2\pi\left(r_{\mathrm{rm}}^2-r_{\mathrm{coat}}^2\right)k_{\mathrm{rm}}}.$$

Aluminium bars:

$$R_{\mathrm{bar1}}=\frac{1}{\left(1-k_{\mathrm{m}}\right)2\pi l_{\mathrm{ra}}k_{\mathrm{al}}}\ln\frac{2r_{\mathrm{rm}}}{r_{\mathrm{rm}}+r_{\mathrm{coat}}};\ R_{\mathrm{bar2}}=\frac{1}{\left(1-k_{\mathrm{m}}\right)2\pi l_{\mathrm{ra}}k_{\mathrm{al}}}\ln\frac{r_{\mathrm{rm}}+r_{\mathrm{coat}}}{2r_{\mathrm{coat}}};$$
$$R_{\mathrm{bar3}}=\frac{l_{\mathrm{ra}}}{\left(1-k_{\mathrm{m}}\right)2\pi\left(r_{\mathrm{rm}}^2-r_{\mathrm{coat}}^2\right)k_{\mathrm{al}}}.$$

Carbon-fibre sleeve:

$$R_{\mathrm{rcfs1}} = \frac{1}{2\pi(l_{\mathrm{ra}} + l_{\mathrm{ring}})k_{\mathrm{rcfs}}} \ln\frac{2r_{\mathrm{rcfs}}}{r_{\mathrm{rcfs}} + r_{\mathrm{rm}}};\ R_{\mathrm{rcfs2}} = \frac{1}{2\pi(l_{\mathrm{ra}} + l_{\mathrm{ring}})k_{\mathrm{rcfs}}} \ln\frac{r_{\mathrm{rcfs}} + r_{\mathrm{rm}}}{2r_{\mathrm{rm}}};$$

$$R_{\mathrm{rcfs3}} = \frac{l_{\mathrm{ra}} + l_{\mathrm{ring}}}{2\pi\left(r_{\mathrm{rcfs}}^2 - r_{\mathrm{rm}}^2\right)k_{\mathrm{rcfs}}}.$$

Stator core:

$$R_{\mathrm{st1}} = \frac{h_{\mathrm{ss}}}{2\left[\pi\left(2r_{\mathrm{s1}} + h_{\mathrm{ss}}\right) - N_{\mathrm{s}}b_{\mathrm{ss2}}\right]l_{\mathrm{sa}}k_{\mathrm{scr}}};\ R_{\mathrm{st2}} = \frac{-R_{\mathrm{st1}}}{3};\ R_{\mathrm{sy1}} = \frac{1}{4\pi l_{\mathrm{sa}}k_{\mathrm{scr}}}\left[1 - \frac{2r_{\mathrm{s2}}^2 \ln\left(\frac{r_{\mathrm{s3}}}{r_{\mathrm{s2}}}\right)}{r_{\mathrm{s3}}^2 - r_{\mathrm{s2}}^2}\right];$$

$$R_{\mathrm{sy2}} = \frac{1}{4\pi l_{\mathrm{sa}}k_{\mathrm{scr}}}\left[\frac{2r_{\mathrm{s3}}^2 \ln\left(\frac{r_{\mathrm{s3}}}{r_{\mathrm{s2}}}\right)}{r_{\mathrm{s3}}^2 - r_{\mathrm{s2}}^2} - 1\right];\ R_{\mathrm{sy3}} = \frac{-1}{8\pi\left(r_{\mathrm{s3}}^2 - r_{\mathrm{s2}}^2\right)l_{\mathrm{sa}}k_{\mathrm{scr}}}\left[r_{\mathrm{s3}}^2 + r_{\mathrm{s2}}^2 - \frac{4r_{\mathrm{s3}}^2 r_{\mathrm{s2}}^2 \ln\left(\frac{r_{\mathrm{s3}}}{r_{\mathrm{s2}}}\right)}{r_{\mathrm{s3}}^2 - r_{\mathrm{s2}}^2}\right];$$

$$R_{\mathrm{sy4}} = \frac{l_{\mathrm{sa}}}{2\pi\left(r_{\mathrm{s3}}^2 - r_{\mathrm{s2}}^2\right)k_{\mathrm{sca}}};\ R_{\mathrm{sy5}} = \frac{-R_{\mathrm{sy4}}}{3}.$$

Stator winding:

$$R_{\mathrm{sw1}} = \frac{1}{l_{\mathrm{sa}}N_{\mathrm{s}}}\left(\frac{1}{4\pi k_{\mathrm{swr}}} + \frac{b_{\mathrm{ssi}}}{\left(2h_{\mathrm{ss}} + b_{\mathrm{ss2}}\right)k_{\mathrm{ssi}}} + \frac{1}{\left(2h_{\mathrm{ss}} + b_{\mathrm{ss2}}\right)h_{\mathrm{co10}}}\right);\ G_{\mathrm{w}} = \frac{1}{R_{\mathrm{sw1}}};$$

$$R_{\mathrm{w}} = \frac{l_{\mathrm{sa}}}{N_{\mathrm{s}}k_{\mathrm{f}}A_{\mathrm{ss}}k_{\mathrm{swa}}};\ R_{\mathrm{sw2}} = \sqrt{\frac{R_{\mathrm{w}}}{G_{\mathrm{w}}}}\tanh\sqrt{\frac{R_{\mathrm{w}}G_{\mathrm{w}}}{2}};\ R_{\mathrm{sw3}} = \frac{1}{G_w}\left(\frac{\sqrt{R_{\mathrm{w}}G_{\mathrm{w}}}}{\sinh\sqrt{\frac{R_{\mathrm{w}}G_{\mathrm{w}}}{2}}} - 1\right);$$

$$R_{\mathrm{sew1}} = \frac{3}{2}\frac{l_{\mathrm{sew}}}{N_{\mathrm{s}}k_{\mathrm{f}}A_{\mathrm{ss}}k_{\mathrm{swa}}};\ R_{\mathrm{sew2}} = \frac{3}{2}\frac{1}{4\pi^2\left(r_{\mathrm{sew1}} + r_{\mathrm{sew2}}\right)k_{\mathrm{swr}}}.$$

Stator ribs:

$$R_{\mathrm{rib1}} = \frac{h_{\mathrm{rib}}}{2n_{\mathrm{rib}}b_{\mathrm{rib}}l_{\mathrm{fr1}}k_{\mathrm{rib}}},\ R_{\mathrm{rib2}} = \frac{b_{\mathrm{rib}}}{4n_{\mathrm{rib}}h_{\mathrm{rib}}l_{\mathrm{fr1}}k_{\mathrm{rib}}}.$$

Frame:

$$R_{\mathrm{fr1}} = \frac{1}{2\pi l_{\mathrm{fr1}} k_{\mathrm{fr}}} \ln \frac{r_{\mathrm{fr2}} + r_{\mathrm{fr1}}}{2r_{\mathrm{fr1}}};\ R_{\mathrm{fr2}} = \frac{l_{\mathrm{fr1}}}{2\pi\left(r_{\mathrm{fr2}}^2 - r_{\mathrm{fr1}}^2\right) k_{\mathrm{fr}}};\ R_{\mathrm{fr3}} = \frac{l_{\mathrm{fr2}}}{2\pi\left(r_{\mathrm{fr2}}^2 - r_{\mathrm{fr1}}^2\right) k_{\mathrm{fr}}};$$

$$R_{\mathrm{fr4}} = \frac{1}{2\pi l_{\mathrm{fr2}} k_{\mathrm{fr}}} \ln \frac{r_{\mathrm{fr2}} + r_{\mathrm{fr1}}}{2r_{\mathrm{fr1}}}.$$

Symbols for the thermal conductivities [W/(m·K)]:

k_{sh} – solid steel shaft;
k_{al} – aluminium;
k_{rm} – permanent magnets;
k_{rcfs} – carbon-fibre sleeve;
k_{scr} – stator core, radial direction;
k_{sca} – stator core, axial direction;
k_{swr} – stator winding, radial direction;
k_{swa} – stator winding, axial direction;
k_{ssi} – stator slot insulation;
k_{rib} – stator rib between the stator yoke and frame;
k_{fr} – stator frame.

Other symbols:

k_{m} – ratio between the volume of the permanent magnets and the total volume of the region occupied by permanent magnets and aluminium cage [/];
k_{f} – filling factor of the stator slot [/];
N_{s} – number of stator slots [/];
h_{ss} – height of a stator slot [m];
b_{ss1} – width of a stator slot opening [m];
b_{ss2} – average width of a stator slot [m];
A_{ss} – surface area of a stator slot [m^2];
b_{ssi} – thickness of slot insulation [m];
h_{co10} – contact heat-transfer coefficient between stator winding and teeth [$\mathrm{W/(m^2 \cdot K)}$];
n_{rib} – number of stator ribs [/];
h_{rib} – height of a stator rib [m];
b_{rib} – width of a stator rib [m].

Convection:

$$R_1 = \frac{1}{h_1 2\pi r_{\mathrm{sh}} l_{\mathrm{re}}};\ R_2 = \frac{1}{h_2 \pi \left(r_{\mathrm{cfs}}^2 - r_{\mathrm{sh}}^2\right)};\ R_3 = \frac{1}{h_3 2\pi r_{\mathrm{rcfs}} (l_{\mathrm{ra}} + l_{\mathrm{ring}})};\ R_4 = \frac{1}{h_4 \left(2\pi r_{\mathrm{s1}} - N_{\mathrm{s}} b_{\mathrm{ss1}}\right) l_{\mathrm{sa}}};$$

$$R_5 = \frac{1}{h_5 \pi^2 r_{\mathrm{sew}} \left(r_{\mathrm{sew2}} + r_{\mathrm{sew1}}\right)};\ R_6 = \frac{1}{h_6 \pi^2 r_{\mathrm{sew}} \left(r_{\mathrm{sew2}} + r_{\mathrm{sew1}}\right)};\ R_7 = \frac{1}{h_7 \left[\pi \left(r_{\mathrm{s3}}^2 - r_{\mathrm{s1}}^2\right) - N_{\mathrm{s}} A_{\mathrm{ss}}\right]};$$

$$R_8 = \frac{1}{h_8 2\pi r_{\mathrm{fr1}} l_{\mathrm{fr2}}};\ R_9 = \frac{1}{h_9 l_{\mathrm{sa}} \left(2\pi r_{\mathrm{s3}} - n_{\mathrm{rib}} b_{\mathrm{rib}}\right)};\ R_{10} = \frac{1}{h_{10} l_{\mathrm{sa}} h_{\mathrm{rib}} n_{\mathrm{rib}} \cdot 2};$$

$$R_{11} = \frac{1}{h_{11} l_{\mathrm{sa}} \left(2\pi r_{\mathrm{fr1}} - n_{\mathrm{rib}} b_{\mathrm{rib}}\right)}.$$

Symbols for the coefficients of thermal convection [W/(m^2·K)]:

h_1 – rotor end-shaft and air;
h_2 – rotor ring and air;
h_3 – rotor surface and air in the air gap;
h_4 – stator surface and air in the air gap;
h_5 – inner end-winding surface and air;
h_6 – outer end-winding surface and air;
h_7 – stator yoke end-disc and air;
h_8 – frame and air in end-winding space;
h_9 – stator yoke and air in the axial cooling channel;
h_{10} – rib and air in the axial cooling channel;
h_{11} – frame and air in the axial cooling channel.

Contact resistances:

$$R_{\mathrm{co1}} = \frac{1}{2\pi r_{\mathrm{sh}} l_{\mathrm{ra}} h_{\mathrm{co1}}};\ R_{\mathrm{co2}} = \frac{1}{2\pi r_{\mathrm{sh}} l_{\mathrm{ring}} h_{\mathrm{co2}}};\ R_{\mathrm{co3}} = \frac{1}{k_{\mathrm{m}} 2\pi r_{\mathrm{coat}} l_{\mathrm{ra}} h_{\mathrm{co3}}};\ R_{\mathrm{co4}} = \frac{1}{k_{\mathrm{m}} \pi (r_{\mathrm{rm}}^2 - r_{\mathrm{coat}}^2) h_{\mathrm{co4}}};$$

$$R_{\mathrm{co5}} = \frac{1}{2 r_{\mathrm{rm}} \pi l_{\mathrm{ring}} h_{\mathrm{co5}}};\ R_{\mathrm{co6}} = \frac{1}{k_{\mathrm{m}} 2\pi r_{\mathrm{rm}} l_{\mathrm{ra}} h_{\mathrm{co6}}};$$

$$R_{\mathrm{co7}} = \frac{1}{(1 - k_{\mathrm{m}}) 2\pi r_{\mathrm{rm}} l_{\mathrm{ra}} h_{\mathrm{co7}}};\ R_{\mathrm{co8}} = \frac{1}{n_{\mathrm{rib}} b_{\mathrm{rib}} l_{\mathrm{sa}} h_{\mathrm{co8}}};\ R_{\mathrm{co9}} = \frac{1}{n_{\mathrm{rib}} b_{\mathrm{rib}} l_{\mathrm{fr1}} h_{\mathrm{co9}}}.$$

Symbols for the contact heat-transfer coefficients [W/(m^2·K)]:

h_{co1} – shaft and coating;
h_{co2} – shaft and ring;
h_{co3} – coating and permanent magnets;

h_{co4} – ring and permanent magnets;
h_{co5} – ring and carbon-fibre sleeve;
h_{co6} – permanent magnets and carbon-fibre sleeve;
h_{co7} – aluminium bars and carbon-fibre sleeve;
h_{co8} – stator yoke and ribs;
h_{co9} – ribs and frame.

The symbols for the dimensions that are met in the equations of the thermal resistances are shown in Figure B1.

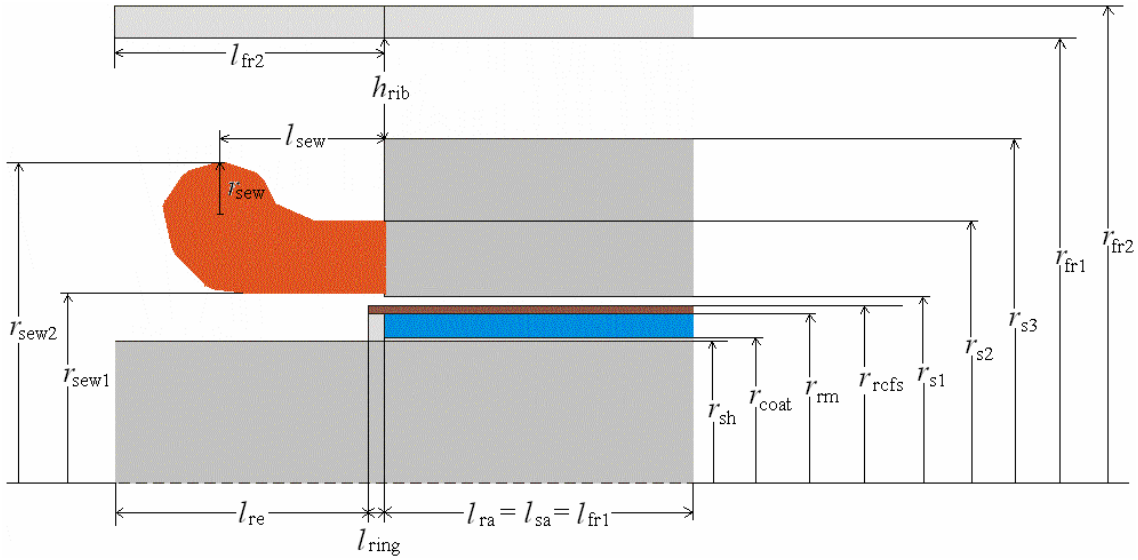

Figure B1: Axi-symmetric view of a half of the machine geometry and symbols for the dimensions that are met in the equations of the thermal resistances.

ISBN 978-952-60-3279-5
ISBN 978-952-60-3280-1 (PDF)
ISSN 1795-2239
ISSN 1795-4584 (PDF)